UNIVERSITY OF PADUA

Department of Industrial Engineering

Master Degree in Aerospace Engineering

HELICOPTER PERFORMANCE ANALYSIS BY MEANS OF A FREE-WAKE METHOD

Supervisor. Prof Benini, Ernesto
Airbus Supervisor. Hollands, Martin
Airbus Supervisor. Garavello, Andrea

Student: Alex Zanello

Academic Year 2018/2019

Abstract

The present work gives a short introduction to the theories that define a helicopter main rotor aerodynamics and performance. The coupling between a software that evaluates the forces on the rotor plane thanks to the blade element theory and a code that, by means of the vortex theory, simulates the inflow field in that region is explained. Three main test cases were simulated in many different conditions in order to explore the capabilities and the practical limits of the method. Starting from 2 blade test cases, parameters and common setting were investigated.

It has been found that the software presents some issues mainly regarding the integrity of the discretization and a correction has been proposed. This has been discovered by comparing the results obtained with the vortex method against experimental flight test data and CFD simulations.

However, the code increases the accuracy of the induced velocity field of the main rotor compared with a basic momentum theory by analyzing non uniform effects, finite blade effects and blade vortex interactions. This consequently produces an improvement of the performance prediction.

Contents

List of Figures

List of Tables

Notation

The symbols used in this work are alphabetically listed below:

a	blade section two-dimensional lift-curve slope
A	Rotor disk area
akh	Induced velocity correction factor for hover
akf	Induced velocity correction factor for forward flight
AoA	Angle of attack
B	Tip loss factor
$BEMT$	Blade Element Momentum Theory
BVI	Blade Vortex Interaction
c	Blade chord
CFD	Computational Fluid Dynamics
CPU	Central Processing Unit
c_d, c_l, c_m	Drag, Lift and Momentum coefficient
C_P	Power coefficient
C_{P_c}	Climb power loss
C_{P_i}	Induced power loss
C_{P_o}	Profile power loss
C_{P_p}	Parasite power loss
C_T	Thrust coefficient
D	Drag
DLR	Deutsches Zentrum für Luft- und Raumfahrt
FM	Figure of merit
F_x, F_y, F_z	Forces along x,y,z axis
I_b	Moment of inertia of the blade
k	Induced power correction factor
l	Length of a vortex segment
L	Lift
M_x, M_y, M_z	Momentums along x,y,z axis
$\dot{m}$	Mass flux through the rotor disk
N	Number of blades
N_A, N_ψ	FT-Freewake radial and azimuthal number of points
$NACA$	National Advisory Committee for Aeronautics
P	Rotor shaft power
Q	Rotor torque
p_i	Pressure in a defined position
r	Blade radial coordinate

r_0	Root radius
R	Rotor radius
RF	Relaxation factor
RoC	Rate of climb
T	Rotor thrust
V_x, V_y, V_z	Helicopter velocity with respect to the air
V_∞	Velocity of the helicopter in the fuselage reference system
V_C	Climb velocity
v_i	Induced velocity
v_h	Induced velocity in hover
VCR	Vortex Core Radius
α	Angle of attack
β	Blade flap angle
Γ	Bound vorticity
Γ_s	Shed vorticity
Γ_t	Trailing vortivity
κ	Distorsion factor of the induced velocity
η	Power available efficiency factor
ζ	Blade lag angle
θ	Blade pitch angle
θ_0	Collective pitch angle
θ_c	Lateral cyclic pitch angle
θ_s	Longitudinal cyclic pitch angle
θ_{75}	Pitch angle of the blade at 75% of the radius
λ	Rotor inflow ration
μ	Rotor advance ratio
ρ	Density of the air
σ	Solidity of the blades
ϕ	Section inflow angle
ω	induced velocity in the far wake
Ω	Rotational speed of the rotor

1 Introduction

This thesis work aims to analyze the performance of a helicopter in a large variety of flight conditions by means of a free-wake method in order to achieve medium-high accuracy results. The wake has a strong influence on the aerodynamics and the loads of the helicopter rotor, therefore an accurate prediction of its shape and its relative induced velocity field is desired.

Due to its relatively low computational time and the big variety of possible situations that occur in a rotating wing configuration, a large number of free-wake codes have been implemented in many different sectors regarding helicopters and wind turbine studies in the past years. The FT-Freewake code written by DLR aims to increase the accuracy of the inflow field used by AIRBUS Helicopters internal code Gensim in order to remove the empirical based models inside the codes that would not be reproducible for a different helicopter.

This paper presents results for three different rotors, which have been analyzed in steady state conditions, and aims to make the reader understand the strengths and the weaknesses of the theories implemented in both codes.

The free-wake code does not predict with 100% of accuracy all the phisical quantities describing the helicopter and its performance but aims to find a trade off between the high accuracy and computational time required by CFD and the low computational time and accuracy achieved with the classic momentum theory.

2 Theoretical background

In order to understand properly this work it is necessary to achieve a certain level of knowledge of all the different theories that have been used. In the first part of this chapter a brief theoretical background concerning the helicopters has been written.
The helicopter is a special type of aircraft which employes rotating wings to provide the necessary lift force that makes the whole body fly; the main parts that compose a helicopter are: the main rotor, the tail rotor the fuselage and the landing gear. The main component studied by this thesis is the main rotor and the wake that it generates. The rotor blades rotate around a vertical axis describing a horizontal disk above the fuselage. The lift is generated by the relative motion between every blade and the air. The rotating speed of the rotor is independent from the speed of the entire helicopter and, because of that, this machine does not require a translational motion to fly.
The helicopter therefore has the capability of vertical flight, forward flight, hover and even backward flight. The main rotor provides also the propulsive force that permits to move forward, which is generated by tilting the lift force in the forward direction.
Since the main rotor has such an important role in the helicopters dynamics it is clear that its efficiency must be as high as possible, which corresponds to maximizing the ratio between the thrust produced by the rotor and the required power. The key to achieve a low power loading is a low disk loading that means a low ratio between the rotor thrust and the total disk area. This aspect is clearly explained in [1]: conservation of momentum requires the lift to be obtained by accelerating air downwards, since corresponding to the lift is an equal and opposite reaction of the rotating wings against the air. This is the induced power loss, a property of both fixed and rotating wings that constitutes the absolute minimum of power required for equilibrium flight. For the rotary wing in hover, the induced power loading is found to be proportional to the square root of the rotor disk loading. Hence the efficiency of rotor thrust generation increases as the disk loading decreases.
The Helicopters are therefore characterized by a large rotor radius; the configuration most widely used is a main disk that rotates around a vertical axis above the fuselage and a smaller tail rotor that rotates at high rotational speed around an axis horizontal and perpendicular to the tail axis that has the task to produce a force that nullifies the torque induced by the main rotor on the fuselage.
However there are different configurations that use two couter-rotating main rotors placed in different positions. In this thesis, only the conventional helicopter configuration has been studied. However, since the wake principles are clearly the same, the method could be applied to general configurations.

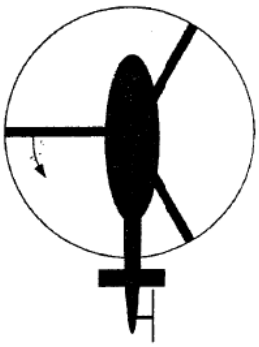

(a) Conventional configuration

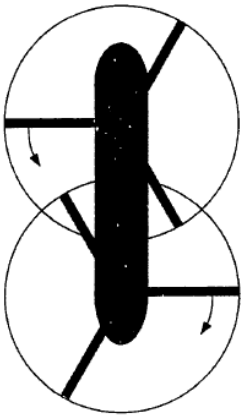

(b) Tandem configuration

(c) Coaxial configuration

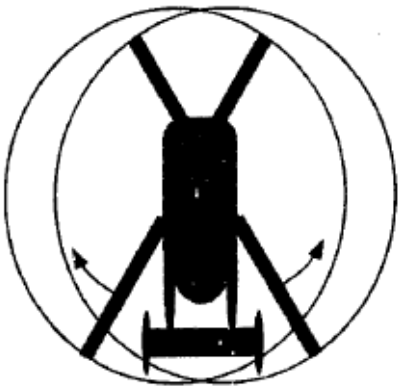

(d) Synchropter configuration

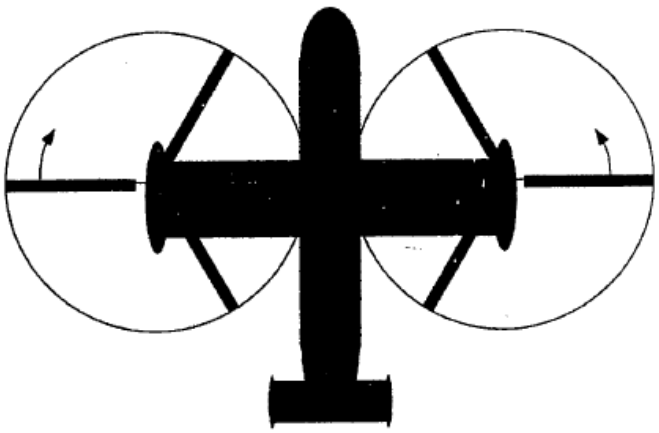

(e) Side by side configuration

Figure 1: Different helicopter configuration[1]

2.1 The main rotor

This chapter shows the features of the main rotor of a helicopter, summarizing the nomenclature and the parameters used throughout the document.
The rotor consists of an hub with two or more blades connected to it. The blades must be at the same angular distance and all the blades must have the same shape in order to have a balanced disk loading. The hub has an uniform rotation transmitted through a shaft torque that is connected with the engine by a gearbox. The value of the rotational speed Ω is chosen in order to produce enough lift to sustain the helicopter and allow the blades to work with an high efficiency, this value depends mainly on the radius of the rotor.
The shape of the blade has a great importance on the aerodynamics of the helicopter; there are many different currents of thought, however, the rotors studied within this thesis have a rettangular blade planform and, in the case of the H135, a parabolic blade tip.
In order to describe the position of a blade relative to the rotor plane, the following reference system is introduced. It is a polar system centered in the center of the hub with a distance indication r and an azimuth ψ. The maximum value of r is the radius of the rotor R and $\psi = 0$ corresponds to the downstream direction over the tail boom.

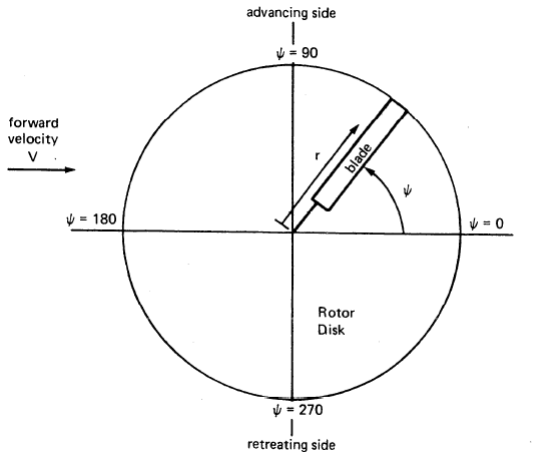

Figure 2: Reference system of the rotor[1]

As shown in Fig.2 the rotation direction will be counter clockwise for analysed rotors, this means that if the helicopter is in a forward flight motion the tangential velocity in the right half of the rotor has an opposite direction compared with the stream velocity. Because of that the right side of the rotor can be called advancing side and the left side is called retreating side.[1][2]

Other parameters that define a rotor and that will be widely used throughout this thesis are:

- $A = \pi R^2$ = total area of the disk
- c = blade chord f(r)
- N = number of blades
- $\sigma = Nc/\pi R$ = rotor solidity
- $I_b = \int_0^R mr^2$ = moment of inertia of the blade around the rotation axis

The rotor solidity is defined as the ratio between the blades area and the total area of the disk.
Now that the main parameters of the rotor have been defined it is important to introduce the motion of the single blade and its parameters: the blade is connected at the root by hinges that allow a 3 degrees of freedom motion.

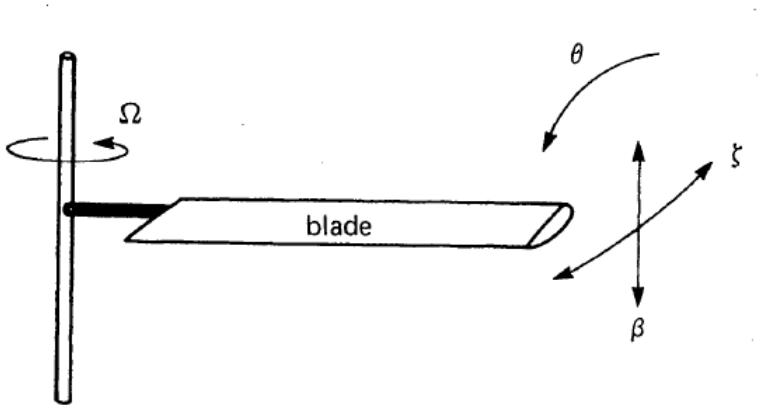

Figure 3: Blade motion[1]

θ is the blade pitch angle which is a rotation around the blade axis, it is considered positive for a nose-up rotation of the blade. ζ is called the lag angle and allows a motion of the blade inside the plane of the disk. It is considered positive if the lag is clockwise. β is the flapping angle that transforms the disk of the rotor in a cone, it is considered positive if the tip is higher than the hub.
Care must be taken not not to confuse θ with α which is the angle of attack of the blade in a defined section and depends on the pitch of the blade and its vertical and tangential velocity as it will be explained in chapter 2.3. This description of the blade motion applies to rigid blades where elastic deformations are not accounted for.
Now that the basic geometry of the main rotor is clear, it is important to introduce how these angles change during an entire revolution since the blade displacement is

periodic around the azimuth angle in a steady state motion. To properly understand the blade motion behaviour, the periodic displacements can be decomposed by means of a Fourier analysis around ψ.:

$$\theta = \theta_0 + \theta_{1c}cos(\psi) + \theta_{1s}sin(\psi) + \theta_{2c}cos(2\psi) + \theta_{2s}sin(2\psi) \tag{2.1.1}$$

$$\beta = \beta_0 + \beta_{1c}cos(\psi) + \beta_{1s}sin(\psi) + \beta_{2c}cos(2\psi) + \beta_{2s}sin(2\psi) \tag{2.1.2}$$

$$\zeta = \zeta_0 + \zeta_{1c}cos(\psi) + \zeta_{1s}sin(\psi) + \zeta_{2c}cos(2\psi) + \zeta_{2s}sin(2\psi) \tag{2.1.3}$$

In the first equation that shows the motion of the pitch angle of the blade against the azimuth, three very important parameters for the entire helicopters control appear. θ_0 is the collective angle, which does not depend on the azimuth and it is a constant on the entire revolution. This angle is the main factor that controls the vertical lift of the helicopter. To provide the tilt of the lift force in lateral and longitudinal direction the cyclic angles must be involved. These two angles, called θ_{1c} and θ_{1s}, are a sinusoidal and a cosinusoidal function of the azimuth angle and their task is to permit forward flight and a large number of different maneuvers.
For a fixed untwisted wing the lift is constant along the radial dimension due to the fact that the relative velocity between the wing and the air is the same in every section of the blade. This is obviously not true for a helicopter, even if considering the blade untwisted the tangential speed at the leading edge will depend on the radius and the angular velocity as: $V_{tan} = \Omega r$. If the helicopter is in forward flight condition the stream velocity must be considered and the tangential velocity at any point of the disk becomes:

$$V_{tan} = \Omega r + V_\infty sin(\psi) \tag{2.1.4}$$

For a helicopter in hover condition the tangential velocity increases linearly with the radius of the rotor and reaches its maximum at the blade tip where $r = R$, for forward flight condition the maximum value is reached at the tip of the blade positioned at an azimuth of 90 degrees; the distribution is still linear but the null is not centered in the rotation axis of the blades. The Fig.4 explains this concept by showing the trend of the incident velocity for a rotor in hover and a rotor in forward flight.
In the image that explains the forward flight trend there is an area of reverse flow, this region occurs where the stream velocity multiplied by $sin(\psi)$ is higher than the tangential speed of the blade, this means that air encounters the blade at the trailing edge and does not produce any lift. It is interesting to note that the wing of a helicopter stalls at high flight speeds instead of low speeds of the fixed wing. A problem that occurs in forward flight on the advancing wing is the relatively high Mach number

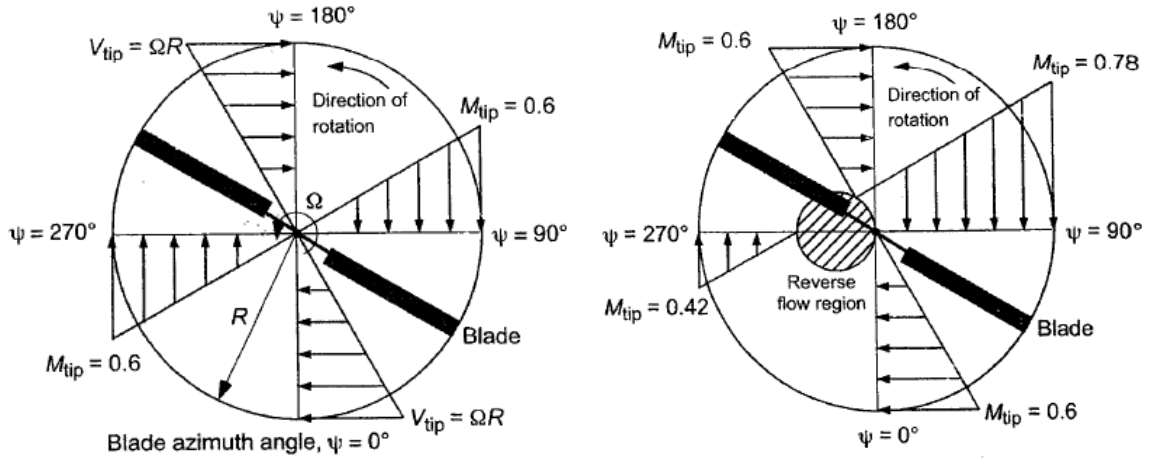

(a) Hovering flight

(b) Forward flight

Figure 4: Distribution of incident velocity on the leading edge of the rotor blade[1]

at the blade tip that in the worst case can cause a shock wave that might produce a separation of the flow or at least an increase of the drag force.

2.2 Momentum theory

The first theory analyzed in this thesis is the momentum theory which (coupled with the blade element theory) is used in Gensim.
The first situation that will be analyzed is the hover case, which is the simplest to evaluate since there is no interaction between the wake and the stream velocity. This theorical approach named Rankine-Freud momentum theory allows the reader just to have a first prediction of the thrust or the power of the rotor. To have a more accurate prediction, a method that analyzes the wake or that solves the Navier-Stokes equation is required.
As usually happens for the study of a phenomenon in aerodynamics the three laws of conservation will be used. For this approach the following boundary conditions will be assumed:

- Flow through the rotor is one dimensional and uniform
- The fluid is ideal
- The flow is steady-state

This means that the flow properties in a defined point do not depend on the time, that the viscous losses are neglected and the only losses that occurs are the induced losses,

and that the properties across any plane parallel to the rotor plane are equal.[2]
In order to analyze the rotor performance a control volume of area S sorrounding the rotor and its wake is assumed.

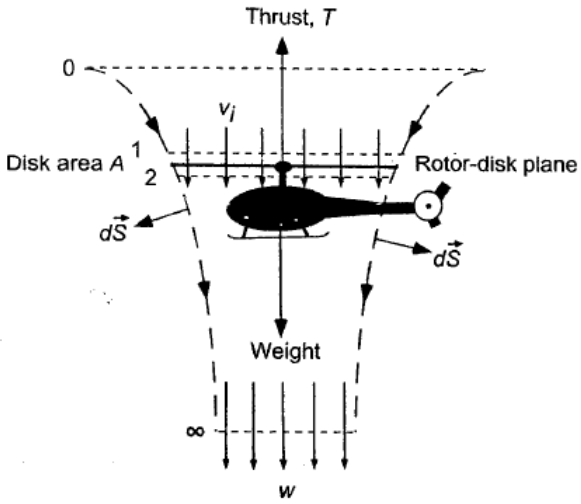

Figure 5: Control volume for hover[2]

The mass conservation law can be written as:

$$\iint_S \rho \vec{V} \cdot d\vec{S} = 0 \tag{2.2.1}$$

where $d\vec{S}$ is the unit normal area vector which points outside the control volume, ρ the density of the fluid and V the local speed. This equation means that the mass entering the control volume is equal to the mass exiting it.
The second statement used is the momentum conservation law:

$$\vec{F} = \iint_S p d\vec{S} + \iint_S (\rho \vec{V} d\vec{S}) \cdot \vec{V} \tag{2.2.2}$$

The assumption is a uniform pressure P jump over the rotor disk and that the distribution of the velocity does not change across any horizontal section of the control volume.
The force acting on the fluid is supplied by the rotor, and thanks to the third Newton law, the fluid applies an equal force but in the opposite direction on the rotor which is the thrust T.
The third law is the energy conservation law which is a scalar equation that states that the work made by the rotor on the fluid is manifested as an increase of the kinetic

energy:

$$W = \iint_S \frac{1}{2}(\rho\vec{V} \cdot d\vec{S})|\vec{V}|^2 \tag{2.2.3}$$

Equations (2.2.1), (2.2.2), (2.2.3) have been already simplified by the boundary conditions called out before.[1][2][4]

2.2.1 Momentum theory for hover

According to the theory described by Leishman [2] that follows the procedures attributed to Rankine and Froude and generalized by Glauert, the three equation written in the previous section will now be applied for a hover rotor.
The section 0 in Fig. 5 denotes a plane far upstream the rotor, the section 1 is placed just above and section 2 is placed just below the rotor disk plane, which has an area called A. The last section considered is the section ∞ which denotes a section very far below the disk.
Lets consider an induced velocity v_i which is the velocity of the mass of air at the rotor disk. This velocity will increase during the descend and at the far wake is denoted by ω. Using the mass conservation law it is possible to say that the mass flow rate $\dot{m}$ is equal to:

$$\dot{m} = \iint_\infty \rho\vec{V} \cdot d\vec{S} = \iint_2 \rho\vec{V} \cdot d\vec{S} \tag{2.2.4}$$

and thanks to the 1-D flow assumption and integrating the mass flow is:

$$\dot{m} = \rho A_\infty \omega = \rho A_2 v_i = \rho A v_i \tag{2.2.5}$$

It is possible to find the thrust produced by the rotor thanks to the momentum law :

$$T = \iint_\infty (\rho\vec{V}d\vec{S}) \cdot \vec{V} - \iint_0 (\rho\vec{V}d\vec{S}) \cdot \vec{V} \tag{2.2.6}$$

in hover condition the velocity far above the rotor is equal to zero so the second integral in the previous equation is zero and the formula can be reduced to:

$$T = \iint_\infty (\rho\vec{V}d\vec{S}) \cdot \vec{V} = \dot{m}\omega \tag{2.2.7}$$

The energy conservation principle helps finding the power consumed by the rotor which is equal to:

$$P = Tv_i = \iint_\infty \frac{1}{2}(\rho\vec{V} \cdot d\vec{S})\vec{V}^2 - \iint_0 \frac{1}{2}(\rho\vec{V} \cdot d\vec{S})\vec{V}^2 \tag{2.2.8}$$

as in equation (2.2.7) the second integral is equal to zero and the formula becomes:

$$P = Tv_i = \iint_{\infty} \frac{1}{2}(\rho\vec{V} \cdot d\vec{S})\vec{V}^2 = \frac{1}{2}\dot{m}\omega^2 \tag{2.2.9}$$

Coupling eq. (2.2.8) with (2.2.7) it is possible to find the relationship between v_i and ω as:

$$v_i = \frac{1}{2}\omega \tag{2.2.10}$$

This means that using the law of mass conservation, the section at the rotor disk is two times bigger than the section at which the wake is fully developed.
It is very important to understand the relationship between the induced velocity and the thrust or the power of the rotor; this can be done just by mathematically combine the previous formulas and solving them for the needed variable:

$$T = \dot{m}\omega = 2\dot{m}v_i = 2\rho A v_i^2 \tag{2.2.11}$$

Recalculating this equation to find the v_i as a function of the thrust it is clear that the induced velocity at the rotor disk is:

$$v_i = \sqrt{\frac{T}{A}\frac{1}{2\rho}} \tag{2.2.12}$$

This helps to define a new ratio which is the disk loading T/A.
To complete the analysis the ideal power to hover can be defined as:

$$P = Tv_i = \frac{T^{\frac{3}{2}}}{\sqrt{2\rho A}} = 2\rho A v_i^3 \tag{2.2.13}$$

In order to decrease the required power the last term of the previous equation suggests to increase the rotor disk area as much as possible in order to reduce the v_i which affects by cubic function the power.
Corresponding to an increment of the speed there is also a variation of the pressure in the horizontal sections of the wake. This phenomenon can be analyzed by means of the Bernoulli principle: there is a real jump of pressure between the area just above and the section just below the rotor made by the additional work added by the blades. The Bernoulli equation, which represents the energy conservation law for an incompressible flow is used between the point 1 and 2 of the control volume in order to find the variation of pressure:

$$p_0 = p_\infty = p_1 + \frac{1}{2}\rho v_i^2 \tag{2.2.14}$$

$$p_2 + \frac{1}{2}\rho v_i^2 = p_\infty + \frac{1}{2}\rho\omega^2 \tag{2.2.15}$$

Assuming that the pressure jump is uniform along the disk, it must result that:

$$\Delta p = p_2 - p_1 = \frac{T}{A} \tag{2.2.16}$$

coupling together (2.2.14), (2.2.15) and (2.2.16) it is possible to find:

$$\frac{T}{A} = p_2 - p_1 = \frac{1}{2}\rho\omega^2 \tag{2.2.17}$$

According to these equations, the relationship between the static pressure p_∞ and the pressure just above and just below the rotor disk are:

$$p_1 = p_\infty - \frac{1}{2}\rho v_i^2 = p_\infty - \frac{1}{2}\rho\frac{\omega^2}{4} = p_\infty - \frac{1}{4}\frac{T}{A} \tag{2.2.18}$$

$$p_2 = p_0 + \frac{1}{2}\rho\omega^2 - \frac{1}{2}\rho\frac{\omega^2}{4} = p_0 + \frac{3}{4}\frac{T}{A} \tag{2.2.19}$$

2.2.2 Momentum theory for vertical climb flight

In this chapter, an important flight situation will be analyzed. Vertical climb occurs when, for example, the helicopter needs to take off. In this situation, the rotor must provide the thrust to lift up the helicopter over a wide range of gross weights. This case will be analyzed with the three conservation laws (2.2.1), (2.2.2) and (2.2.3) as well. In the following, the symbol v_h indicated the induced velocity in hover in order to reduce the length formulations and compare the v_i for the two cases. The same boundary conditions will be used.

The main difference with the hover case is the presence of a stream velocity along the vertical axis called rate of climb, V_C or (RoC according to the most common aeronautical gergon). The total velocity at the rotor plane is the sum between the rate of climb and the induced velocity. The velocity where the wake is fully developed will be $V_c + \omega$.

As for the hover case, a control volume must be defined: Thanks to the mass conservation law it is possible to write:

$$\dot{m} = \iint_\infty \rho\vec{V}\cdot d\vec{S} = \iint_2 \rho\vec{V}\cdot d\vec{S} \tag{2.2.20}$$

integrating Eq. (2.2.20) the result is:

$$\dot{m} = \rho A_\infty(V_c + \omega) = \rho A(V_c + v_i) \tag{2.2.21}$$

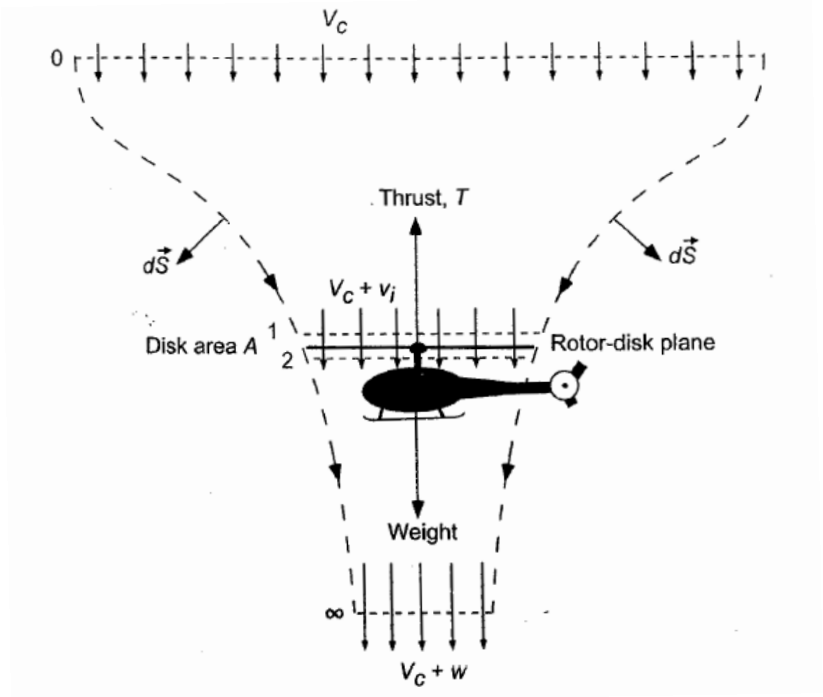

Figure 6: Control volume for climb ascent[1]

This means that the mass flow is increased by V_c compared with the hover case. The thrust has been found with the conservation momentum law as:

$$T = \iint_{\infty} \rho(\vec{V} \cdot d\vec{S})\vec{V} - \iint_{0} \rho(\vec{V} \cdot d\vec{S})\vec{V} \tag{2.2.22}$$

In this case, the second integral can not be considered zero because of the presence of the rate of climb so the thrust will be:

$$T = \dot{m}(V_c + \omega) - \dot{m}V_c = \dot{m}\omega \tag{2.2.23}$$

and the work made by the rotor is:

$$T(V_c + v_i) = \iint_{\infty} \frac{1}{2}\rho(\vec{V} \cdot d\vec{S})\vec{V}^2 - \iint_{0} \frac{1}{2}\rho(\vec{V} \cdot d\vec{S})\vec{V}^2 \tag{2.2.24}$$

that after double integration becomes:

$$T(V_c + v_i) = \frac{1}{2}\dot{m}(V_c + \omega)^2 - \frac{1}{2}\dot{m}V_c^2 = \frac{1}{2}\dot{m}\omega(2V_c + \omega) \tag{2.2.25}$$

Coupling (2.2.24) and (2.2.25) it results that $\omega = 2v_i$ which is exactly the same result that occurs for the hover case. The relationship between the thrust and the induced

velocity becomes:

$$T = \dot{m}\omega = \rho A(V_c + v_i)\omega = 2\rho A(V_c + v_i)v_i \tag{2.2.26}$$

dividing both terms for $2\rho A$ and v_h^2 the equation becomes a quadratic equation on v_i/v_h as:

$$\left(\frac{v_i}{v_h}\right)^2 + \frac{V_c}{v_h}\left(\frac{v_i}{v_h}\right) - 1 = 0 \tag{2.2.27}$$

which has the two solutions:

$$\frac{v_i}{v_h} = -\left(\frac{V_c}{2v_h}\right) \pm \sqrt{\left(\frac{V_c}{2v_h}\right)^2 + 1} \tag{2.2.28}$$

but the ratio between v_i and v_h must be positive otherwise the flow model would be violated so the only possible solution is the positive one:

$$\frac{v_i}{v_h} = -\left(\frac{V_c}{2v_h}\right) + \sqrt{\left(\frac{V_c}{2v_h}\right)^2 + 1} \tag{2.2.29}$$

This solution shows that as the rate of climb of the helicopter increases its induced velocity decreases. However this equation has a lower limit for V_c that is exactly the hover condition because below that case there could be two different flow direction, which of course can not be possible. So this theory must be considered correct just for positive values of V_c and not for descent.[2]

2.2.3 Momentum theory for axial descent flight

This is the case where the slipstream is above the rotor disk. In this flight condition $-2v_h > V_c$. If the rate of climb is between $-2v_h$ and 0 the velocity at any plane through the rotor slipstream can be either upward or downward and a more complex flow pattern is required. Fig.7 shows the new control volume. A boundary condition must be added to the previous ones which stay unchanged: $|V_c| > 2v_h$. The direction for positive velocity is still downward.
The procedure that will be applied is the same used in hover and climb flight, so, the first parameter to be calculated is the mass flow rate:

$$\dot{m} = \iint_{\infty} \rho\vec{V} \cdot d\vec{S} - \iint_{2} \rho\vec{V} \cdot d\vec{S} \tag{2.2.30}$$

after integration (2.2.30) becomes:

$$\dot{m} = \rho A_{\infty}(V_c + \omega) = \rho A(V_c + v_i) \tag{2.2.31}$$

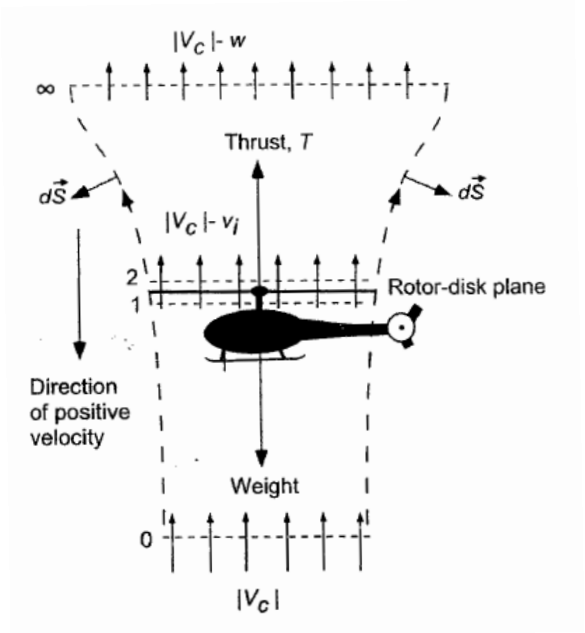

Figure 7: Control volume for descent[1]

Now the thrust force is:

$$T = -\left(\iint_{\infty} \rho(\vec{V} \cdot d\vec{S})\vec{V} - \iint_{0} \rho(\vec{V} \cdot d\vec{S})\vec{V} \right) \tag{2.2.32}$$

The first minus in (2.2.32) is caused by the direction of the flow relative to the axis reference. In this case the thrust becomes:

$$T = -\dot{m}(V_c + \omega) + \dot{m}V_c = -\dot{m}\omega \tag{2.2.33}$$

Eq. (2.2.33) shows a negative thrust but clearly that is not true because of the negative sign of the flow mass rate. The last parameter that has to be found is the power required:

$$T(v_i + V_c) = \iint_{0} \frac{1}{2}\rho(\vec{V} \cdot d\vec{S})\vec{V}^2 - \iint_{\infty} \frac{1}{2}\rho(\vec{V} \cdot d\vec{S})\vec{V}^2 \tag{2.2.34}$$

and after integration the result is:

$$T(v_i + V_c) = \frac{1}{2}\dot{m}V_c^2 - \frac{1}{2}\dot{m}(V_c + \omega)^2 = -\frac{1}{2}\dot{m}\omega(2V_c + \omega) \tag{2.2.35}$$

The rotor power is negative which means that the rotor is extracting power from the airstream. The rotor in this situation, called windmill state, is decreasing the speed of the air.

It is now important to find a correlation between the V_C and the induced velocity as

it has been made for the ascending case. Using the thrust formulation as:

$$T = -\dot{m}\omega = -\rho A(V_c + v_i)\omega = -2\rho A(V_c + v_i)v_i \tag{2.2.36}$$

and dividing by $2\rho A$ and v_h^2:

$$\left(\frac{v_i}{v_h}\right)^2 + \frac{V_c}{v_h}\left(\frac{v_i}{v_h}\right) + 1 = 0 \tag{2.2.37}$$

The equation is very similar to the climbing case, the only solution valid is that one that does not violate the flow model which is:

$$\frac{v_i}{v_h} = -\left(\frac{V_c}{2v_h}\right) - \sqrt{\left(\frac{V_c}{2v_h}\right)^2 - 1} \tag{2.2.38}$$

Remembering that this equation is valid only for $V_c/v_h \leq 2$.
To conclude this chapter it is necessary to analyze what happens in the region between the pure ascent case and the high rate of descent case. This region is defined by $-2 \leq V_c/v_h \leq 0$. The momentum theory is useless in this zone because it is impossible to set a control volume since the flow can take different directions.
The only possibility to solve the problem and find a curve that connects the equation for the ascent case and the fast descent case is to fit an interpolation between empirical values. A lot of different studies have been made, but in this thesis only a quartic function valid for the full range will be proposed:

$$\frac{v_i}{v_h} = \kappa + \kappa_1\left(\frac{V_c}{v_i}\right) + \kappa_2\left(\frac{V_c}{v_i}\right)^2 + \kappa_3\left(\frac{V_c}{v_i}\right)^3 + \kappa_4\left(\frac{V_c}{v_i}\right)^4 \tag{2.2.39}$$

where κ is the measured induced power factor in hover, $\kappa_1 = -1.125$, $\kappa_2 = -1.372$, $\kappa_3 = -1.718$ and $\kappa_4 = -0.655$. The following graph summarizes the trend of the induced velocity ratio versus the climb velocity ratio for both ascent and descent cases.

2.2.4 Momentum theory for forward flight

The last flight case that will be analyzed with the momentum theory is the forward flight; in this situation the rotor tilts by an angle to produce the propulsive force that pushes forward the helicopter. The flow model is non axisymmetric and there will be some assumptions in order to represent better the flow field.
V_∞ is the stream velocity of the helicopter; the purpose of this paragraph is to find a

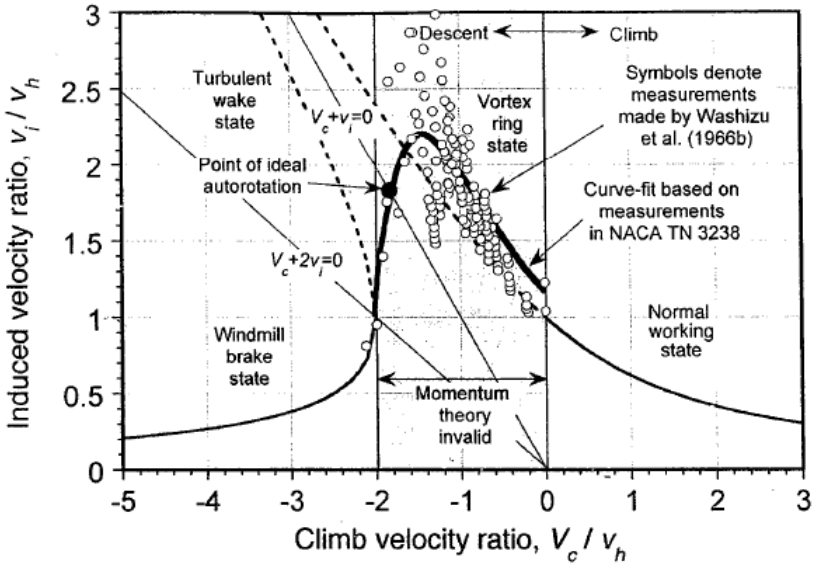

Figure 8: Induced velocity ratio vs climbing ratio[1]

law, which, if used for hover will achieve the same results seen before.
It is necessary to introduce a new velocity U which is the resultant velocity at the rotor disk:

$$U = \sqrt{(V_\infty cos\alpha)^2 + (V_\infty sin\alpha + v_i)^2} \tag{2.2.40}$$

where α is the angle between the rotor disk and V_∞. This theorical model has been studied by Glauert and it is well summarized in the following image:

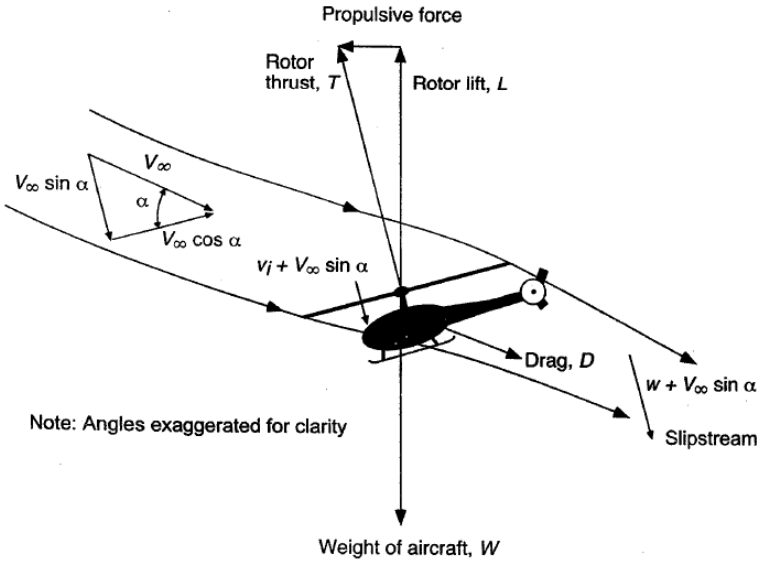

Figure 9: Glauert flow model for forward flight[3]

According to the momentum theory the mass flow rate will now be:

$$\dot{m} = \rho A U \tag{2.2.41}$$

Thanks to the momentum conservation law and the conservation of energy it is easy to find the thrust and the power as:

$$T = \dot{m}(\omega + V_\infty sin\alpha) - \dot{m}V_\infty sin\alpha = \dot{m}\omega \tag{2.2.42}$$

$$P = T(v_i + V_\infty sin\alpha) = \frac{1}{2}\dot{m}(2V_\infty \omega sin\alpha + \omega^2) \tag{2.2.43}$$

Coupling together (2.2.42) and (2.2.43) it is possible to find the relationship between ω and v_i which as usual is: $\omega = 2v_i$ To compare the induced velocity in a forward flight case with the hover case three parameters will be introduced:

- The advance ratio $\mu = V_\infty cos\alpha/(\Omega R)$
- The inflow ratio $\lambda = (V_\infty sin\alpha + v_i)/(\Omega R)$
- Thrust coefficient $C_T = \frac{T}{\frac{1}{2}\rho A(\Omega R)^2}$

From the hover case it is clear that $\lambda_h = \sqrt{C_T/2}$. After a few algebraic substitutions the inflow ratio that rules the relationship between the two induced velocities is defined as:

$$\lambda = \mu tan\alpha + \frac{C_T}{2\sqrt{\mu^2 + \lambda^2}} \tag{2.2.44}$$

The following graph shows the induced inflow ratio λ_i/λ_h against the forward speed ratio for different values of α.

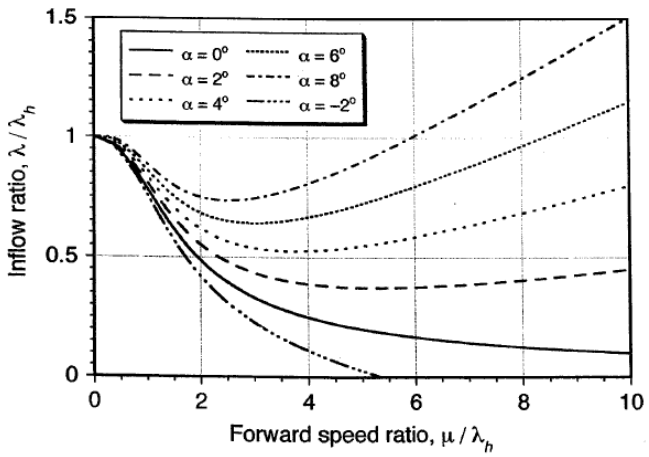

Figure 10: induced inflow ratio vs forward speed ratio[1]

Now that every flight situation has been analyzed, and before introducing another theory that describes with an higher accuracy the flow field, it is important to understand which are the limits of the momentum theory and where it requires some corrections that could be both theorical or empirical.[1]

2.2.5 Non-ideal effects on rotor performance

In this chapter some non ideal effects on the rotor thrust will be discuss with accuracy since the main purpose of this thesis is to avoid the empirical corrections that must be applied to the momentum theory and, in the next chapter, to the blade element theory to obtain proper results.
The first non ideal effect that will be analyzed is the losses on local thrust distribution due to a tip loss effect. For an infinite long ideal blade it is already clear that the thrust increases with the radius, but, when the blade comes to an end a strong tip vortex is produced. The air goes from the pressure side to the suction side of the blade reducing the lift. This phenomenon reduces the total lifting area of the rotor.

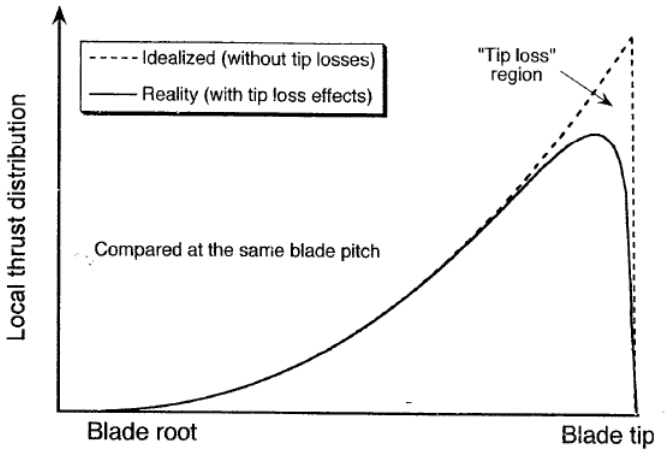

Figure 11: Tip losses[2]

For preliminary analysis a coefficient smaller than one is multiplied for the rotor disk area. In the AIRBUS Helicopters internal code Gensim to consider tip effects are taken into account by iterrupting the lift forces integration at a certain distance from the tip (tipically 97% of radius). Obviously the drag is not affected by this effect.
A correlated phenomenon is the cut off effect at the root of the blade: the wing does not start at $r = 0$ and this reduced the working area of the rotor.
If the value of the radius where the wing profile starts is r_0 and the tip loss coefficient is B, then the ratio between the area of the rotor and the area that produces thrust is:

$$\frac{A_e}{A} = B^2 - r_0^2 \tag{2.2.45}$$

There are a lot of empirical theories to find the best value of B which depends on the number of the blades and their the geometry and the thrust coefficient. Fig.12 shows the trend of B as a function of the thrust coefficient for different numbers of blades with the same geometry.

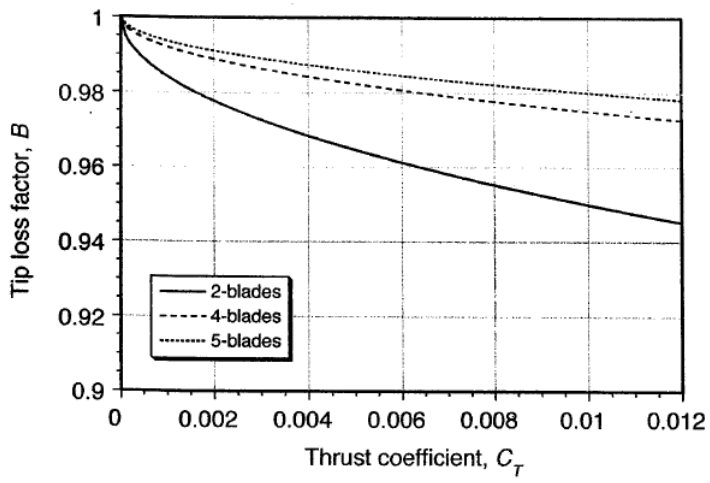

Figure 12: tip loss factor[3]

To compare the required power that comes from the ideal momentum theory and the real result measured in a flight test a new coefficient will be introduced. The power coefficient C_P defined as:

$$C_P = \frac{P}{\rho A(\Omega R)^3} = \frac{C_T^{\frac{3}{2}}}{\sqrt{2}} \tag{2.2.46}$$

The last term of the formulation is the relationship between the power coefficient and the thrust coefficient, both are ideal coefficients that come from the momentum theory. From flight tests it is clear that the last formulation underestimates the induced power coefficient, so it is necessary to multiply the result for a scalar number κ which is the induced power correction factor:

$$C_P = \frac{\kappa C_T^{\frac{3}{2}}}{\sqrt{2}} \tag{2.2.47}$$

This coefficient considers all the non ideal but physical phenomena that affects the theory such as: tip losses, wake swirl, non-ideal wake contraction, finite number of blades and non uniform inflow which is the main problem that the free wake method aims to solve. The swirl effect reduces the net change of the fluid momentum and affects the power coefficient for a 1% variation.[4]
To find the profile power, which is the power that a blade requires to move in a viscous fluid, the drag coefficient is required.

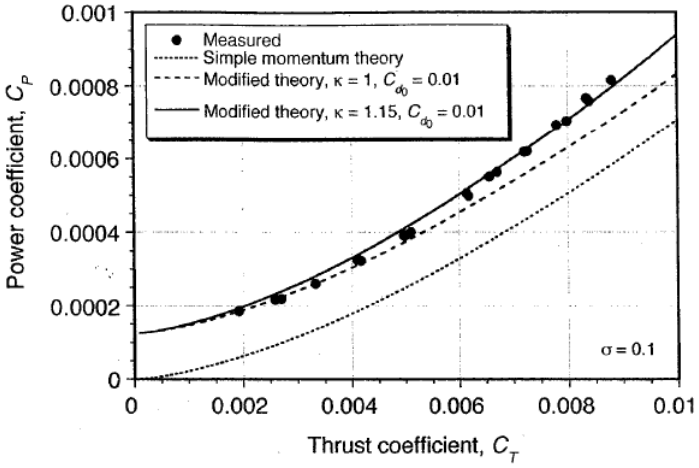

Figure 13: Non ideal effects on momentum theory[3]

2.3 The blade element theory

In this section the blade element theory, which is widely used in helicopter performance calculation and permits the design of the main rotor, will be summarized. This method calculates the forces on the blade and the rotor disk by analyzing the motion of the wing through the air. It applies the lifting line theory of Prandtl to a rotating wing; the wing is divided in sections along the radius and it is assumed that each section acts like a 2-D airfoil to produce the forces. The effects of the angle of the wake and the rest of the rotor must be considered in a variation of the angle of attack at the analyzing section.

Obviously an estimation of the induced velocity at the rotor disk is required. This can be done with several methods like momentum theory or vortex theory but in the case of Gensim (if not coupled with other codes) there is an improved momentum theory based inflow model calculating the induced velocity at any position of the disk is employed. This model will be replaced with the inflow calculated by means of the free-wake and the differences between the two flow fields will be discuss in the next chapters.

To be efficient, the lifting line theory assumes that the blade has a high aspect ratio which is usually true for low disk loading. Before introducing the model it is important to itemize the assumptions and the boundary conditions characterizing this theory and permitting an analytical solution:

- Low disk loading
- Neglect stall
- Neglect compressibility effects

The stall effect ad the compressibility effects can be taken into account by including a non-linear behaviour of the lift and drag coefficient along the angle of attack.
It is now important to determine the angles and the velocities in every section of the wing: θ is the pitch angle measured from the plane of rotation and the zero lift line, in components the blade sees a normal and a tangential velocity called respectively u_P and u_T. These two components define the inflow angle as:

$$\phi = tan^{-1}\frac{u_P}{u_T} \tag{2.3.1}$$

and of course the magnitude of the resultant velocity is:

$$U = \sqrt{u_T^2 + u_P^2} \tag{2.3.2}$$

The aerodynamic angle of attack at the blade is: $\alpha = \theta - \phi$. It is now possible to calculate the lift and the drag that this single section of the blade produces and their components on the vertical and horizontal axis:

$$L = \frac{1}{2}\rho U^2 c c_l \tag{2.3.3}$$

$$D = \frac{1}{2}\rho U^2 c c_d \tag{2.3.4}$$

$$F_z = Lcos\phi - Dsin\phi \tag{2.3.5}$$

$$F_x = Lsin\phi + Dcos\phi \tag{2.3.6}$$

Fig.14 shows the wing section, the angles, the velocities and the forces acting on the blade element:

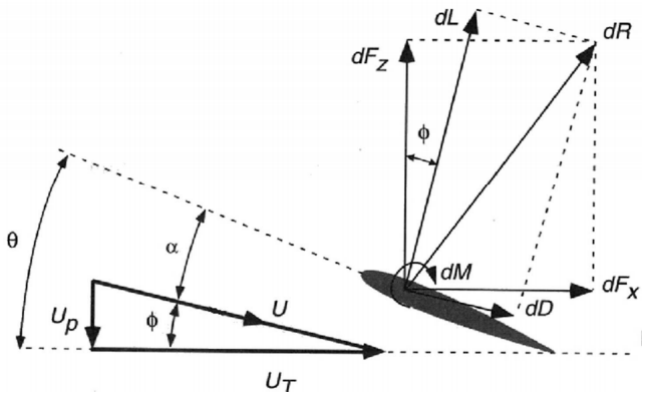

Figure 14: Blade section aerodynamics[2]

It is now possible to calculate the thrust, the torque and the power. Integration over

azimuth and radius provides the global results for the rotor.

$$dT = NF_z dr \tag{2.3.7}$$

$$dQ = NF_x r dr \tag{2.3.8}$$

$$dP = NF_x \omega r dr \tag{2.3.9}$$

where N is the number of blades. For a rotor blade it is acceptable to make the simplification of small angles so that $U = u_T$ and $\phi = \frac{u_P}{u_T}$. Thanks to the stall assumption and the compressibility effects neglected, the lift coefficient is linearly correlated with the angle of attack as $cl = a\alpha$ where a is the slope of the blade. Normalizing and undimensionalizing the quantities, the contribution that every section has on the thrust and the power in terms of coefficients in hover case is:

$$dC_T = \frac{\sigma a}{2}(\theta r^2 - \lambda r)dr \tag{2.3.10}$$

$$dC_P = \Big[\frac{\sigma a}{2}(\theta r\lambda - \lambda^2) + \frac{\sigma c_d}{2} r^2\Big] r dr \tag{2.3.11}$$

where λ is the inflow ratio and σ the solidity. Integrating the thrust coefficient along all the radius of the blade with the assumption of constant chord, linear twist and uniform inflow the total thrust coefficient of the blade is:

$$C_T = \frac{\sigma a}{2}\Big(\frac{\theta_{75}}{3} - \frac{\lambda}{2}\Big) \tag{2.3.12}$$

where θ_{75} is the pitch of the blade at 75% of the radius.
It is clear now, that the blade element theory gives the thrust and power coefficient as a function of the pitch angle and the inflow ratio, this means that the induced velocity is required to evaluate the thrust knowing just θ. For a vertical climb or a hover case the momentum theory provides an induced velocity of:

$$\lambda = \frac{V}{2\omega R} + \sqrt{\Big(\frac{V}{2\omega R}\Big)^2 + \frac{C_T}{2}} \tag{2.3.13}$$

Analyzing the power coefficient that can be written as:

$$C_P = \int \lambda dC_T + \int_0^1 \frac{\sigma c_d}{2} r^3 dr \tag{2.3.14}$$

it is possible to establish the difference between an induced power loss, which is the first term and results from the in-plane component of the lift, and a second term representing the profile power loss due to the drag of the wing in that section.

Combining the momentum theory with the blade element theory it is possible to define a non uniform inflow distribution on the radius of the blade. This can be done assuming that the distribution of the induced velocity on the radius depends just on the distribution of the thrust. Solving the following equation permits to find λ:

$$\lambda^2 + \Big(\frac{\sigma a}{8} - \lambda_c\Big)\lambda - \frac{\sigma a}{8}\theta r = 0 \tag{2.3.15}$$

for hover case where $\lambda_c = 0$ the induced velocity as a function of the radius of the blade is:

$$\lambda = \frac{\sigma a}{16}\Big[\sqrt{1 + \frac{32}{\sigma a}\theta r} - 1\Big] \tag{2.3.16}$$

which is a basic non uniform inflow distribution that can be improved by analyzing more in the detail the wake.
The previous equations are valid only for hover or vertical climb conditions, however, in forward flight the velocity of the helicopter must be considered with the components that the blade sees. The following equations of U_T, U_P and U_R, which is the radial velocity, can be used in every situation by setting the correct velocity of the helicopter:

$$U_T = r + \mu sin\psi \tag{2.3.17}$$

$$U_R = \mu cos\psi \tag{2.3.18}$$

$$U_P = \lambda + r\dot{\beta} + \beta\mu cos\psi \tag{2.3.19}$$

The Fig.15 helps to understand all the terms of the previous equations.[1][2][3][4] The

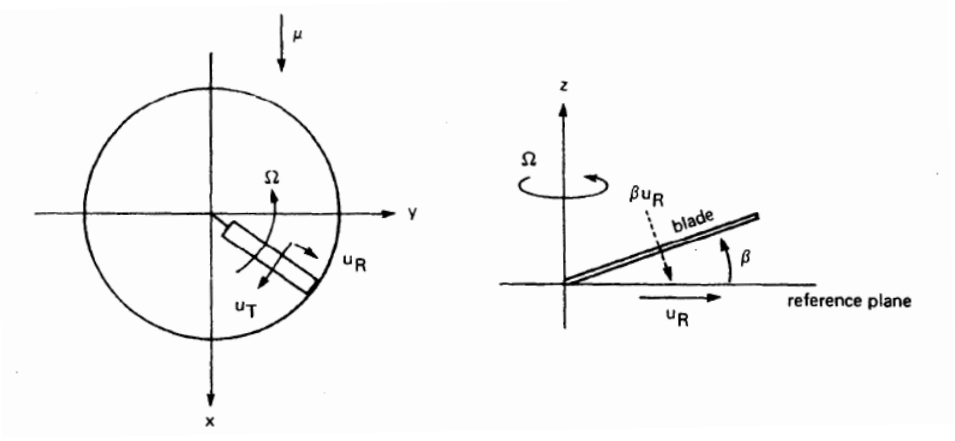

Figure 15: Blade section aerodynamics in forward flight[1]

results of the blade element theory or the blade element momentum theory if coupled with the momentum theory depend on the inflow velocity and its distribution at the rotor disk, therefore this theory suffers the accuracy of the employed induced velocity

field.

2.4 The vortex theory

In this chapter the vortex theory is discussed. This method permits to determine a more accurate induced velocity field by analyzing the wake of the rotor. The wake has a big impact on the induced velocity field since in a rotating wing the blade encounters its own wake and the wake from the previous blades many times.
The lift of the blade is connected to a bound circulation through the Kutta Joukowsky theorem:

$$\Gamma_b = \frac{1}{2} V c_l c \tag{2.4.1}$$

The vorticity is trailed into the wake from a three dimensional wing. To find the value and the direction of the induced velocity the vortex method applies the Biot-Savart law, the Kelvin's theorem and the Helmholtz law. Fig.16 shows the distribution of the bound vorticity along the blade and the trailed vorticity. In this case the bound vortex line is placed at $c/4$ and the evaluating points at $3c/4$

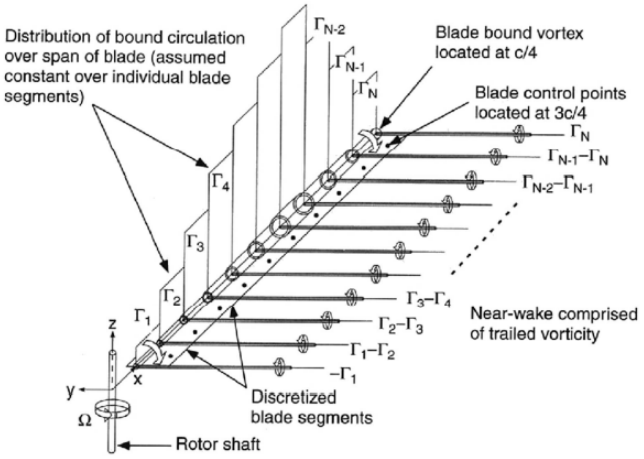

Figure 16: Blade representation in the vortex theory[6]

Biot-Savart law

The most important law in a vortex method is the Biot-Savart law, which permits the computation of the velocity induced by a vortex filament in an evaluation point P at r distance from the filament. If the filament has a circulation Γ, then:

$$d\vec{v} = \frac{\Gamma}{4\pi} \frac{d\vec{l} \times \vec{r}}{|r^3|} \tag{2.4.2}$$

To obtain the velocity at the point P induced by all the vortex lines an integration along its length is required. A non linear vortex (like the one following the shape of a wake) can be discretized in several straight segments and the velocity becomes:

$$V_i = \frac{\Gamma}{4\pi h}(cos\theta_1 - cos\theta_2)\, e_i \tag{2.4.3}$$

where h is the normal distance from point to filament and θ_1, θ_2 the angles between the filament line and the line that merges the beginning and the end point of the segment. Fig.17 helps the understanding of the formulation.

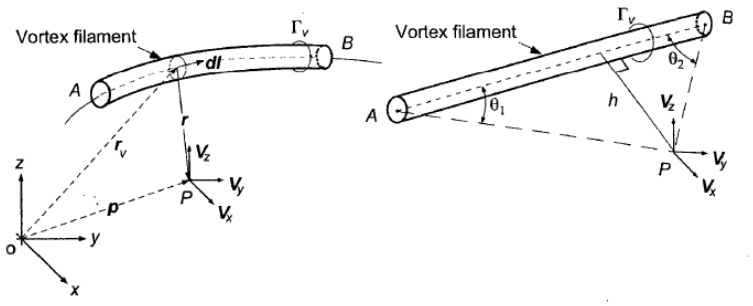

Figure 17: Induced velocity due to a vortex filament[1]

The Biot-Savart formulation has a singularity in $r = 0$, the induced velocity of a vortex line in a point that stands on the line is infinite. To solve the problem a vortex core radius must be implemented in order to achieve physical values of induced velocity. The vortex core radius (VCR) consists in a limitation on the velocity if the distance between the point and the vortex line is smaller than the VCR. Depending on the formulation of the code there are several different theories: [6][11]

- Rankine vortex model
  The vortex line is modelled as a solid body rotation so that:

  $$v_\theta = \frac{\Gamma}{2\pi r_c} r \tag{2.4.4}$$

  if the distance is smaller than the vortex core radius

- Oseen-Lamb model
  Thanks to a simplification of the Navier-Stokes equation the velocity becomes:

  $$v_\theta = \left(\frac{\Gamma}{2\pi r_c r}\right)\left(1 - e^{-\alpha r^{-2}}\right) \tag{2.4.5}$$

  with $\alpha = 1.25643$

- Vastitas

$$v_\theta = \left(\frac{\Gamma}{2\pi r_c}\right)\frac{r}{(1+r^{2n})^{\frac{1}{n}}} \tag{2.4.6}$$

Fig.18 shows the trend of the induced velocity a function of the distance to the vortex with different models of vortex core radius.
It is very difficult to find a correct value of the vortex core radius, however, depending on the method used in the code usually the range goes from the 30% to 80% of the chord.

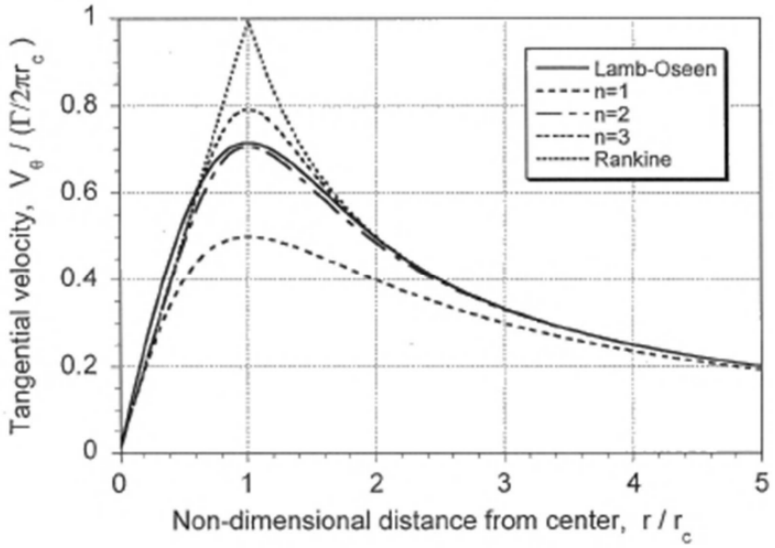

Figure 18: Velocity induced by a vortex line with different vortex core radius models[6]

Wake geometry and lattice method

Now that the induced velocity and the VCR limitation have been explained, the following step is to determine the shape of the wake in order to place the vortex line correctly. As mentioned before, the bound vorticity must be trailed in the helicopter wake from the blade tips and the trailing edge. From Fig. 16 it is easy to understand that if a constant loading along the radius is assumed then the vorticity would be trailed just at the root and at the tip of the blade. The trailed tip vortex has the shape of a helix due to the combination of the axial velocity (in hover it is just the induced velocity) and the rotational motion of the blade. Clearly the assumption of constant lift on the blade can not be always accurate; assuming a more general case, the trailing vorticity will move from the trailing edge of the blade at every position of the radius depending on its discretization. The wake then consists in helical vortex sheets behind each blade.

All these vortices quickly converge in a bigger vortex near the tip. Summarizing: there is a bound vorticity due to the lift, a trailing vorticity due to the radial variation of lift distribution and a shed vorticity due to the azimuthal changes in the bound vorticity. The presence of a shed vorticity means that the trailing vorticity varies along its filament; this effect occurs mainly in forward flight. It is possible to define the trailing and the shed vorticity as:

$$\gamma_t = \left.\frac{\partial \Gamma}{\partial r}\right|_{\psi-\phi} \tag{2.4.7}$$

$$\gamma_s = -\left.\frac{1}{U_T}\frac{\partial \Gamma}{\partial \psi}\right|_{\psi-\phi} \tag{2.4.8}$$

where ϕ is the wake age. Fig.19 shows the trailing and the shed vorticity in a rotor wake.

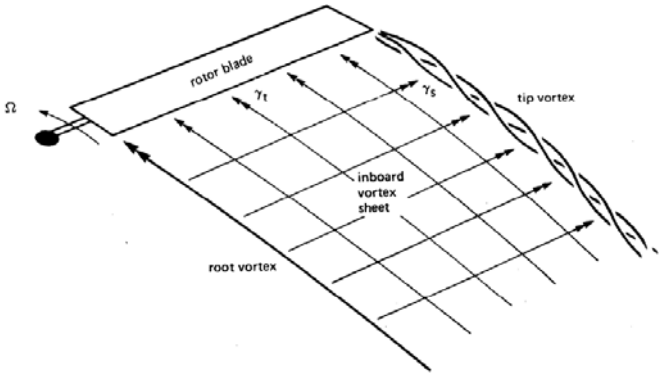

Figure 19: Trailed and shed vorticity in rotor wake[1]

Near the tip there is a drop on the bound circulation due to the tip losses; the high negative gradient of the circulation produces a strong negative trailed vortex near the tip that induces a strong downwash.

This method produces a non uniform inflow distribution, which highly increases the accuracy of the results provided by the blade element theory. This phenomenon occurs because the strong tip vortices of the previous blade encounter the following blade varying the induced velocity, especially in hover case where the helicopter wake is not carried away by the free stream velocity. In forward flight there is an important azimuthal variation of the induced velocity that produces a large harmonic content on the loading.[1][13]

The most commonly used wake model is the lattice model that consists in a high number of small straight vortex elements that can easily describe the variation of bound vorticity along radius and azimuth. The model must be used in order to avoid the integration problem on a non-straight line of the trailed vorticity. Usually the evaluation point is placed in the middle of two vortices or respecting the area rule

(every ring has the same area of the previous one), of course, a adequate model for the vortex core radius is required. The discretized trailing and shed vorticity become:

$$\gamma_t = \Gamma(\psi - \phi, r_{j+1}) - \Gamma(\psi - \phi, r_j) \tag{2.4.9}$$

$$\gamma_s = -\Gamma(\psi + \Delta\psi - \phi, r_j) + \Gamma(\psi - \phi, r_j) \tag{2.4.10}$$

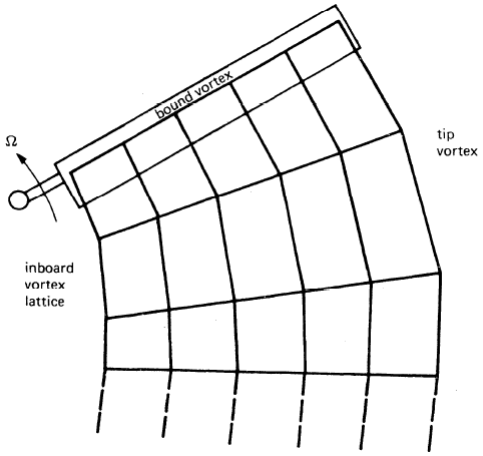

Figure 20: Example of the lattice model[1]

The geometry of the wake depends on the velocity of the helicopter, the rotational speed and the induced velocity which is by itself function of the geometry of the wake. An iteration between the Biot-Savart law and the position of the points of the lattice model is required in a non uniform inflow calculation. This make the vortex theory more expensive than the previous theories and the prescribed helix form is just a coarse simplification of this method. Usually to simplify the modeling only the position of the strong tip vortices is calculated with a high level of accuracy. Considering a non rotating tip-path-plane orientation axis system with x,y,z the position of the wake element, ϕ the age of the wake and ψ the dimensionless azimuth and β_0 the coning angle, considering just the mean convention velocities that have components λ and μ in the tip path plane, the current position of the wake element is:

$$x = rcos(\psi - \phi) + \mu\phi \tag{2.4.11}$$

$$y = rsin(\psi - \phi) \tag{2.4.12}$$

$$z = r\beta_0 - \lambda\phi \tag{2.4.13}$$

For N blades the azimuth angle of the mth blade is

$$\psi_m = \psi + m\Delta\psi \tag{2.4.14}$$

with $m = 1$ to N and $\Delta\psi = 2\pi/N$ so that the vertical position becomes:

$$z = r\beta_0 + \int_0^{\phi} \lambda d\phi \tag{2.4.15}$$

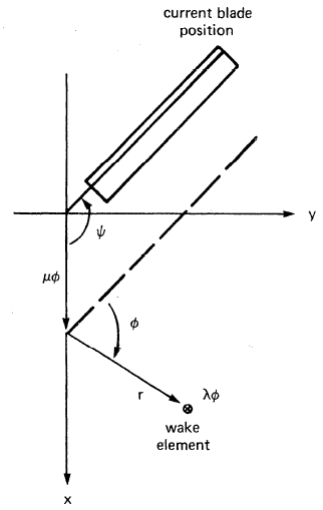

Figure 21: Geometry of the wake[1]

A free wake model analysing the geometry of the wake due to the induced velocity at every iteration is required for high accuracy inflow fields, especially when the speed of the helicopter is not high enough to create a sufficient distance between the wake of the first blade and the second one. The tip vortex encountering the incoming blade induces a large aerodynamic load on that blade. If the vortex is below the blade it induces a downwash that goes to zero just when the blade is perfectly above the vortex. The bound vorticity has the same effect. The spanwise gradient on the bound circulation indicates that there is a trailed vorticity in the wake behind the blade induced by the tip vortex of the preceding blade[1]. Fig.22 shows the difference between the vortex geometry with a free-wake model with a fixed model that do not permit the variation of the structure of the wake due to an induced velocity modification. It is clearly visible that the rigid method is accurate only in the near field but after one rotation the difference between the freewake, perfectly matching the experiment data, and the rigid structure wake becomes relevant for a high accuracy simulation. This can be easily seen in the side view where the importance of having a free wake method is clear. A

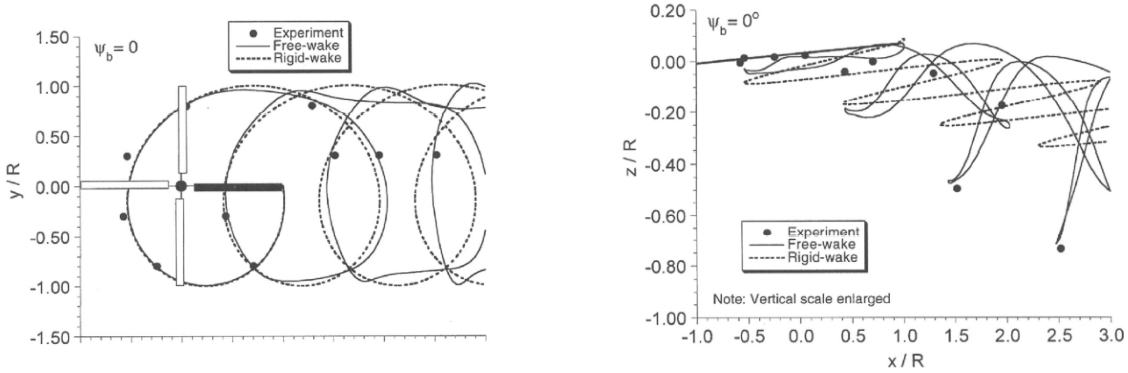

(a) Vortex geometry top view

(b) Vortex geometry side view

Figure 22: Vortex geometry comparison between freewake, rigid wake and experimental data[1]

non negligible effect for a code that uses the free wake method and for the performance of the helicopter is the BVI (Blade vortex interaction). This occurs when the blade encounters a vortex line and the vorticity of the blade changes the natural shape of the vortex line. This phenomenon happens mainly for the tip and root vortex lines of the previous blade especially if the rotor has 4 or more blades and a low descending speed. There are 3 different types of BVI depending on the direction between the blade and the vortex line[7][12]:

- Parallel BVI: occurs when vortex line and the blade axis are parallel. They have a strong effect on the noise of the rotor

- Perpendicular BVI: occurs when vortex line and the blade axis are perpendicular and in parallel planes

- Oblique BVI: the angle between the blade and the vortex line is different from the previous two.

At the start of the BVI the vortex is located in an upstream position and moves towards the airfoil leading edge as shown if Fig.23.
The FT-Freewake code uses specific models for the roll up, the BVI and the growth of the vortex core radius that helps the stability of the code and permits the aging of the wake, these models will be discuss in chapter 3 where both Gensim and FT-Freewake will be introduced with more accuracy since these two codes do not use just general theory but they are also based on empirical data.

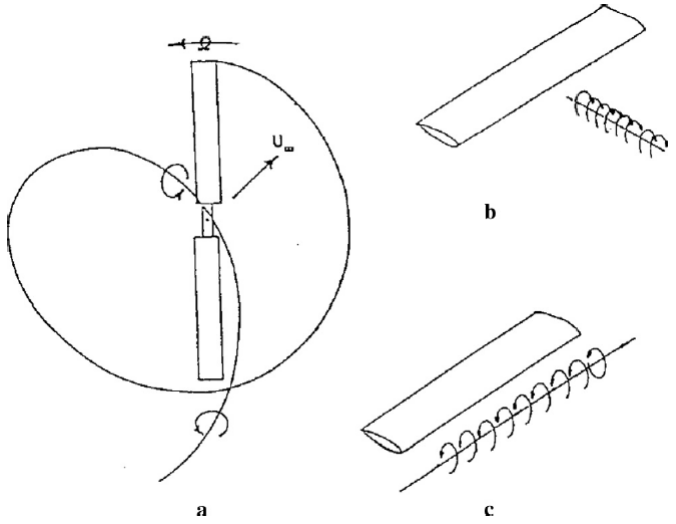

Figure 23: Blade vortex interaction: parallel and perpendicular[12]

2.5 Helicopter performance

In this chapter a review of the total performance of a helicopter will be done, analyzing the power required in different flight situations. A large use of the adimensionalized coefficients is binding in order to make the data more comparable. An accurate study of the performance of the helicopter is important to understand the behavior of the machine in all the different conditions, finding the best solution, and optimizing the mission planning. Before introducing the required power in different flight conditions, the available power is discussed. This is the power that the engines can provide counting the different losses and efficiency. The maximum power that an engine produces is not constant, since there are some variables as the altitude and the temperature that can significantly reduce the available power. All the inboard systems like the generator or the oil pump and every accessory required for the navigation reduce the power that the helicopter can use for the flight and this must be taken into account. The tail rotor uses an amount of power that increases as the speed decreases. The most common method is to find the total power required by multiplying for a coefficient the main rotor power:

$$P_{req} = \frac{1}{\eta} P_{rotor} \tag{2.5.1}$$

with η that depends on the flight conditions and varies from helicopter to helicopter. Usually it goes from 0.80 in hover to 0.85 in forward flight. The coefficient must also consider the losses due to the transmission efficiency which is usually around 0.97.
As it has been done for the momentum theory the first flight case analyzed will be the hover or vertical flight where in the power coefficient (and in the total power) there

can be analyzed three different terms:

$$C_P = C_{P_i} + C_{P_o} + C_{P_c} \tag{2.5.2}$$

C_{P_i} is the induced power coefficient, C_{P_o} is the profile power coefficient and C_{P_c} is the climb power coefficient. The first one is connected with the energy dissipated by the rotor wake by imparting a momentum to the air, the second one is connected to the viscous drag dissipation of energy of the blades and the third one is connected with the power that the helicopter needs to climb and it is a function of the power required in hover.

$$C_{P_i} = \int_{r_R}^{B} \lambda_i dC_T \tag{2.5.3}$$

$$C_{P_o} = \int_{r_R}^{B} \frac{\sigma c_d}{2} r^3 dr \tag{2.5.4}$$

$$C_{P_c} = \lambda_c C_T \tag{2.5.5}$$

A parameter that is usually analyzed as a function of C_T and C_P is the θ_{75} thanks to the momentum theory combined with the blade element theory:

$$\theta_{75} = \frac{6C_T}{\sigma a} + \frac{3}{2}\lambda \tag{2.5.6}$$

A new parameter that express the rotor hover efficiency is the figure of merit that will have a large use in this thesis and it is defined as:

$$FM = \frac{T\sqrt{\frac{T}{2\rho A}}}{P} = \frac{\frac{C_T^{3/2}}{\sqrt{2}}}{C_P} \tag{2.5.7}$$

In hover condition some typical numbers of the profile power are around 30% and 70% for the induced loss power.
One way to understand the power required for climbing is to use the induced velocity evaluated in hover and a ΔP to calculate the climb velocity permitted by the difference between the power required in hover and the available power:

$$V = \frac{\Delta P}{v_h} \frac{2v_h + \Delta P/T}{v_h + \Delta P/T} \tag{2.5.8}$$

if $V < \sqrt{T/2\rho A}$ the formulation becomes:

$$V = 2\frac{\Delta P}{T} \tag{2.5.9}$$

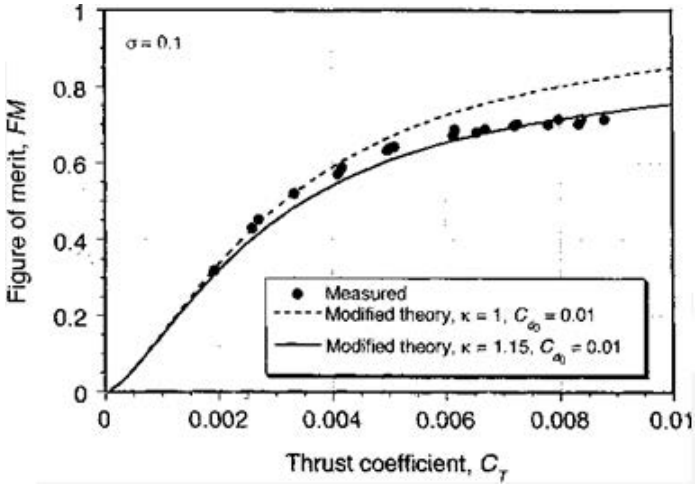

Figure 24: Thrust coefficient vs figure of merit[4]

In forward flight the power required to move the helicopter through the air must be added to the power coefficient equation and it is called parasite power:

$$C_P = C_{P_i} + C_{P_o} + C_{P_c} + C_{P_p} \tag{2.5.10}$$

except for the induced power that has the previous formulation, the other terms are:

$$C_{P_o} = C_{Q_o} + \mu C_{H_o} \tag{2.5.11}$$

$$C_{P_p} = \frac{DV}{\rho A(\Omega R)^3} \tag{2.5.12}$$

$$C_{P_c} = \frac{V_c W}{\rho A(\Omega R)^3} \tag{2.5.13}$$

At high speed the stall and the compressibility effects that were neglected in the blade element theory are significant, so the results with this theory could underestimate the real result. The determination of the drag will not be discussed in this thesis but for a low accuracy calculation a method that uses an equivalent frontal area instead of the complex shape of the helicopter can be used. Fig.25 shows the trend of the power in level flight for different speeds. Analyzing with more details the graph it is easy to understand that for every helicopter there is an optimal speed of flight that permits to use as less power as possible, this means for example, that if the helicopter needs to increase its altitude quickly the best speed to do it is where the total power of the graph is at its minimum. This considering an available power constant with the speed. Obviously that point is also the point of best endurance. For hover or low flight speed the presence of the ground can also reduce the required power.
From Fig.25 the speed at which the rate of change of power with velocity is minimum

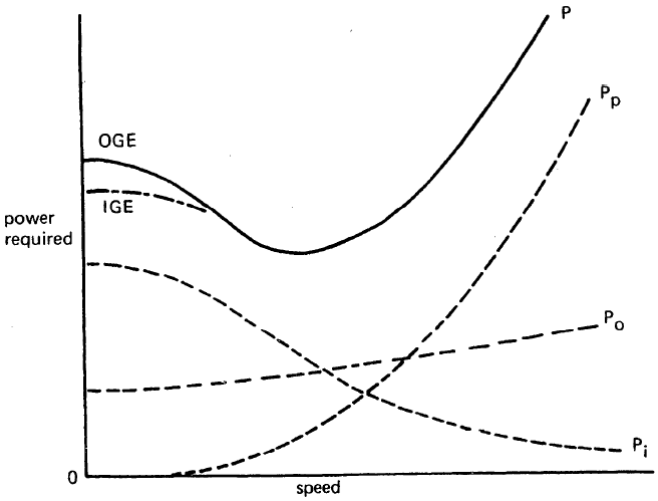

Figure 25: Power required in level flight[4]

can be identified (best range and best descend angle). This can be easily done by drawing the tangent of the curve passing from the origin of the axis. Both of this points are a function of the induced velocity in hover defined thanks to the momentum theory.

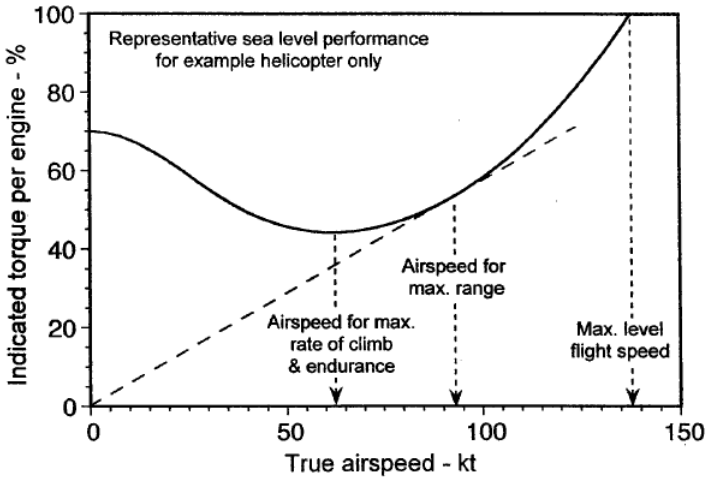

Figure 26: Best endurance and max range speed[3]

Clearly the maximum level flight speed that the helicopter can reach is in the right side of the graph where the curve surpasses the available power value. It can also happen that the maximum speed is not determinated by a engine power but also by aerodynamic effects as the stall of the retreating blade or compressibility effects on the advancing side.

The gross mass of the helicopter affects the power required by the exponential function (2.2.47), this power also depends on the altitude and the temperature. By increasing

the altitude the helicopter will need more power to fly with constant weight. The Fig.27 shows the take of weight against the required power; it is also possible to note that if the pressure altitude or the density altitude increases the power increases.

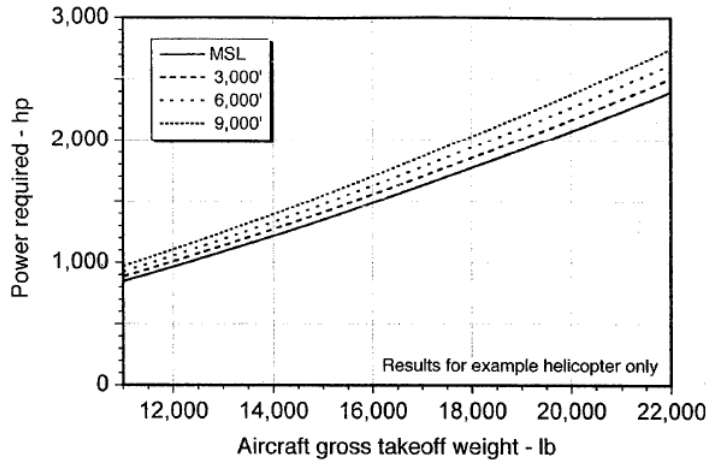

Figure 27: Required power vs take off weight for different altitudes[3]

The available power is not constant, it decreases as the altitude increases, therefore a helicopter that can hover at the sea level might not be able to hover at a higher altitude due to the increase of the required power but also due to the decrease of available power. By defining the excess power as the difference between the required power and the available power, the hover ceiling is defined as the point at which the excess power becomes equal to zero.

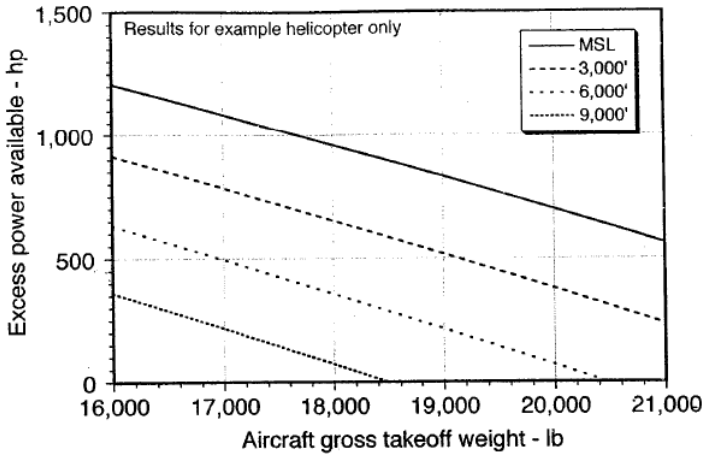

Figure 28: Excess power for different altitudes[3]

The vertical speed of a helicopter is called vertical rate of climb and it also affects the required power linearly. Usually it is measured in ft per minute and for a helicopter in hover condition it is:

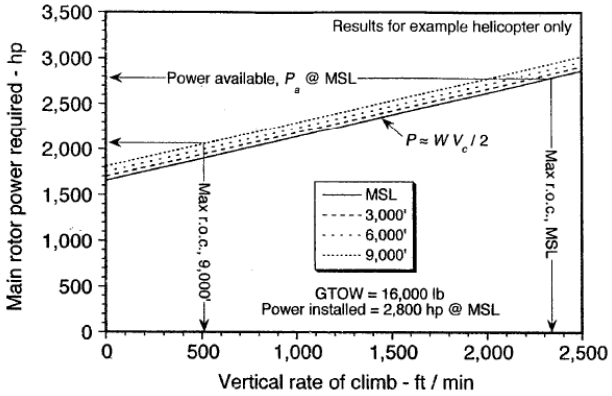

Figure 29: Rate of climb versus required power[3]

The point with the maximum rate of climb for a helicopter does not occur in hover; it occurs when the available power is at its maximum. Considering a constant excess power the trend of the rate of climb follows exactly the excess power. This means that the rate of climb decreases from a maximum point to a lower point condition, the trend is mirrored for an increase of speed. Fig.30 explains this phenomenon.

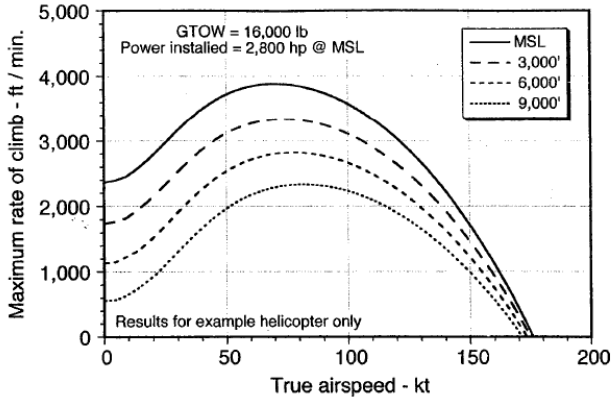

Figure 30: Rate of climb versus level velocity[2]

Clearly an increase of the altitude shifts down the rate of climb especially for low values of true airspeed.

Now that the main parameters that affect the helicopter performance have been summarized, the ground effect phenomenon must be explained in order to understand the reasons that reduce the required power of the helicopter if the flow is not far above an object. Fig.25 showed how a reduction of the power occurs in hover condition or low forward flight speed. Because the flow must be streamlined to the ground, the rotor slipstream tends to rapidly expands and it approaches the surface; this modifies the slipstream velocity and also the induced velocity so that for a given power the rotor produces a higher thrust. This phenomenon is still not well explained but the test data

suggest a dependence also on the rotor loading. The following image shows the shape of the wake in ground effect and out of ground effect.

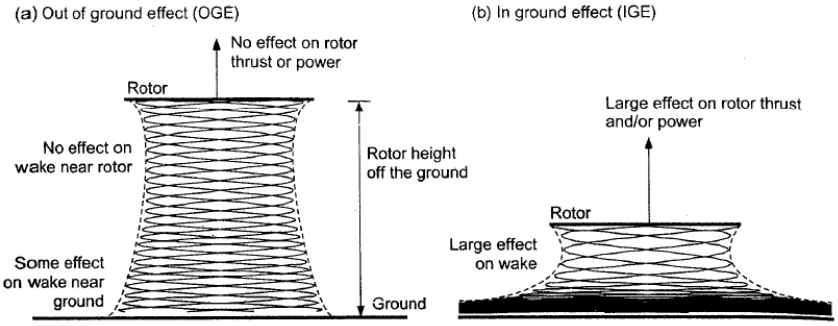

Figure 31: Ground effect[1]

The decrease of the power is visible for a distance to the ground equal to the diameter of the rotor. There is also a reduction of the profile power due to the induced velocity reduction.
A simple estimation of the ground effect is made by considering the power constant:

$$\frac{T}{T_\infty} = \frac{1}{1 - \frac{(R/4z)^2}{1+(\mu/\lambda_i)^2}} \tag{2.5.14}$$

where z is the altitude from the ground.
A more accurate model considers also the loading of the disk even if the effect is minor. The formulation becomes:

$$\frac{T}{T_\infty} = \frac{1}{1 - \frac{\sigma c_l \lambda_i}{4C_T} \frac{(R/4z)^2}{1+(\mu/\lambda_i)^2}} \tag{2.5.15}$$

Which gives accurate result for $z/R > 0.5$.
Fig.32 shows the ratio between the thrust achieved in ground condition and out of ground effect[1][2][4].

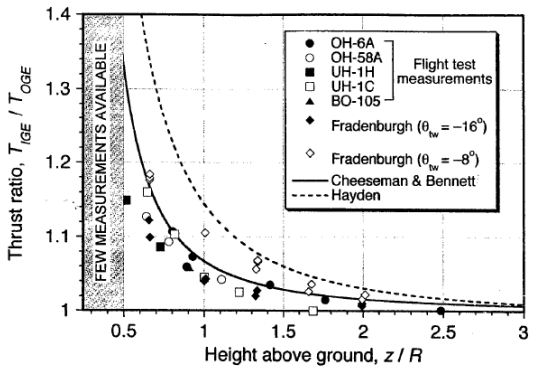

Figure 32: Thrust ratio for ground effect[3]

3 Gensim, FT-Freewake and their coupling

To analyze the performance of the helicopter with an accurate induced velocity field, in this thesis a blade element method code called Gensim, coupled with a free wake vortex method code called FT-Freewake, was used. Before introducing the coupling it is important to summarize the features of both of them including the possible input parameters, the effects that they can analyze and the effects that are neglected.

3.1 Gensim

Gensim is an Airbus internal simulation tool, used in flight mechanics, loads calculation and performance. The physical modelling of steady and unsteady performance is based on blade element theory. It performs a 6 DOF helicopter trim. Due to its limited complexity it can be used to evaluate a very different and large amount of data and it provides accurate result for special applications as malfunctioning of one engine, jettisoning, weapon separation and variation of the initial shape of the helicopter by adding accessories for example.
It is possible to simulate all flight conditions. Every part of the helicopter is analyzed separately and than put together in the overall helicopter equations. The code uses the Newton-Rapson iteration method to converge.
The blade is divided in 15 segments and for every segment the code evaluates its aerodynamics and airfoil characteristics and integrates along the radius to find the total values. Airfoils table provide the lift coefficient, the drag coefficient and the momentum coefficient for different Mach numbers and angles of attack.
For the geometric modeling of the blade the following inputs are needed:

- Chord-taper
- Twist
- Aerodynamic center
- Blade tip geometry

All these parameters must be defined as a function of the blade span.
The blade equation of motion is defined as:

$$M_{mass} + M_{aero} + M_{spring} + M_{damp} = 0 \tag{3.1.1}$$

The forces and the moments are evaluated for every axis and transformed in the rotor hub frame system. With the same approach the tail rotor is evaluated; in this thesis case the Fenestron model is used.
The fuselage is evaluated as a rigid body, the mass forces and their momentums are calculated from the acceleration vector thanks to the Newton formulation that gives the inertia force and the mass moments. The aerodynamic loads that include also the download must be added to perform the equilibrium condition.[14][15][16]
The final formulation for the entire helicopter becomes:

$$P = P_{mr} + P_{fu} + P_{tr} + P_{tp} + P_{eb} = 0 \tag{3.1.2}$$

$$M = M_{mr} + M_{fu} + M_{tr} + M_{tp} + M_{eb} = 0 \tag{3.1.3}$$

With mr main rotor, tr tail rotor, tp tail planes, fu fuselage and eb external bodies.
The trim condition aims to find all the position angles, forces, momentums and powers of the helicopter in a specified flight condition.
After setting all the parameters that regard the geometry of every part of the helicopter, the power limitations due to engines or transmission, the angular velocity function, the tolerance of the calculation, the special conditions as ground effect or one engine inoperative, the code requires the flight condition with the following inputs:

- Gross weight
- V_x
- V_z
- Altitude
- Temperature

The V_y is also required but it is not considered as a main parameter for normal performance analysis. The temperature can be defined as an absolute temperature or a variation from the ISA conditions. The code also permits to evaluate the boundary performance condition by calculating a 7 DOF system adding the power to the previous equations in order to understand the performance limits of the helicopter.
Analyzing with more accuracy the Gensim inflow model highlights the importance of coupling the blade element theory with the free wake. Gensim applies two types of corrections on the simple uniform induced velocity evaluated by the momentum theory as:

$$v_i = \sqrt{\frac{T}{2\rho A}} \tag{3.1.4}$$

The first correction regards the average value of the induced velocity that, compared with flight data, results too low. It uses two correction factors that aim to increase the inflow. The first one affects the result in both hover and forward flight conditions and depends mainly on the density of the air. This parameter is almost constant and it increases the induced velocity of about 10%. The second parameter acts in forward flight and is a function of the speed of the helicopter. The following formulation explains

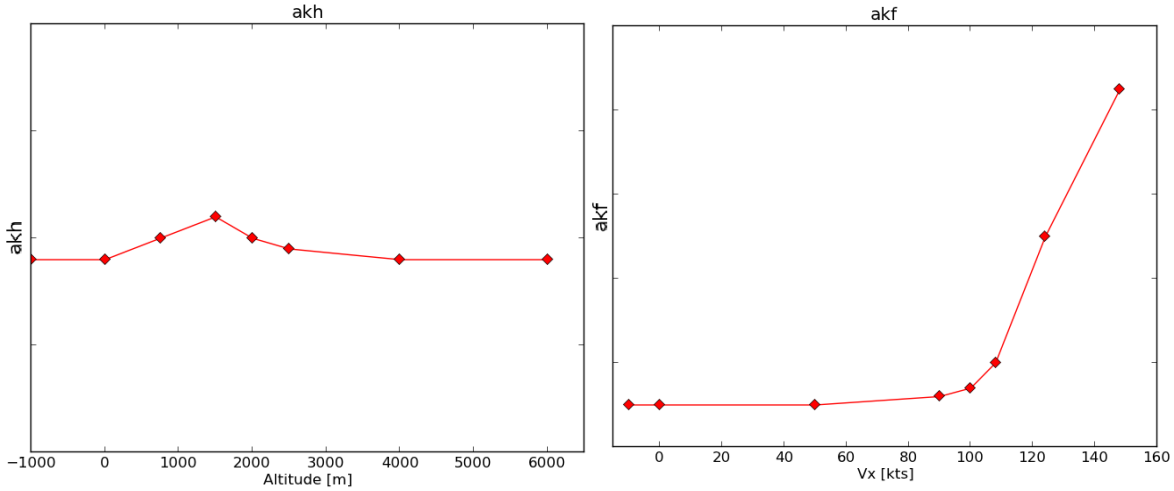

(a) Hover correction factor

(b) Forward flight correction factor

Figure 33: Correction factors of the induced velocity

the use of akf and akh:

$$V_{io} = \frac{1}{\sqrt{\frac{V_{xy}^2}{akf^2} + \frac{(V_z - V_{io})^2}{akh^4}}} \tag{3.1.5}$$

These two parameters are empirically determined and show how especially in fast forward flight a uniform inflow model underestimates the average induced velocity of a helicopter.

The second correction acts only in forward flight since the inflow model in hover is completely uniform. In forward flight Gensim uses an induced velocity distribution which is small at the leading edge of the disk and higher at its trailing edge. The local induced velocity for a helicopter in forward flight varies along azimuth and radius as:

$$v_l = v_i\left(1 + \kappa\frac{r}{R}cos\psi\right) \tag{3.1.6}$$

where κ is a distortion factor that can be considered as one, just in fast forward flight. The formulation leads to Fig.34 induced velocity distribution considering a κ equal to one and v_i equal to 10 m/s.

Gensim evaluates the distortion factor thanks to a more accurate and complex inflow model: Pitt and Peters. In this formulation only the static part will be analyzed but

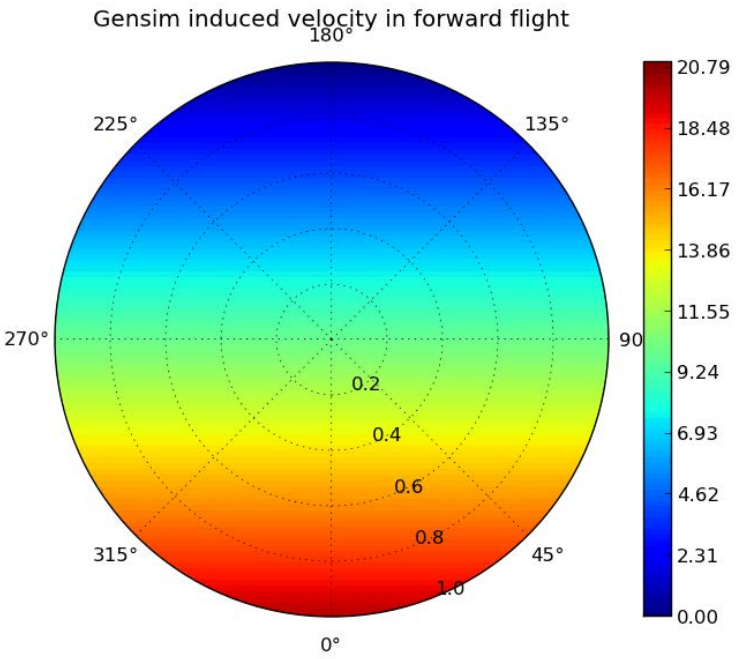

Figure 34: Gensim induced velocity in forward flight

the model permits also a more complex and dynamic evaluation. In a steady pitching or rolling motion the rotor applies a first harmonic aerodynamic motion. Pitt and Peters assumes that also the inflow has a first harmonic distribution. Starting from the formulation:

$$v = v_0 + x(v_c cos\psi + v_s sin\psi) \tag{3.1.7}$$

Curtis demonstrated that the inflow components v_c and v_s are correlated by a gain matrix to the aerodynamic pitching and rolling moment coefficients as:

$$\begin{bmatrix} v_s \\ v_c \end{bmatrix} = \begin{bmatrix} \frac{-K}{v_0} & 0 \\ 0 & \frac{-K}{v_0} \end{bmatrix} \begin{bmatrix} c_l \\ c_m \end{bmatrix} \tag{3.1.8}$$

where K depends on the wake model used. Note that in this formulation the momentum theory is used just to find v_0. The problem of this theory is the extension of the gain matrix to forward flight. Peters extended the gain matrix using the unsteady actuator theory and wrote a function between the induced velocity and the thrust coefficient as:

$$\begin{bmatrix} v_0 \\ v_s \\ v_c \end{bmatrix} = \begin{bmatrix} L \end{bmatrix} \begin{bmatrix} c_T \\ c_l \\ c_m \end{bmatrix} \tag{3.1.9}$$

where the gain matrix L is defined as:

$$L = \begin{bmatrix} \frac{1}{2v_T} & 0 & \frac{15\pi}{64v_m} tan\frac{\chi}{2} \\ 0 & -\frac{4}{v_m(1+cos\chi)} & 0 \\ \frac{15\pi}{64v_T} tan\frac{\chi}{2} & 0 & -\frac{4cos\chi}{v_m(1+cos\chi)} \end{bmatrix} \tag{3.1.10}$$

in which $v_T = \sqrt{\mu^2 + \lambda^2}$, χ is the wake skew angle defined as $tan^{-1}\mu/\lambda$ and v_m is a mass flow parameter:

$$v_m = \frac{\mu^2 + \lambda(\lambda + v_0)}{v_T} \tag{3.1.11}$$

This method permits to find the distortion factor that varies the radial and azimuthal inflow model, however the difference between this models and the real inflow distribution is still not neglectable, this aspect will be highlight in chapter 6 that shows the results coming from the free wake method[13][14][17][18].

3.2 FT-Freewake

FT-Freewake is a Fortran based code written by DLR that aims to find the induced velocity field of a rotor. It uses the vortex theory with a complete freewake method to find the shape of the wake.
The code is divided in two main sections that iterate each other, the first one finds the shape of the wake and the position of every vortex segment, the second one evaluates the induced velocities along the 3 axis at any number of radial and azimuth position. The wake geometry iteration can be done at a reasonable time interval with the chosen wake mesh discretization.
For discretizing the wake, the code uses the principle of the multi-wake structures. This method permits to find the total number of vortices along the azimuth as:

$$N_A = N_\psi N_T \tag{3.2.1}$$

where N_ψ is the azimuthal number of vortices of one wake and N_T is the number of turns of each blade wake. This permits to find out the total number of nodes of the entire wake as:

$$N = (N_A + 1)N_R N_B \tag{3.2.2}$$

with N_R the radial number of wake nodes on one blade and N_B the number of the blades. Returning to the lattice model, explained in chapter 2.4, the number of trailed vortices and shed vortices are:

$$N_t = N_A N_R N_B \tag{3.2.3}$$

$$N_s = N_A(N_R - 1)N_B \tag{3.2.4}$$

The induced velocity of all vortex segments must be computed $N_t(N_t + N_s)$ times and the influence of one vortex must be evaluated for each time step. This means that the total number of vortices evaluations goes up to:

$$N_{tot,\omega} = 2N_f N_\psi^3 N_R^2 N_T^2 N_B^2 \tag{3.2.5}$$

with N_f the total number of single vortices evaluations.

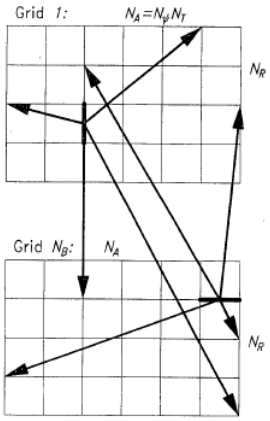

Figure 35: Principle of the grid structure and grid-grid interaction[11]

The second step uses the Biot-Savart law to evaluate the induced velocity in all the grid points. Remembering that this type of codes aim to reduce the computational time compared with CFD, a small discretization should not be used, however a coarse discretization might not produce an automatic tip vortex roll up. The coded uses a roll up model that after an azimuthal distance concentrates all the vortices in the radial position of the real tip vortex, this position is in the center of vorticity defined as:

$$r_t = \frac{\int_{r_1}^{r_2} \frac{d\Gamma(r)}{dr} r dr}{\Gamma_2 - \Gamma_1} \tag{3.2.6}$$

The bounds of vorticity summing up into a vortex are evaluated where $d\Gamma/dr = 0$ and at the blade tip where $\Gamma = 0$

In general the velocity field induced by a vortex is measured by the energy of the vortex. Considering l_0 the initial length of the segment and Γ_0 its initial vorticity, if the vortex is stretched multiple times and the vorticity remains constant it will affect a larger portion of wake. To solve this problem the code instead of keeping constant the circulation to preserve the energy conservation law uses the product Γl so that a stretched vortex has less circulation. This can be studied by analyzing the Biot-Savart law for a non infinite segment length vortex and it is important for two

main situations: when trailed vortices from different radial stations converge in the tip vortex and second within the wake development in time where the vortex are free to be stretched and shortened.
The vortex core radius is an important parameter that permits to solve the problem of the singularities when the vortex is in the same position of the evaluating point. The VCR is also modified by the age of the wake: to reduce the vortex global induction the vortex growth must be applied with the ageing. Thanks to test data, DLR introduced a formulation for the vorticity:

$$\Gamma = \frac{2\pi}{1.2763}\Delta V_{max} r_c \tag{3.2.7}$$

where ΔV_{max} is the maximum peak to peak velocity difference. Comparing the bound circulation strength at different azimuth it is possible to find a time decay function, if $\Gamma(0)$ is the circulation at the beginning of the wake:

$$\Gamma(\psi_V) = \Gamma(0) e^{-0.44\frac{\psi_v}{2\pi}} \tag{3.2.8}$$

To permit a better set up, the code treats the vortex core radius as an input variable. In order to analyze the BVI (blade vortex interaction) the code uses an adaptive grid remeshing: if a node of the mesh is close to another vortex line then a much finer mesh is locally introduced. The trailed and the shed vorticity are split in a higher number of vortices with a prescribed normalized strength distribution in order to approximate correctly the continuous vorticity sheet on the blade.

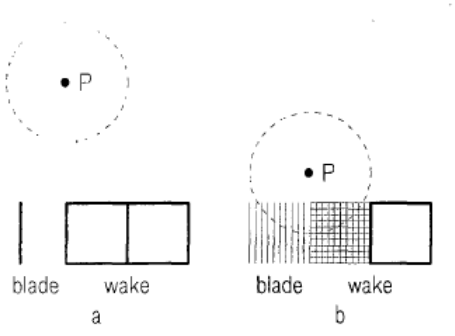

Figure 36: Adaptive grid remeshing[11]

Fig.36 shows how the adaptive grid mesh works when the blade passes near or crosses a vortex line.
To increase the performance of the code and decrease the computational time it is possible to parallelize the simulation on several CPU's.
The input coefficients included in FT-Freewake are[11]:

- Radial discretization
- Azimuthal discretization (must be the same used by Gensim)
- Number of available CPU's
- Bound vortex core radius
- Trailed vortex core radius
- Wake length: length of a vortex line in revolutions
- Number of revolutions (must be higher than the wake length)
- Convergence method: Adam Bashford (linear multistep method for ordinary differential equations) or Euler explicit (basic explicit method)
- Aborting tolerance
- Multiple output parameters

3.3 The coupling between Gensim and FT-Freewake

As already mentioned the coupling between these two codes is made for increasing the accuracy of the induced velocity that Gensim uses to evaluate the performance of the helicopter. The coupling is provide by a Python script written by DLR that permits the iteration cycle between the vortex theory and the blade element theory. Fig.37 shows the steps of the procedure:

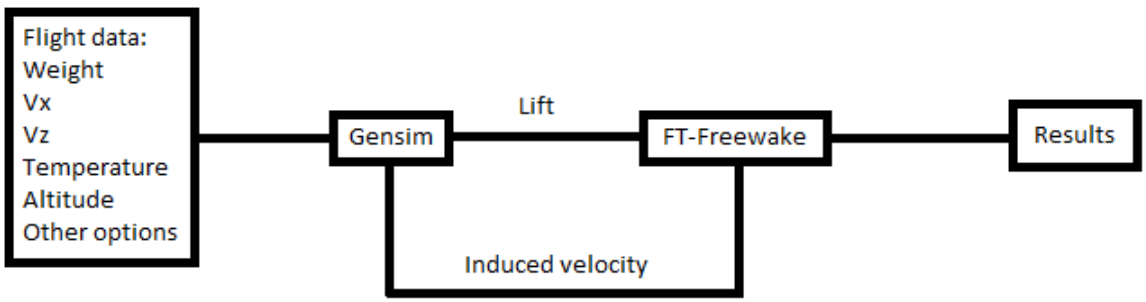

Figure 37: Coupling steps

The procedure starts by setting the input data regarding the helicopter flying conditions in Gensim: in the first iteration Gensim uses its own inflow model without any correction. Thanks to the coupling script Gensim passes to the Freewake the geometry of the rotor and its discretization. Gensim outputs the lift distribution along the radius

and the azimuth which permits to calculate the bound vorticity in every point of the disk thanks to the Kutta condition. With this distribution FT-Freewake is able to evaluate the wake and the induced velocity field as explained before.
FT-Freewake output is the induced velocity field at the rotor disk which will be used in the second iteration of Gensim that replaces with the corrected one its own model and the steps restart until convergence. At the very last iteration since Gensim computational time is small the procedure is terminated with another Gensim cycle.
Some changes have been applied to both codes to permit their coupling: the bound vortex has been removed in the induced velocity calculation of the freewake otherwise it would be redundant since the lift is provided by Gensim, obviously its influence on the shape of the wake is considered in order to analyze properly the BVI. The Gensim tiploss model has been completely removed since the zero lift at the tip must be provided by the correct value of the induced velocity. The tiploss model that Gensim uses evaluates an equivalent radius thanks to a coarse wake model and stops the integration for the total thrust at that radial position without changing the forces parameters.
The coupling permits the user to decide the number of iterations between Gensim and FT-Freewake; this number must be chosen trading off the complete convergence of the results and the computational time. The convergence will be discuss in chapter 6. A relaxation factor has been implemented in order to reduce the possibilities of divergence that may occur when the Gensim inflow model and the free wake first result are too far appart.
Another task of the coupling script is to rotate the coordinates from the Gensim to FT-Freewake axis and vice versa since they have different reference axis. Gensim z-axis heads downwards, x forward and y heads on the right. FT-Freewake axis reference has a z-axis pointing upwards, x forward and y on the left.

4 Main rotor models

In this thesis the model of three main rotors have been created and analyzed. Two of them are used for the validation of the code, comparing results against experimental data and CFD analysis. The two validation models consist in the main rotor stand alone analysis. The experimental data have been collected by NASA in the early 80s to understand the wake shape and behavior, to have a general prediction of the thrust and to achieve general knowledge on rotating wings. This models have been analyzed prescribing the pitch angle in an untrimmed condition.
The third model is the AIRBUS Helicopters main rotor for the H135: the complete modeling of the entire helicopter have been created and analyzed. The choice of the validation rotor is made by considering the simplicity of the blade in order to reduce the modelling error, the high level of accuracy that bench test permits and the large amount of data available and searchable.
As explained in chapter 3, the freewake is used to correct the inflow model of Gensim. This model uses the momentum theory and provides an uniform inflow. The first rotor analyzed is an almost uniform lift distribution over the disk, in order to have a small error from the coupled blade element theory and momentum theory.
The second model is chosen in order to increase the deviation from the momentum theory. Since the discrepancy between the uniform inflow assumption and the free wake formulation increases for untwisted straight blades, the Caradonna-Tung case has been chosen.

4.1 Carpenter rotor

The rotor analyzed by Paul J. Carpenter [9] is a full scale two blades rotor with a NACA 0012 wing profile along the radius. The chord is constant between the 15% and the 98% of the radius with a value of 0.41 m. The distance between the rotation axis and the tip is 8.17 m. The blade has a linear twist angle of 8 degrees and a solidity of 0.0325. The wing has also a tip cap shown in Fig.38:
The blade has also the possibility to improve the chordwise and spanwise balance with adjustable tip weights used for high pitch settings.
The distance from the ground is 12.8 m so the ground effect will be analyzed and compared with result that neglect this increase of the thrust.
Carpenter made several different tests by changing the rotational speed and the blade pitch angle. The estimated accuracies of the basic quantities measured from Carpenter are around 200 N for the forces, 0.2 degrees for the angles and 1 rpm for the rotational speed. The following table summarizes the features of the rotor:

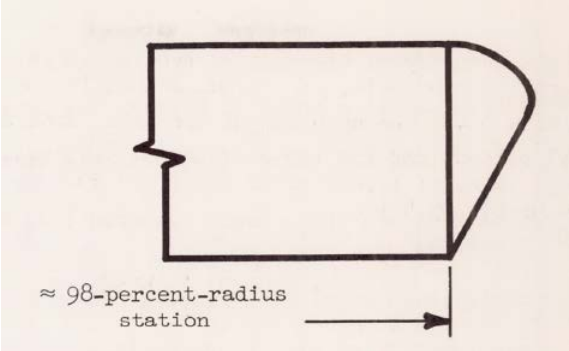

Figure 38: Tip cap of the Carpenter blade[8]

The results between the FT-Freewake code and the test data available concern mon-

Table 1: Carpenter rotor features

Radius	8.17 [m]
Number of blades	2
Root Radius	1.23 [m]
Chord	0.41 [m]
Ground distance	12.8 [m]
Area	209.7 $[m^2]$
Linear twist	8 [deg]
Tip cap	yes
Wing profile	NACA 0012
Tip Mach	0.22-0.7
Pitch angle	0-20 [deg]

stly the total thrust and the required torque or power and their coefficients.

Fig.39 shows the trend of the thrust coefficient at different pitch angles, the plots are made by interpolating bench test results. It is also possible to note the analytic result calculated with the incompressible theory in the linear lift coefficient against angle of attack area.
Fig.40 summarizes the thrust vs the torque coefficients:
Especially for high thrust and torque coefficients the lines diverge from the incompressible no-stall theory.
Obviously the rotor is in a perfect hover condition so the V_x and the V_z velocities are both zero. The test boundary conditions as the temperature or the density of the air are not specified by Carpenter so the case is analyzed at sea level, ISA. Another inaccuracy point is the elasticity of the blade which has not been specified[8].

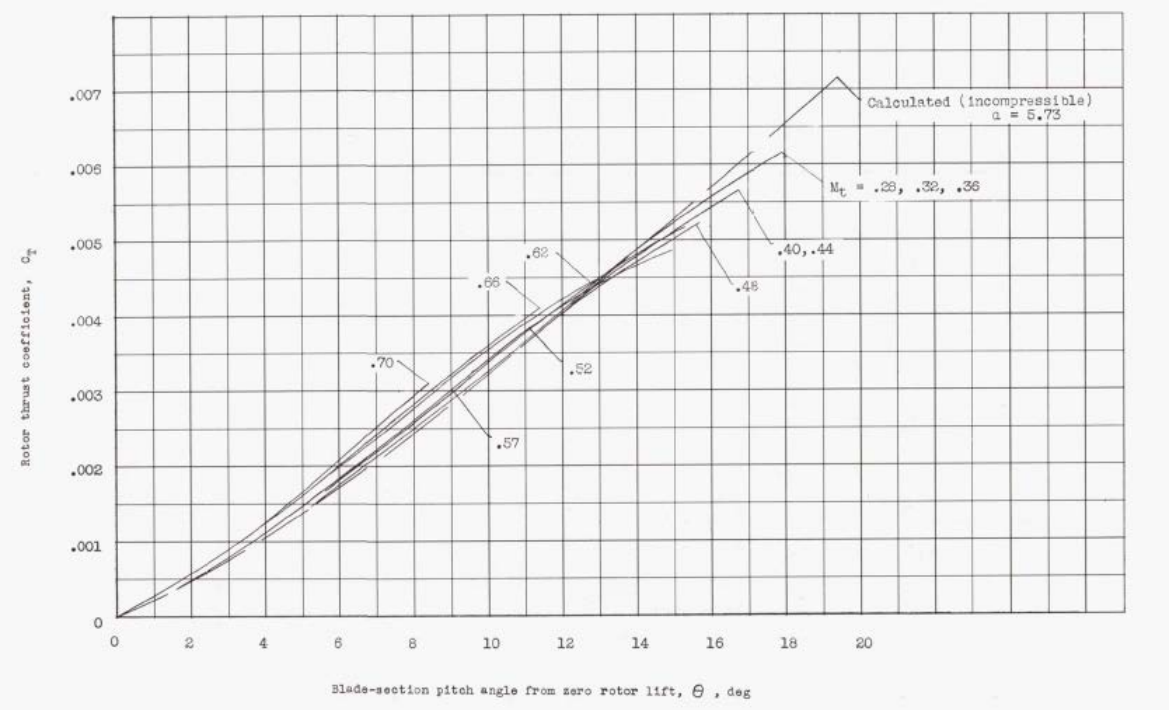

Figure 39: Thrust coefficient vs pitch angle for Carpenter

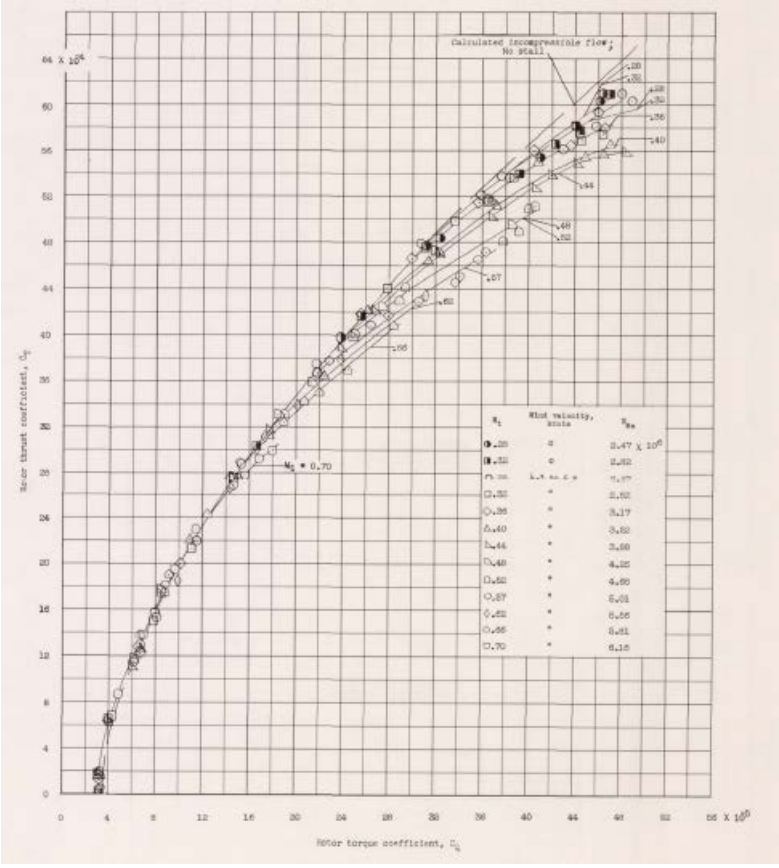

Figure 40: Thrust coefficient vs torque coefficient for Carpenter[8]

4.2 Caradonna-Tung rotor

The rotor consists in two rigid blades with rectangular shape. The wing profile is a NACA 0012 (symmetric) along all the length of the blade which has zero twist.
The model built and tested in the 1981 has a radius of 1.143m and a chord length of 0.1905m which results in an aspect ratio of 6. For increasing the accuracy of the results the rotor was mounted on the top of a tall column containing the drive shaft inside a particular room that reduced the recirculation. The drive shaft permits a constant turning speed of 1250 rpm. The rotor has been operated with a large number of test conditions varying the Mach number at the tip or the collective angle. For this validation the chosen collective angle is equal to 8 degrees.
The validation has been made not only comparing absolute values as the total thrust or the thrust coefficient but also local distributions. In order to obtain physical results for the whole flow field the investigation considered the measurment of the lift coefficient along the radius for whole the rotor disk which confirmed the correct trend of the thrust. This allows to understand which physical phenomena have been considered in the code and which ones are neglectable. This can be also done analyzing the entire shape of the wake which is required to check the correct convergence of the iterations. Fig.41 shows the geometry of the Caradonna test:

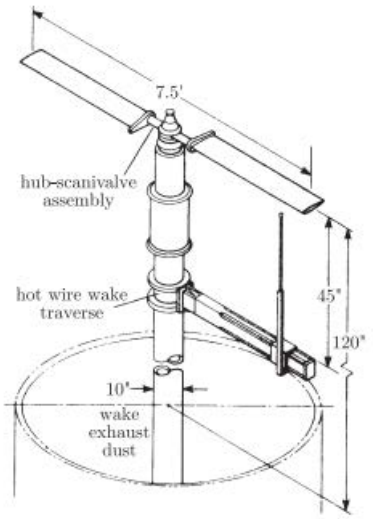

Figure 41: Caradonna-Tung rotor modeling[9]

The characteristics of this model are summarized in table 2. Caradonna was able to find the lift coefficient distribution along the radius of the rotor. In an untrimmed simulation in which the pitch angle is an input, the c_l trend permits to understand whether the induced velocity is correct. Since the twist angle is zero the lift distribution for this rotor increases with the radius due to the rotational velocity, which correspond

Table 2: Caradonna-Tung rotor features

Radius	1.14 [m]
Number of blades	2
Root Radius	0.19 [m]
Chord	0.19 [m]
Ground distance	$> 2R$ [m]
Area	4.08 $[m^2]$
Linear twist	0 [deg]
Blade shape	rectangular
Wing profile	NACA 0012
Ω	1250 [rpm]
Pitch angle	8 [deg]

to a large error of the uniform inflow of the momentum theory.
Fig.42 highlights the bench test results assuming no variation along the azimuth. This phenomenon is true just in hover case. The maximum peak of the lift coefficient occurs at the 90% of the radius and the thrust coefficient is equal to 0.0046. From $T = c_T \rho A(\Omega R)^2$ it is possible to find the total thrust for this rotor which is 515 N.

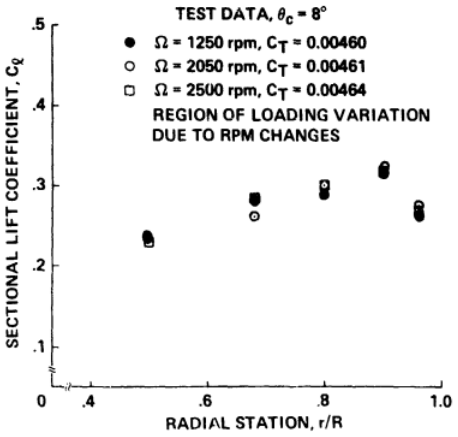

Figure 42: Caradonna-Tung lift coefficient distribution[9]

Fig42 also highlights how the thrust coefficient distribution is almost not affected by an increase of the rotational velocity. The variation on the average is negligible and the only point that does not perfectly fit the others is at 0.7 of the radius.
Although it is not clear from the examination of the test data, the lift coefficient must decrease until zero at the tip of the blade[9].

4.3 H135 rotor

In this chapter, the rotor of the H135 is summerized. This is a four blade rotor with a radius of $5.2m$ and a constant chord along the span with exception of the blade tip which is parabolic. The rotor has 3 different airfoils depending on the radial position, the first airfoil starts at the 30% of the radius. The twist of this rotor has been studied in order to achieve an almost uniform thrust distribution along the radius in the most common flight conditions. The helicopter permits to slightly modify the angular velocity of the rotor depending on the speed and the altitude.
The rotor has not been simulated alone as done for the validation cases; the model for the entire helicopter has been used in Gensim but just the main rotor has been passed to the freewake. The model has been evaluated in a trim condition, which means that the angles were not prescribed but iterated by Gensim in order to converge to the correct thrust[10].

Table 3: H135 rotor features

Radius	5.2 [m]
Number of blades	4
Root Radius	30% R
Area	84.9 [m^2]
Blade shape	rectangular with parabolic tip
Ω	variable ca 41 [rad/s]
Pitch angle	trimed to desired thrust

5 Implementations

In order to increase the performance of the code, increase the accuracy or simply solve errors, two main implementations will be summarized in this chapter. Since the FT-Freewake and its coupling with Gensim are first version codes, some minor errors and bugs have been found and solved before achieving the results that will be presented. The first implementation aims to reduce the possibilities of diverging of the simulation; the divergence might occur when the difference with the momentum theory is large or when, for numerical reasons, the solution keeps bouncing from a value to another without a real convergence.
The second implementation is a real correction of the FT-Freewake code by fixing a missing part in the lattice method of the wake that leads to a missing induced velocity component.

5.1 Relaxation factor

A solution that various codes utilize to stabilize the convergence of the iterations is the relaxation factor (RF). This mathematical method aims to reduce the variation between an iteration and the previous one. In this case the relaxation factor acts directly on the induced velocity as:

$$v_{i_n} = (1 - RF)v_{i_n} + RF(v_{i_{n-1}}) \tag{5.1.1}$$

where n is the iteration number. For a proper use the RF must be a floating point number between 0 and 1, where 0 means that the new induced velocity is not affected at all by the previous one and 1 means that the induced velocity does not vary along the iterations. In this case setting the relaxation factor to one compromises the correction of the free wake along the iterations since the inflow will always be the one provided by the first Free-wake iteration. Setting the RF to 0.5 means doing an average between the two induced velocities.
Fig.43 shows the behaviour of the relaxation factor on the global thrust for the Caradonna rotor. The implementation affects the local distribution in the same way. The graph also shows that for this test a relaxation factor equal to zero would mean a not converged solution. A relaxation factor of one is also not correct because it converges to the wrong value, since the induced velocity is not adapted. Common values for this parameter are from 0.1 to 0.5. In this graph the trend shows how this implementation reduces the number of iterations needed; this phenomenon is true just with this type of convergence in which the third value is always in the middle of the previous two.

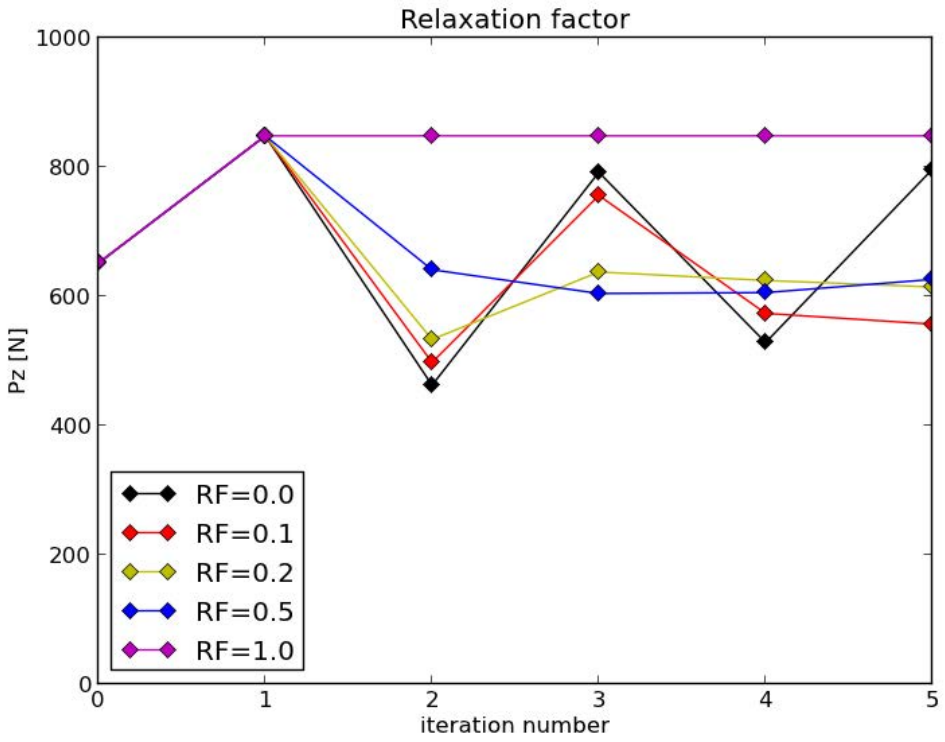

Figure 43: Effect of the relaxation factor

For an asymptotic convergence in which the solution goes always in the same direction the relaxation factor slows down the computation and more iterations are required.

5.2 Missing vortex lines

An important rule for the lattice method is that the grid must be closed; since the bound vortex position is placed at $c/4$ the first trailing vorticity must start in the same position with a normal direction until the trailing edge. Analyzing the trend of the lift coefficient it was possible to notice that the free wake code could not evaluate the tip losses. A too high lift coefficient at the tip means that in that area the induced velocity is too low: this behaviour is not correct since using this theory at the tip there should be a strong vortex producing in the closer evaluation point a strong downwash. Fig.44 shows the wrong distribution of the lift coefficient after the first free wake iteration. The comparison between the lift coefficient produced by the vortex method and the momentum theory method will be studied with a higher accuracy in chapter 6, however this graph aims to make the reader aware of the error in the code that produces a non-zero lift situation at the tip. On this plot the Caradonna case is proposed because the almost linear increase of the angle of attack, and consequently the lift coefficient,

highlights better the phenomenon. However, it is possible to notice this error even in forward flight with a non rectangular blade. The task of this correction is not to achieve the perfect zero condition at the tip but to change the trend in that direction. Because of the highly three dimensional behaviour achieving zero lift at the real tip of the blade is very difficult with a code that uses the blade element theory.

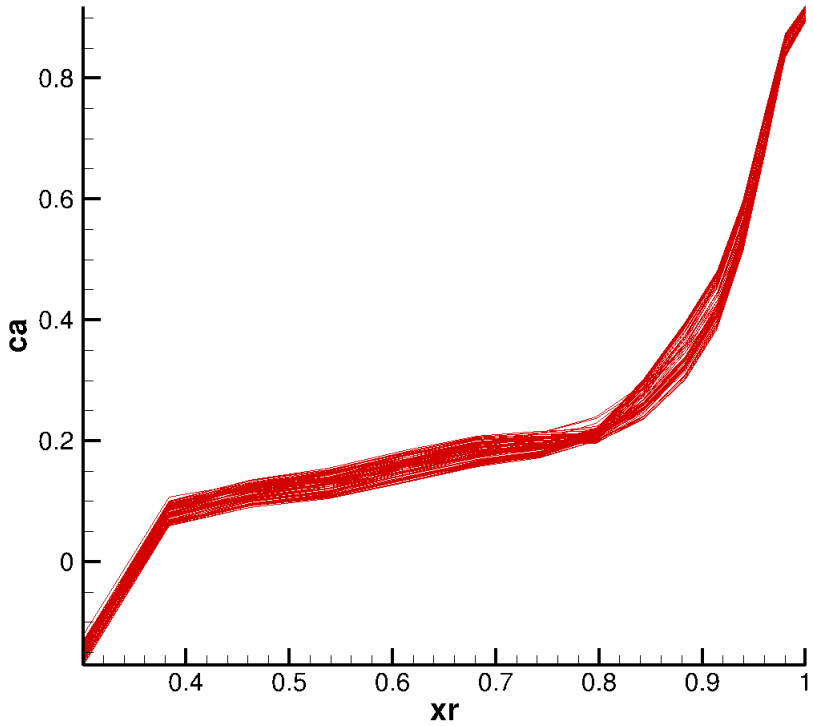

Figure 44: Distribution of the lift coefficient before implementation of the missing vortex lines

According to DLR it is clear that the missing vortex lines are needed to improve the results and to permit the removal of the Gensim tip-loss model. It is important to remember that a missing induced velocity or in general an error in the induced velocity field in a free wake code affects also the shape of the wake and the iteration inside the FT-Freewake code itself.
Fig.45 shows the trailed vortex lines that have been implemented, the blue lines were missing in the original FT-Freewake code.
The implementation consists in summing the induced velocity produced by the missing lines into the inflow that FT-Freewake outputs back to Gensim, obviously the limitation of this implementation is that the shape of the wake is not affected by it, so the result will not be highly accurate. For a better implementation the correction of the FT-Freewake main code by DLR is required. The correction uses the Biot Savart law explained in chapter 2.4 to evaluate the velocity induced by a finite length vortex segment in an evaluation point. To maintain the uniformity with FT-Freewake, the

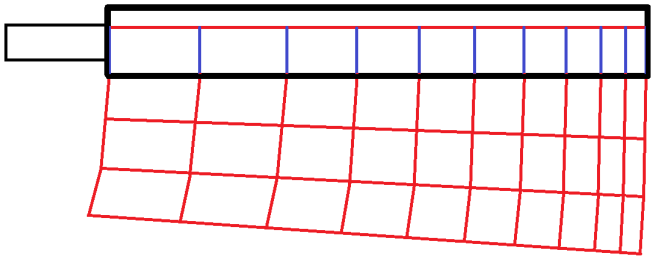

Figure 45: Missing vortex lines

points are placed radially in between two consecutive vortex lines using the "area rule" in which the disk is divided in rings of equal area in order to get a higher definition at the tip. The implementation permits to move the point vertically from the $c/4$ line to the trailing edge according to the version of FT-Freewake that the user adopts. Every point is affected not just by the circulation of the two near vortices but the induced velocity must be evaluated in every point for every vortex.
The strength of a trailing vortex is defined as the difference in bound vorticity along the radius so the trailed circulation can be defined depending on the radial position as:

$$\Gamma_{t_1} = \Gamma_{b_1} \tag{5.2.1}$$

$$\Gamma_{t_k} = \Gamma_{b_{k+1}} - \Gamma_{b_k} \tag{5.2.2}$$

$$\Gamma_{t_n} = -\Gamma_{b_n} \tag{5.2.3}$$

where 1 is the vortex at the root radius, n is the tip vortex and k are the generic vortices in the middle of the blade.
For the Caradonna case, for which Gensim provides an almost linear lift coefficient distribution without any reduction at the tip, the bound circulation and the trailed circulation at the first iteration have the following trends (Fig.46):

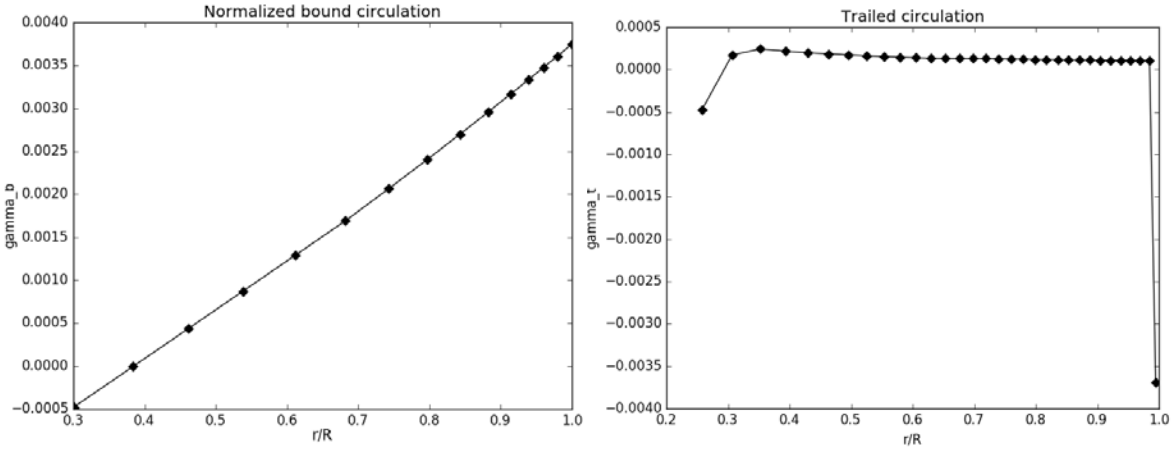

(a) Bound circulation (b) Trailed circulation

Figure 46: Bound and trailed circulation after for the first free-wake iteration

From the plot in Fig.46 of the trailed vorticity it is clear that the main correction will affect the area at the tip and at the root of the blade. As previously introduced, the evaluation point at the tip will be more affected by the correction not only due to the higher strength of the vortex but also for their distance from it. Due to the linearity of the lift coefficient provided by the Gensim inflow model, the strength of the trailed vortices in the middle of the blade is constant along radius.

Fig.47 shows the behaviour of the correction on the induced velocity by plotting the inflow along the radius before the correction, after the correction and the correction it-self.

As expected the figure shows that the correction does not affect at the radial positions of the blade far from the root or the tip. The correction at the root is negligible in the global integration for the thrust since the local speed is very low. The graph shows how the behaviour at the tip is completely wrong: for the Caradonna case according to the blade element theory at the tip the induced velocity must increase up to 18 m/s which is not a neglectable modification.

Since it is not possible to increase the radial discretization in Gensim, this aspect decreases the accuracy and does not permit a smoother solution which is more physical.

A very interesting phenomenon that the graph permits to understand is the position along radius of the lift peak. In the presented case it occurs where the correction line (black) and the induced velocity without correction line (lilla) cross each other near by 0.95 of the normalized radius. The strong downwash that happens at the tip of the blade is mainly due to the high negative strength of the tip vortex and the positive one of the previous vortex.

The vortex at the tip induces a downwash velocity all over the blade that decreases

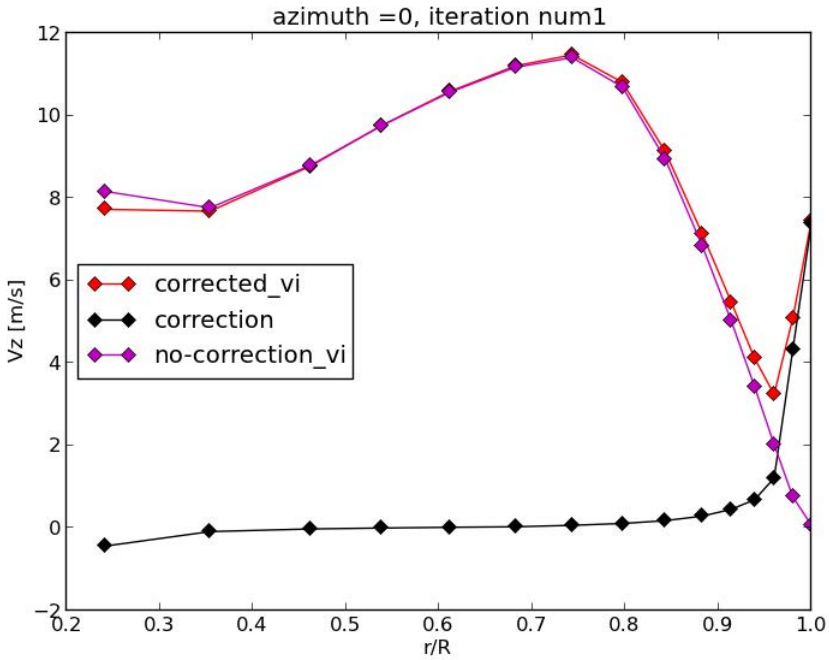

Figure 47: Trend of the induced velocity due to the implementation of the missing vortex lines

with the distance from it.
Fig.48 analyzes the trend of the lift coefficient to prove that the implementation behaves correctly.

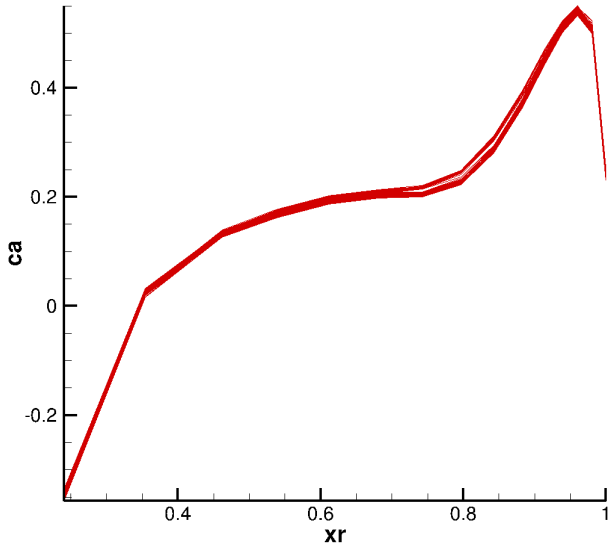

Figure 48: Distribution of the lift coefficient after the implementation

As expected, at 95 % of the radius the lift coefficient starts decreasing rapidly due to the tip-losses. The thickness of the line represents the variation along the azimuth of the lift coefficient which for a hover case is clearly small.

The distribution of the lift coefficient proves that the implementation works correctly; in order to allow the user to increase the inflow due to the correction at the tip and raise the accuracy, a strategy already implemented in Camrad [19] has been adopted: an input scalar defined as moving parameter permits to shift horizontally the position of the tip vortex. The moving parameter must be set to 1 if the user wants to leave the tip vortex at the real tip of the blade instead, if, the moving parameter is set to zero, the vortex will be in the same position of the last evaluating point, this will produce a singularity in the Biot Savart law and the induced velocity will explode. Another solution would be the one used by free-wake, that is the vortex core radius, but for this implementation where the position of all the vortex lines is fixed except made for the tip vortex a real vortex core radius is not required.
Another correction to the implementation must be made to obtain a physical result: after the first iteration the lift distribution will not increase along radius but near the tip the coefficient will start to rapidly decrease; the bound circulation has a trend similar to the lift coefficient and after the first iteration is (Fig.49):

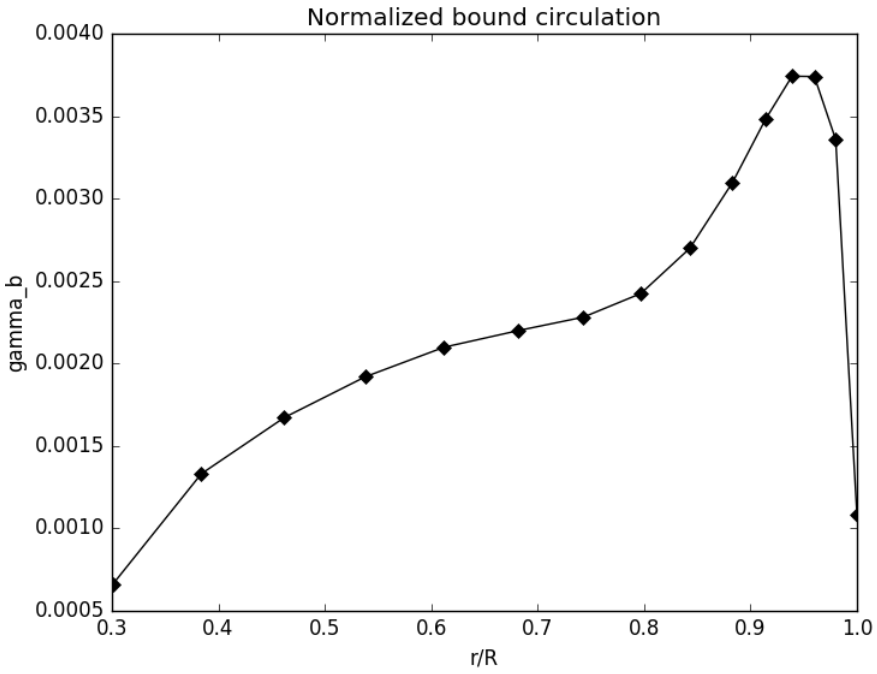

Figure 49: Bound circulation after first iteration

This trend produces a really weak vortex at the tip and a strongly negative trailed vortex in the point before the tip which would lead to a strong upwash. Clearly this phenomenon is not physical and it would diverge along the iterations. To solve the problem, an integral average in the bound circulation has been introduced for all the points after the lift coefficient peak, in order to avoid a zero strength vortex at the tip and a strong negative vortex before. For the trailed vorticity this leads to have a

number of vortices with zero strength between the tip and the peak of the lift coefficient. The trend of the trailed vorticity after these corrections becomes as shown in Fig.50:

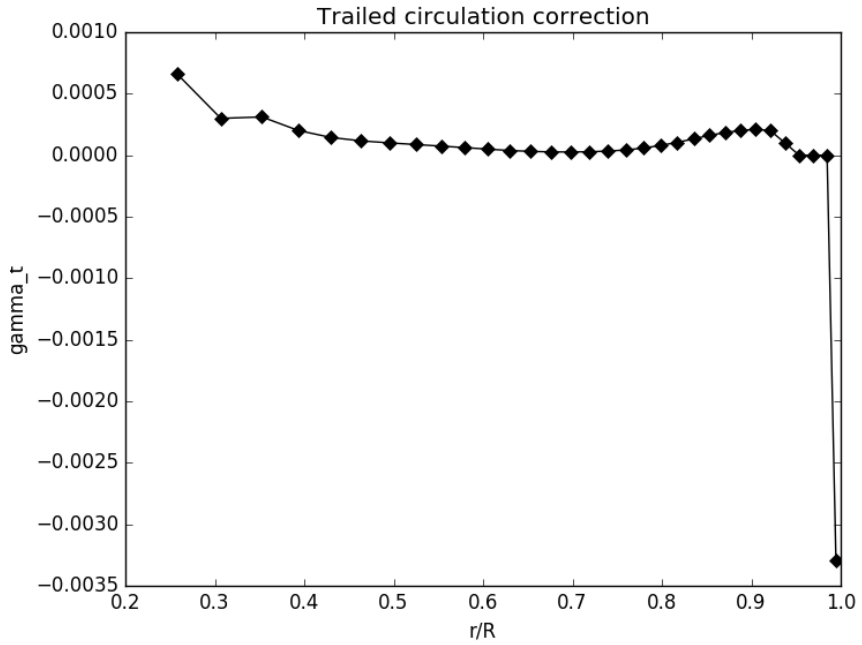

Figure 50: Trailed circulation after first iteration

In Fig.50 it is possible to note the number of evaluating points in the descending side of the lift coefficient.
The correction modifies the induced velocity that Gensim uses along the three axis. The implementation first calculates the induced velocity on the evaluating points and then evaluates the components along the axis by taking into account the angle of attack of the blade in that section, the cone angle of the blades and the not fixed frame of the blades. The corrected induced velocities along the three axis are:

$$V_x = V sin\alpha(V_x cos\psi - V_y sin\psi) \tag{5.2.4}$$

$$V_y = V sin\beta(V_x sin\psi + V_y cos\psi) \tag{5.2.5}$$

$$V_z = V cos\alpha cos\beta \tag{5.2.6}$$

where α is the angle of attack, β is the flapping angle and ψ is the azimuth.
As previously mentioned this is only a coarse correction since the shape of the wake is not affected. The inaccuracy increases in hover condition where the wake stays longer under the rotor, whereas for forward flight conditions the behavior is less pronauced. The missing modification of the shape of the wake will lead in more BVI since the tip vortex will not move down due to a high induced velocity.

6 Results

In this section the results obtained with the coupling between Gensim and FT-Freewake for the three different rotors will be presented, summarizing also the input parameters. The accuracy and the weaknesses of the code will be highlighted and explained in order to understand properly the operative range of the code, comparing the accuracy of the BEMT and the vortex theory. The global and the local trend will be compared against bench and flight test data, highlighting the improvement of the result. The computational time will also be analyzed in order to understand which parameters mostly influence it.

6.1 Results for the Carpenter rotor

To maintain the uniformity with the rest of the document the first results presented are those concerning the Carpenter rotor.
Three main tests have been carried out on this rotor, changing the Mach number and the pitch angle at the 70% of the radius. The global comparison regards the thrust coefficient against the pitch and the thrust coefficient against the power coefficient.
In the first part of this chapter one of the three tests will be analyzed with more details and after that, the global trend will be presented, starting from the input parameters, which have not been modified between one test and the others. The number

Table 4: Carpenter input parameters

Number of iterations	9
Relaxation factor	0.2
Moving point	1.0
VCR	8% of the radius
Wake revolutions	15
Max turns	18
Radial discretization	32
Azimuthal discretization	72
Test 1	$M_{tip} = 0.7$ $\theta_{70} = 6$
Test 2	$M_{tip} = 0.6$ $\theta_{70} = 13$
Test 3	$M_{tip} = 0.3$ $\theta_{70} = 18$

of iterations between Gensim and FT-Freewake and the relaxation factor affect the convergence of the coupling; these two parameters are larger for the validation tests in order to understand better the causes of divergence, if occurs. The relatively high number of wake revolution and Maximum number are used to achieve a long wake and are required since in a hover case the wake does not move apart from the rotor but stays under it. A large VCR is needed to analyze properly the wake far from the

rotor disk, stabilizing the wake shape and the solution. The moving point has not been chosen in order to obtain zero lift at the tip but just to confirm the trend.
The test chosen is the number 2 and the result for the thrust coefficient is 0.00443. Fig.51 shows the C_T variation along the iterations in order to understand the convergence of the solution and compares the result with the bench data provided by Carpenter.

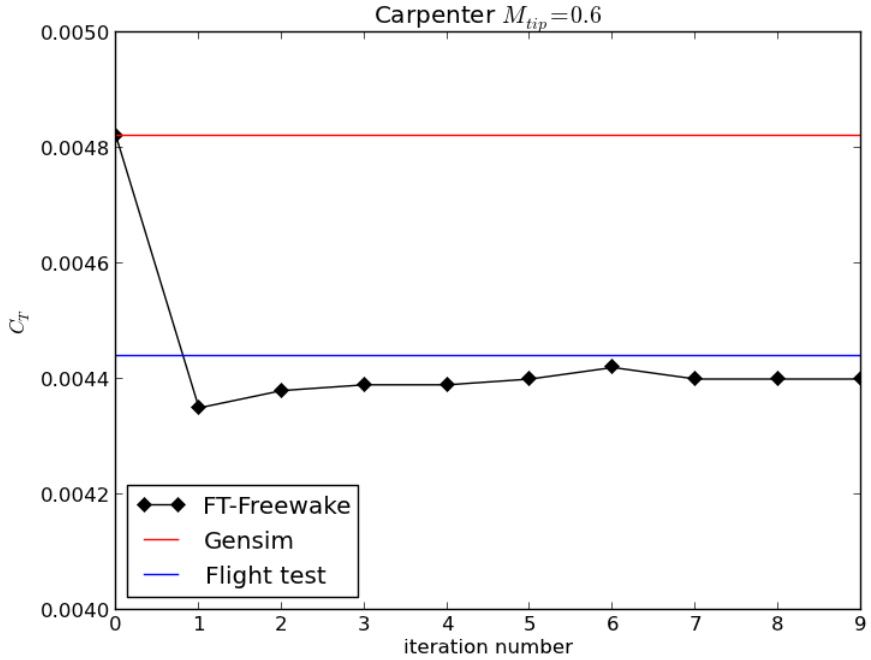

Figure 51: Thrust coefficient for Carpenter Test 2

From the graph the stability of the code is clear, just three iterations and, in this case, the result is already at convergence. The iteration number zero represents the BEMT result, which, has an accuracy of ca. 9 %. The result obtained with the free wake has a global error of 0.6% which is totally negligible since it is lower than the accuracy of the bench test.
The damping factor of the convergence of this solution is very close to 1 since the thrust coefficient has a negative peak at the first iteration and then it never increases more than the final iteration except for the iteration number six in which a mathematical approximation occurs.
Now that the global result has been confirmed, the local distribution of the induced velocity, the angle of attack and the lift coefficient are analyzed. Fig.52 permits to understand properly the deviation between the BEMT and the vortex theory which results higher than expectated. Two different types of graphs will be presented: a 2D normal graph that shows the trend of the magnitudes along radius for the zero azimuth due to its simplicity and accuracy, and a 2D polar contour graph that shows the trend

over azimuth and radius to prove the homogeneity of the results for this hover case. Unfortunately the tests made by Carpenter do not provide a local distribution of aerodynamic forces. Fig.52 shows the main aim of this work which is the study of the local distribution of the induced velocity.

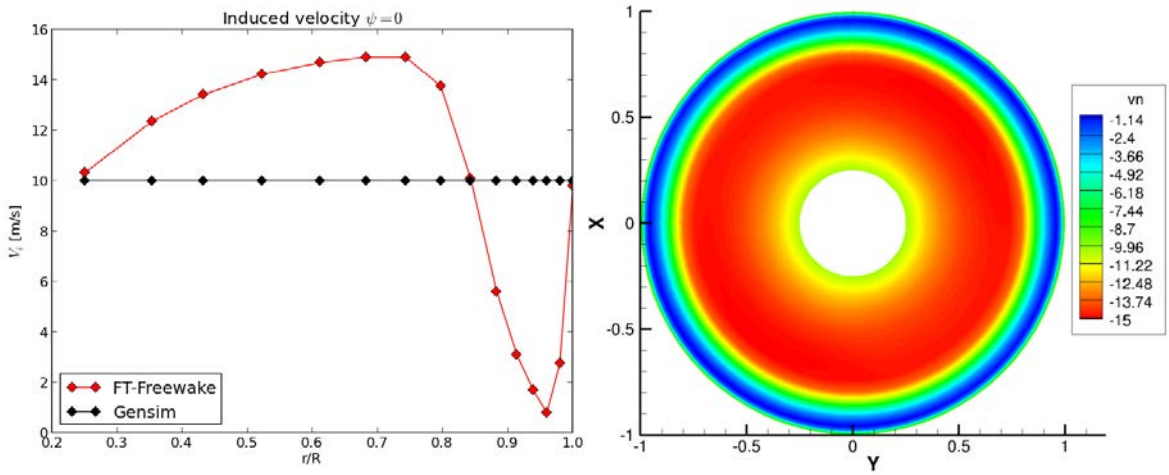

(a) Carpenter Test 2 induced velocity (b) Carpenter Test 2 induced velocity contour

Figure 52: Carpenter induced velocity test 2 iteration 9

The induced velocity proposed in the graphs belongs to the last iteration; the variation along the iterations is not presented in this case since the difference is not visible.
The difference between Gensim stand alone and Gensim coupled with the freewake is clear from the graph on the left side; Gensim calculates a 10 m/s of uniform inflow that is almost correct in the average value but not in the local distribution. The trend shows that in the inner part of the blade the freewake induced velocity is higher than the Gensim one which involves a lower angle of attack in that area. At a normalized radius of 0.7 it rapidly decreases from 15 m/s to almost zero at 95% of the radius. This decrese in the inflow produces a strong increase in the angle of attack. From 95%R to the tip the induced velocity increases with a high gradient due to the missing line implementation that aims to reduce the lift coefficient at the tip.
The graph on the right side highlights the uniformity along the azimuth, that suffers small variations caused mainly by the velocity induced by the instable far wake. Using the Python function that integrates by means of the Cavalieri-Simpson method and integrating along radius and azimuth the global value for the induced velocity is 9.67m/s.
The strong variation in the gradient of the inflow at 95% of the radius is an inaccuracy due to the coarse mesh that Gensim allowes along the radius. Due to its homogeneity, it is difficult to understand the axis direction of the contour plot: the zero azimuth is the line that from the center of the disk goes to Y equal to zero. For the graph on the

left a positive sign means a downwash and vice versa for the graph on the right.
To understand if the correction of the inflow is physical, it is important to analyze the trend of the vorticity on the rotor disk. The decrease of the induced velocity that occurs at 80% of the radius must be provided by a decrease of the strength of the vortices in that area. Fig.53 shows the distribution of the vorticity in the upper part of the wake; to increase the zoom the wake below 150% of the radius has been blanked. The trailing vorticity has been normalized in this plot; to simplify the understanding of the graph the upper value of the vorticity in the axis does not represent the real maximum value in order to permit a better visualization of the distribution in the middle part of the rotor disk.

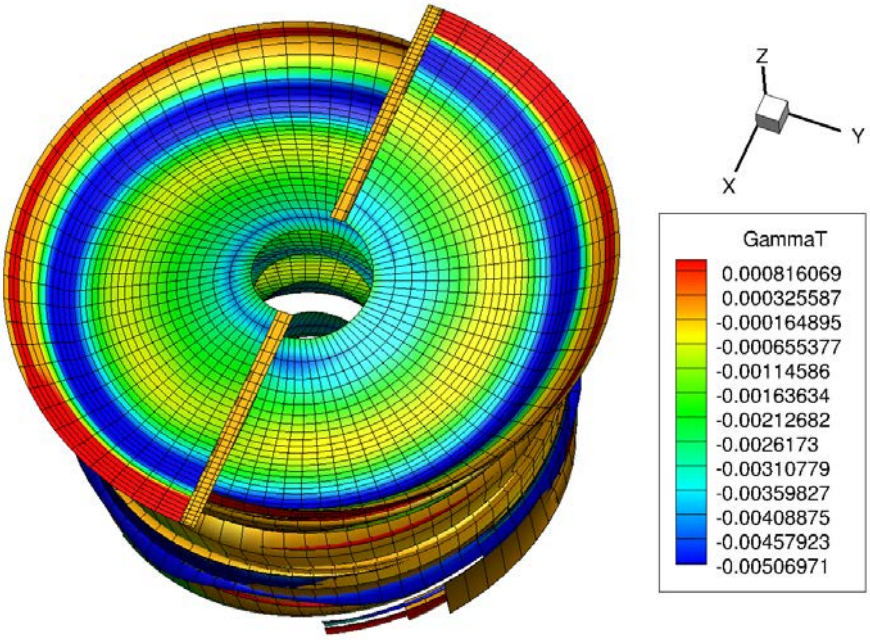

Figure 53: Trailing vorticity distribution for Carpenter rotor

As expected the plot shows that around 80% of the radius there is a strong decrease in the trailing vorticity, this effect is caused by the interaction with the wake of the other blade. This also permits to highlight the contraction that the wake experiences especially after the fist half revolution which of course has the main effect on the rotor disk.
The plot also shows the missing vorticity on the two blades that has been added in the coupling script in order to connect the lifting line to the rest of the lattice panels. The thickness of the blue zone explains exactly the contraction of the wake with the increase of the velocity along the z direction. It is very interesting to note that the radius of the wake section after the first revolution is subjected by the highest decrease due to the higher positive gradient in the velocity. The vorticity in the outer part of

the wake results to be 50 to 100 times higher that the plotted one, resulting in a strong downwash velocity that moves the entire wake downwards and denies the interaction between the blade and wake caused by the other blade for a hover case.
Now that the induced velocity distribution is explained, it is important to understand how the angle of attack reacts to this variation. As done for the induced velocity the result will be compared with the stand alone Gensim BEMT and analyzed on the rotor disk.

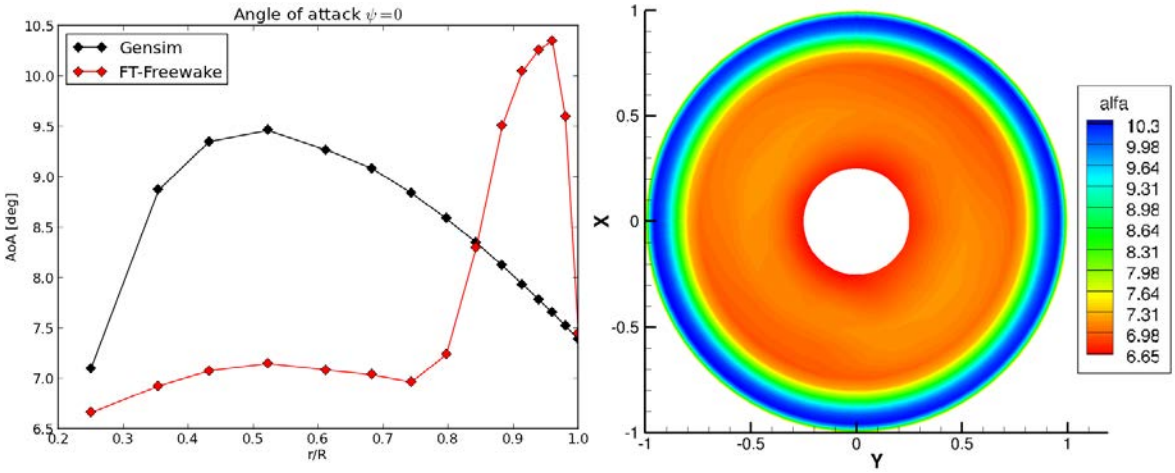

(a) Carpenter Test 2 angle of attack

(b) Carpenter Test 2 angle of attack contour

Figure 54: Carpenter angle of attack test 2 iteration 9

Fig.54 confirms that the induced velocity provided to Gensim by the Free-wake is applied correctly because when BEMT is applied to a rotor with a fix collective pitch angle, a higher induced velocity corresponds to a lower angle of attack. Unfortunately the graph also shows that the reduction in the angle due to the implementation of the missing vortex lines requires a higher number of discretization points along the radius to achieve a smoother distribution which is more physical.
The vortex theory produced a distribution of the AoA almost constant between 6.7 and 7.2 degrees until the 80% of the radius with a maximum difference with the BEMT of 2.5 degrees around 50% of the radius. After that a quick increase rises the angle of attack up to 10.35 degrees at around 95% of the radius that can be considered as the position where the tiplosses start. The angle of attack does not decrease enough at the tip of the blade and this will produce a non zero lift situation, since the evaluation point at the tip is placed at 99.5% of the radius and the gradient is strongly negative the global result has been considered as correct.
Fig.54 also confirms the uniformity along azimuth typical for a hover case.
Fig.55 show the trend of the lift coefficient to let the reader understand the distribution

of the thrust along the blade radius.

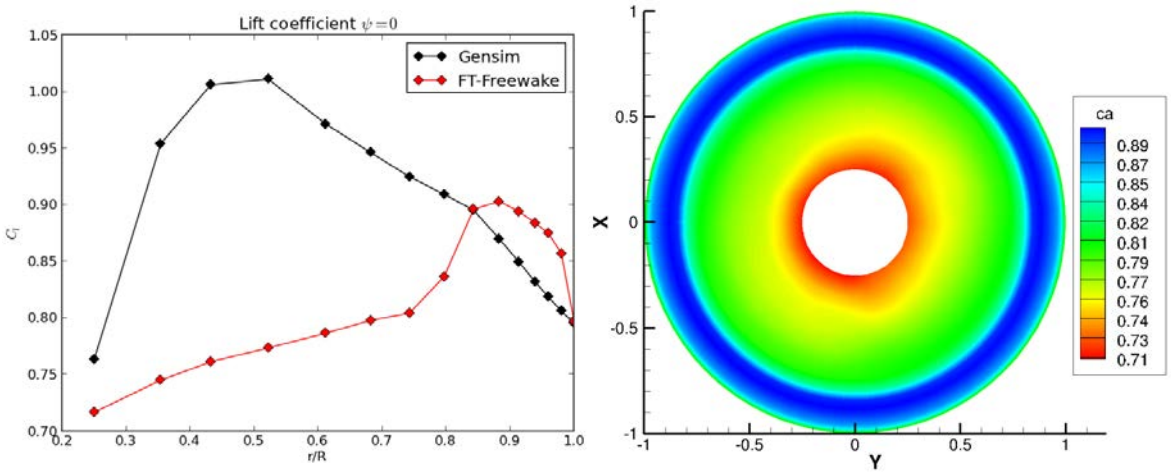

(a) Carpenter Test 2 lift coefficient

(b) Carpenter Test 2 lift coefficient contour

Figure 55: Carpenter lift coefficient test 2 iteration 9

The angle of attack distribution is confirmed along the radius, altough some discrepancies occur near the tip probably due to an inaccuracy of the lift coefficient polars. The graph shows that the blade is affected by a strong thrust in the outer part since the lift coefficient must be multiplied by the square of the tangential velocity and by the chord. The linear decrease of the chord at the tip helps the freewake code to decrease the thrust producing also a weaker tip vortex.

A significant difference between the BEMT and the vortex theory is visible on the lift coefficient graph in which the BEMT achieves a globally higher result along the radius except for the outer part in which of course the tangential velocity is higher and this explains the low difference between the two methods.

Finally the plot of the entire shape of the wake will be shown and discussed. The code produces really stable results for the first 4 or 5 revolution then slowly starts diverging until 9 or 10, and between 10 and the maximum number of revolution set it is completely unstable (red zone). This instability should not be seen as an error since this effect occurs even in reality where far downwards the wake of the helicopter loses its tube shape and "explodes". This instability is caused by the loss in accuracy of the position of the vortices after a few revolutions by the free-wake code. The small variations along the azimuth presented in Fig.54,52 are probably caused also by the far unstable vortices; this effect highlights the importance of increasing the number of revolution that the wake must evaluate in hover in which a freestream velocity that transports far away the wake does not occur. Obviously an increase of the revolutions in the wake evaluation strongly affects the computational time.

Another effect that is very well highlighted in Fig.56 is the contraction of the wake

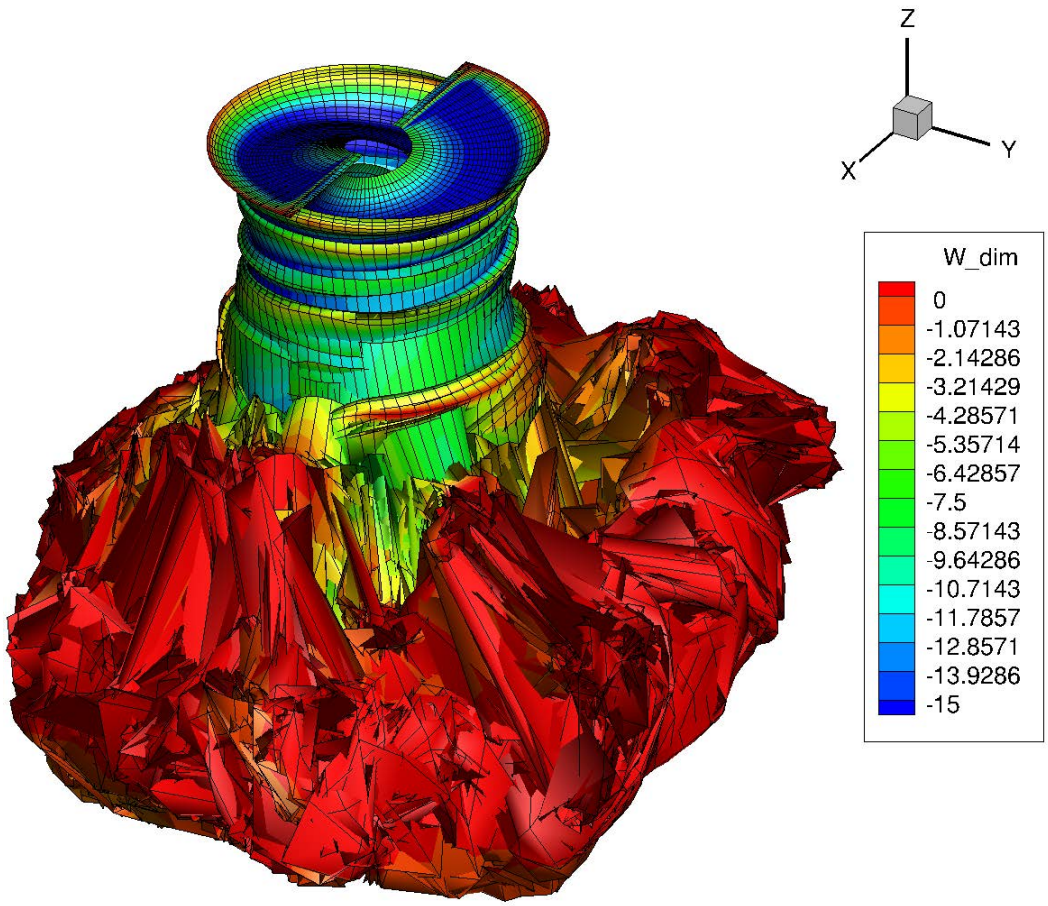

Figure 56: Wake of the Carpenter rotor

(until the instability); the radius of the wake after the stable revolutions is around 75% of the rotor radius.

On the rotor disk plane it is very clear how the wake follows its induced velocity: the blue part that represents a strong downwash moves downwards faster then the green part in which the induced velocity is lower. This effect explains the general correct behaviour of the freewake code.

Probably due to a too large vortex core radius it is not possible to see the roll-up effect that occurs at the tip in which, after the blade, the vortices should move from the inner part to the outer part and create a strong vortex placed near by the tip producing a roll up in the shape of the wake. The code evaluates this effect but due to a too large vortex core radius the shape of the wake at the tip does not roll up enough. To understand better this effect the plot that shows the trend of the tip vortex vorticity is presented in Fig.57. The strength of the vortex at the tip linearly increses for around 40 deg azimuth, this means that after that azimuthal distance all the trailing vorticity of the blade is summed up on the tip vortex except made for the one joining the root vortex which has a smaller vorticity and impact on the induced velocity. The thickness

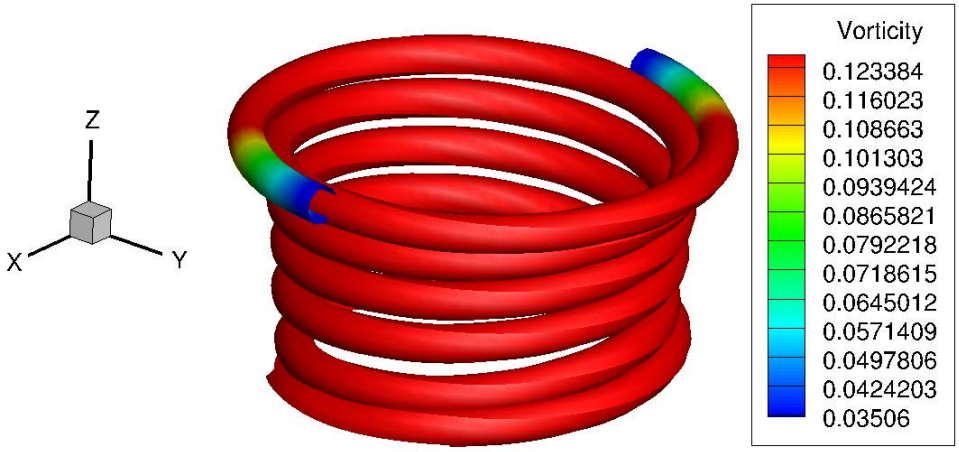

Figure 57: Carpenter tip vortex strength

of the two vortices in the graph (one for blade) is equal to the VCR. This graph helps also to understand the stability of the code: since the shape of the vortex is linear, the shape of the wake for the number of revolution considered must be stable.
Now that the test number 2 has been presented, the global results for the other two cases will be summarized in order to understand whether the code works properly in different conditions. The first aspect that will be analyzed is the trend of the thrust coefficient against the pitch angle.Simulation results are compared against the bench test data.

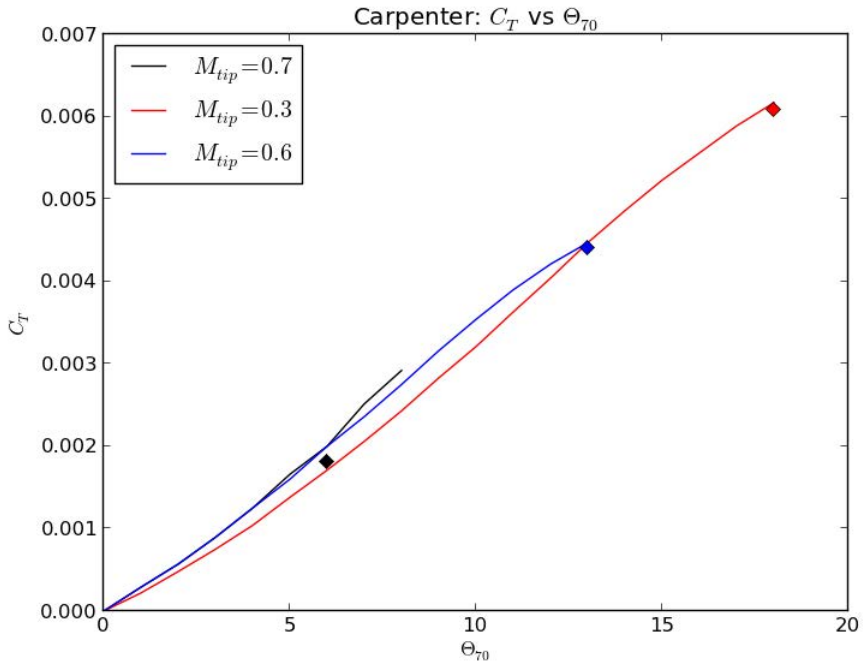

Figure 58: Carpenter: Thrust coefficient vs pitch angle

As for the test with a tip Mach number of 0.6 the case with 0.3 matches perfectly

the polar line. For the test case with a higher Mach number the result produces a lower thrust coefficient compared with the test data. The relative error in that case is around 7.2%. This case is the most difficult for a free wake code to be analyzed since the high rotating speed and the low pitch angle creating a low vertical induced velocity do not allow the wake to move downwards enough. This creates an instability much closer to the rotor disk plane producing unpredictable effects. Probably increasing the number of revolutions, the radial discretization and decreasing consciously the vortex core radius in order to increase the induced velocity would help to obtain a result with higher accuracy but would also increase drastically the computational time which is not the purpose of this method.
Fortunately Carpenter evaluated also the power coefficient which permits to cross-check wether the angle of attack on the rotor disk is correct since it is required with the drag coefficient to calculate the profile power which is added to the induced power to find the C_P. In an untrimmed situation with a prescribed pitch angle this cross-check should not be required since a correct thrust coefficient already proves a global correct induced velocity.

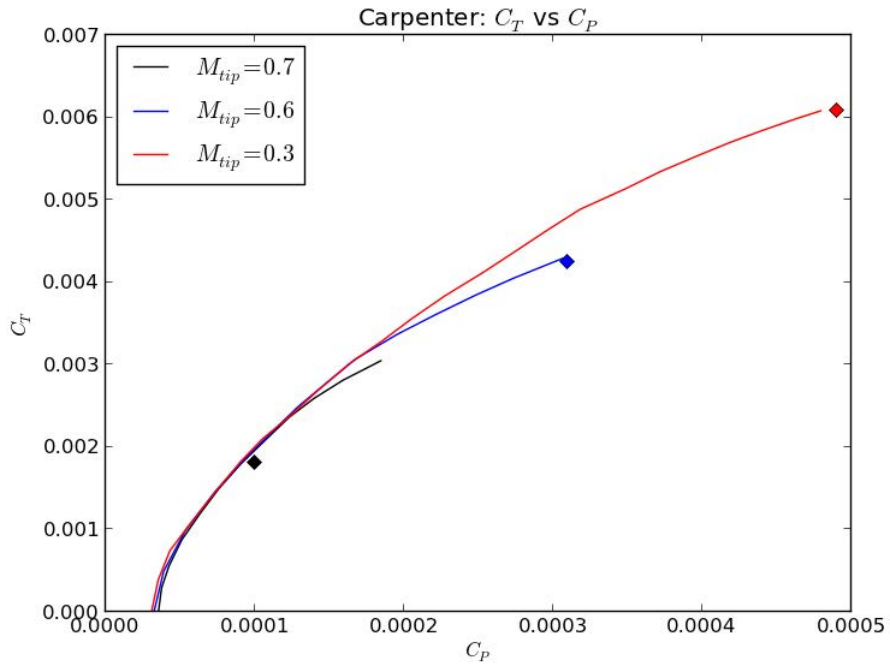

Figure 59: Carpenter: Thrust coefficient vs power coefficient

The general trend is confirmed: in the case with a tip Mach number of 0.3 the resulting power coefficient is higher than aspected. This small offset can be caused by an inaccuracy of the C_d vs angle of attack polars provided in Gensim but is negligible.
All the main results for the three cases are summarized in table 5; only the last iteration is considered because every test reached convergence.

Table 5: Carpenter test results

Magnitude	Test 1	Test 2	Test 3
Omega [rad/s]	29.170	25.00	12.5
Thrust [N]	26090	47104	16270
C_T	0.00181	0.0044	0.00608
$\frac{C_T}{\sigma}$	0.055	0.0135	0.18719
Induced power [kW]	186.0	451.1	91.6
C_P	0.0001	0.00031	0.00049
Average v_i [m/s]	7.127	9.577	5.628
FM	0.5438	0.4412	0.4475
Computational time [s]	145920	56100	51420

The computational time presented in the table explains which cases are easier to evaluate for the freewake code since all the test cases use the same configuration parameters. It also confirms that if the wake moves far from the rotor disk quickly then the evaluation is easier and more accurate. The computational time increase can be explained by the presence of blade vortex interaction that would produce a more fine meshgrid that of course increases the computational effort. The blade vortex interaction is analyzed better in forward flight where this phenomenon is more visible.
For the simulations, 10 CPU's were used, the factor between free-wake and CFD computational time is still above 10, which means that with 100 CPU's a CFD would require the same time, considering the same level of parallelization.

6.2 Results for the Caradonna-Tung rotor

The results for the different tests made for the Caradonna-Tung rotor are presented in this chapter. As previously mentioned the shape of this rotor makes the simulation harder for both codes. To understand the stability, the VCR used for these cases is smaller than the Carpenter one.

Four main tests are proposed: two of them are very similar and the only variation is the vortex core radius dimension. The other two tests consider an effect that can not be neglected which is the elastic twist (the pitch angle increases almost linearly, depending on the shape of the blade, along the radius due to the elasticity of the blade). In the paper that explains the Caradonna-Tung rotor this effect seems to not be taken in consideration, which for a one meter rotor turning at 1250 rpm could be a source of inaccuracy.

To understand this effect a case with 0.5 and one with 1 degrees of linear twist have been added to the normal shape of the blade. Table 6 summarizes the input parameters for the free-wake and the coupling between the two codes. Comparing with the Carpenter, the relaxation factor has been increased, however due to the higher difficulty and the smaller VCR convergence for this case was harder to obtain.

Table 6: Caradonna-Tung input parameters

Magnitudes	Test 1	Test 2	Test 0.5 deg	Test 1 deg
Number of iterations	9	9	9	9
Relaxation factor	0.3	0.5	0.3	0.3
Moving point	0.5	0.5	0.5	0.5
VCR	60%c	30%c	60%c	60%c
Wake revolutions	15	15	15	15
Max turns	18	18	18	18
Radial discretization	32	40	32	32
Azimuthal discretization	72	72	72	72
Θ_0	8	8	8	8
Ω [rpm]	1250	1250	1250	1250

The first case analyzed is the normal rotor with bigger vortex core radius. Fig.60 shows the trend of the thrust coefficient along the iterations, highlighting the improvement but also the offset against the target.

The convergence is not very stable except for the two last iterations. The result obtained with the BEMT is very far from the bench test, around 43 % of error, after the free wake the error decreases to around 14 %. This is clearly a big improvement but the accuracy in this case can not be considered sufficient.

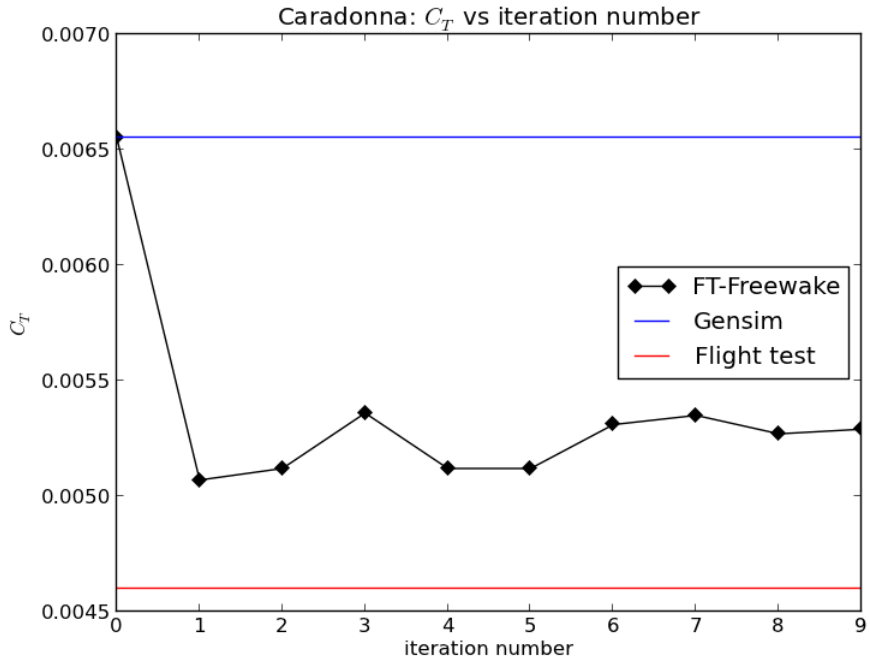

Figure 60: Caradonna Test 1: Thrust coefficient along iterations

This discrepancy is probably caused by several different effects:

- The vortex core radius is still too large and this causes a too low induced velocity
- The implementation of the missing vortex lines does not move the second revolution of the wake far enough and this causes a too low vorticity at the rotor disk
- Inaccuracy of the polars: α vs lift coefficient
- Inaccuracy of the bench test data: elastic twist
- The rectangular untwisted wing requires a higher resolution of the mesh

Due to the erratic convergence along the iterations, the induced velocity plotted in Fig.61 shows its trend for the first iteration, the third and the last one.
Except for the tip, where there is an offset of around 1 m/s, the third iteration and the last are very similar. The first iteration has the same trend of the following one but there is an almost constant offset from the root radius to 70% of R; between 80 % and 95% of the blade span the inflow of the first iteration is lower compared with the last one and the third one.
It is interesting to note that at the tip the induced velocity raises up to 18 m/s that according with the blade element theory will produce a correct lift in that area. This increment is caused by the moving point which has been set to 0.5.

The first iteration produces an induced velocity equal to the Gensim constant value, around 8.5 m/s that is consequently corrected by the following iterations. The minimum value of the induced velocity at convergence is around 6 m/s which produces the peak of the angle of attack in that area.

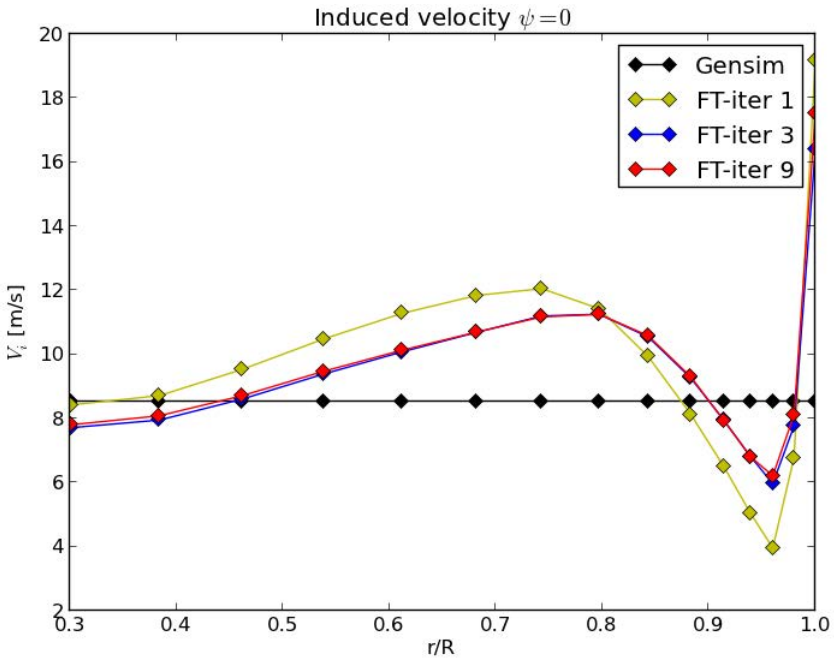

Figure 61: Caradonna Test 1: induced velocity comparison

As done for the Carpenter rotor, after the induced velocity the angle of attack is analyzed in order to understand the correct behaviour even for this case.
The difference in the angle of attack between Gensim and the free-wake is smaller compared with the Carpenter; as expected at the tip the angle of attack is very close to zero (around one degree) and it confirms the correct behaviour of the implementation. Since the angle of attack is small and the velocity is relatively high the lift coefficient should maintain the trend of the angle of attack.
Fig.63 shows the lift coefficient along the radius and its uniformity along the azimuth. The Caradonna experiment evaluated the lift coefficient in five points so the local magnitude is also comparable.
The distribution is not well represented by the free-wake which is lower in the first part of the blade and has a strong increase near the tip (before the tiplosses). Due to the low number of evaluating points used by Caradonna and Tung, it is not possible to understand if there is an increase of lift coefficient in the bench test as well, and it is not possible to see a real tip-loss but just a small decrease. However the peak in the freewake simulation reaches a too high value that causes the offset in the total thrust coefficient; as previously mentioned this peak can be caused by the second revolution

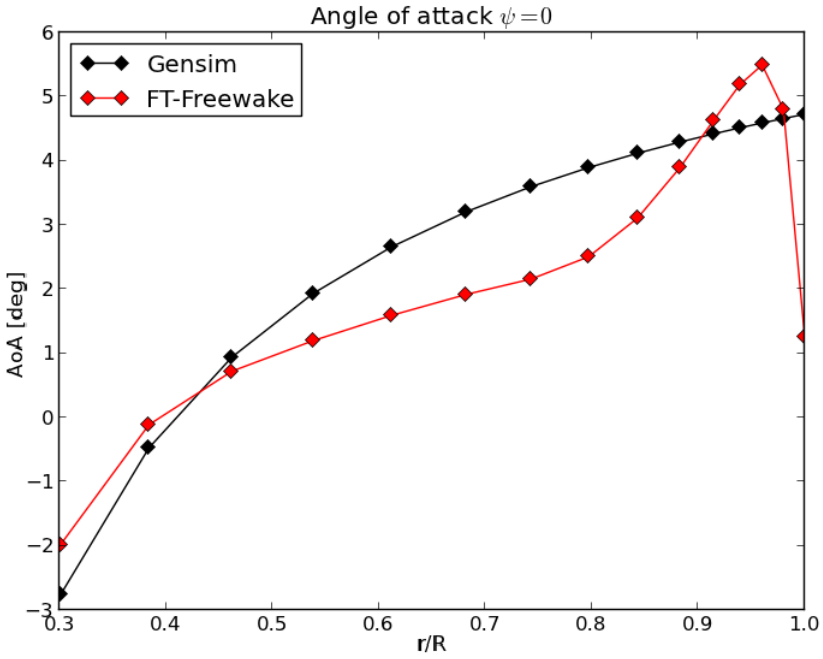

Figure 62: Caradonna Test 1: angle of attack comparison

of the wake that, due to the missing vortex lines, does not move downwards enough. Since the simulation prescribes the pitch angle and does not trim on the thrust, the effect of this error in the inner part of the blade should be negligible. The uniformity

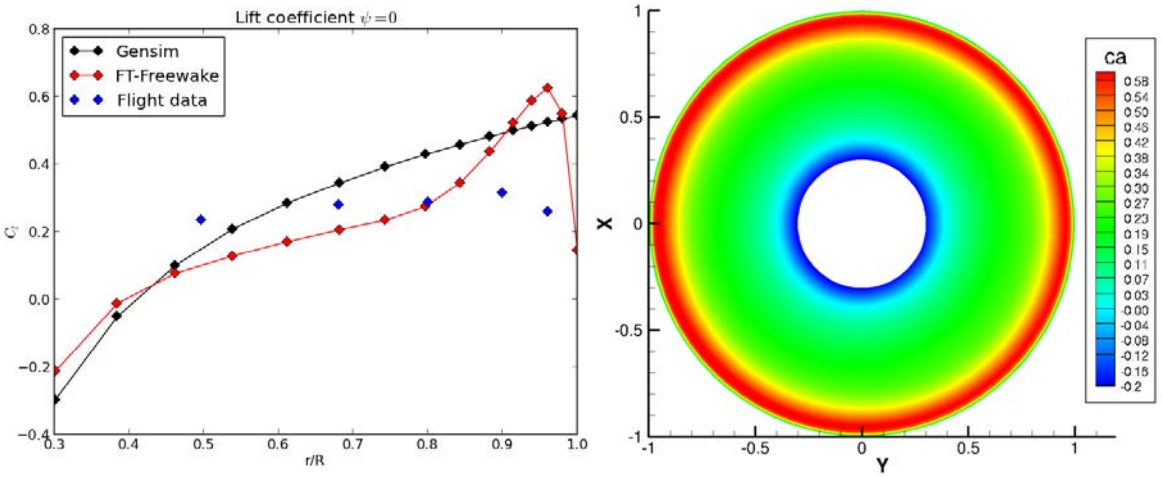

(a) Caradonna Test 1 lift coefficient

(b) Caradonna Test 1 lift coefficient contour

Figure 63: Caradonna lift coefficient test 1 iteration 9

proved by the graph on the right side confirms that the lift coefficient does not change along azimuth. This phenomenon confirms that the shed vorticity works correctly in hover case.

The absence of the peak in the bench data might be caused by neglecting the elastic

twist which will probably decrease the lift coefficient in the inner part but of course the main behaviour will be noticed near the tip. The last phenomenon that is highlighted in Fig.63 is the fact that at the root the magnitude of the lift is negative, which is explained by a high induced velocity.
Before proceeding with the next case, the shape of the entire wake is plotted. Com-

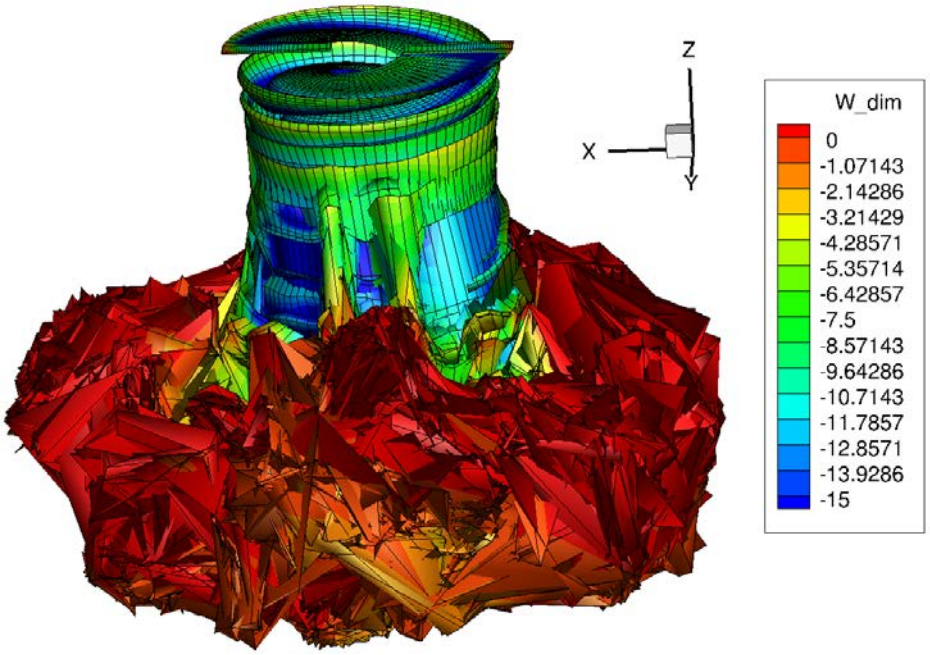

Figure 64: Caradonna Test 1: entire wake

paring with the entire shape of the Carpenter's wake for Caradonna the contraction of the wake is less visible. The smaller vortex core radius permits to highlight better the rollup at the tip vortex but these effects are still too weak.
Generally the wake seems to be stable and the red zone is smaller than the Carpenter one which is a strange phenomenon considering the smaller VCR. The first instability is visible after a few revolutions where the panels do not behave linearly but a reduction of the induced velocity of around 3 or 4 m/s messes up the shape in two points (green vertical lines in the blue zone).
Before presenting the case with the smaller VCR, the two cases with a linear twist will be introduced together since they both present a similar modification of the rotor model which does not come from reported data; it is still interesting to understand properly the phenomenon of the elastic twist.
Both simulations converge and, as expected, the case with one degree of linear twist achieves a result closer to the test data with a final C_T of 0.00465. This result is very interesting since it highlights the importance of having the most accurate test data possible; just one degree of linear twist produces a variation of 13% in the global re-

sult.

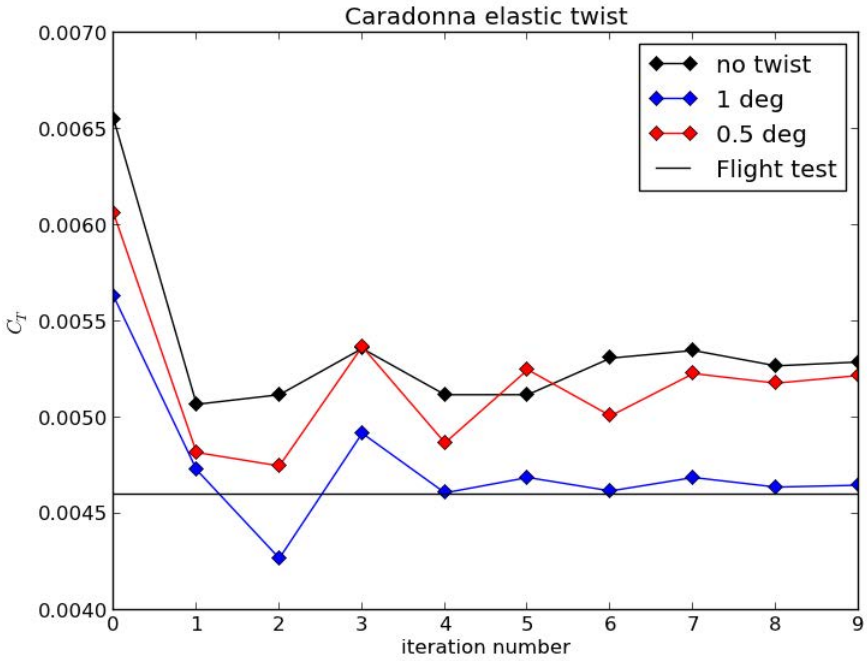

Figure 65: Caradonna elastic twist convergence

The difference between half degree of linear twist and the model without modification is negligible, this can be caused by all the interpolations that are required in the codes that reduce the global accuracy. The BEMT result is shown by the iteration number 0 and presents a variation of the thrust coefficient of around 10% every half degree of twist.

Fig.66 shows the comparison in the local distribution of the lift coefficient and the angle of attack for the two cases. According to these two results it is clear that the 0.5

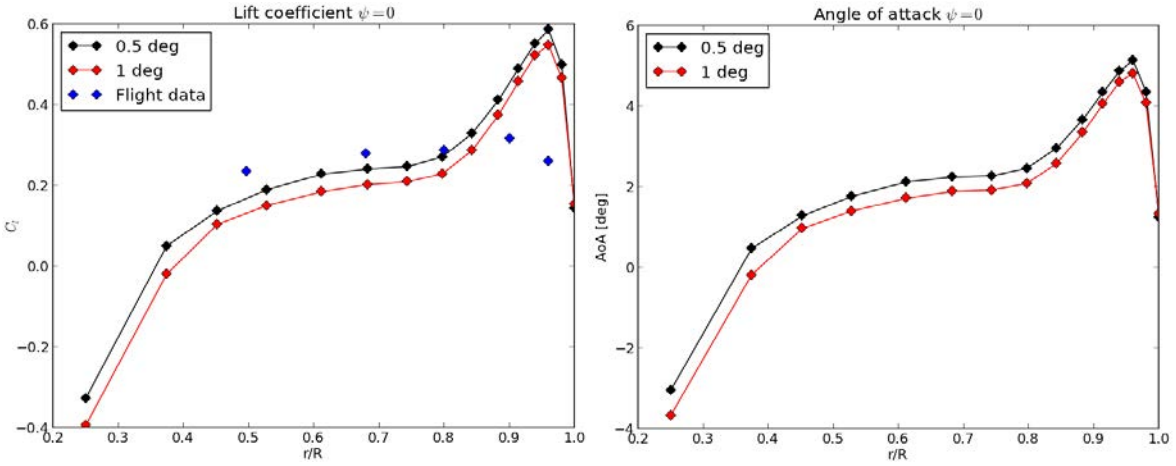

(a) Caradonna elastic twist: lift coefficient (b) Caradonna elastic twist: angle of attack

Figure 66: Caradonna elastic twist: AoA and lift coefficient comparison

degrees of linear twist fits better the test data; near the tip the peak is still to high and this produces the offset in the global result of the thrust coefficient.
This confirms the correct behaviour of the free wake method in the inner and middle part of the blade and proves once more the correct effect of the missing lines implementation.
The last case that will be presented is the normal rotor model with the smaller vortex core radius. The results presented show how this alteration destabilizes the code and the shape of the wake. The iteration sequence did not converge so the results presented correspond to the first iteration. Even with the higher relaxation factor the solution diverges from the momentum theory to a result close to the test data without decreasing the difference between one iteration and the other.
The thrust coefficient after the first iteration is 0.00486 which is 5% off the result. Even the local trend improves comparing to the large vortex core radius since the difference with the test points decreases especially in the inner part of the blade. The amplitude of the peak is also reduced and this explains the improvement in the global result.

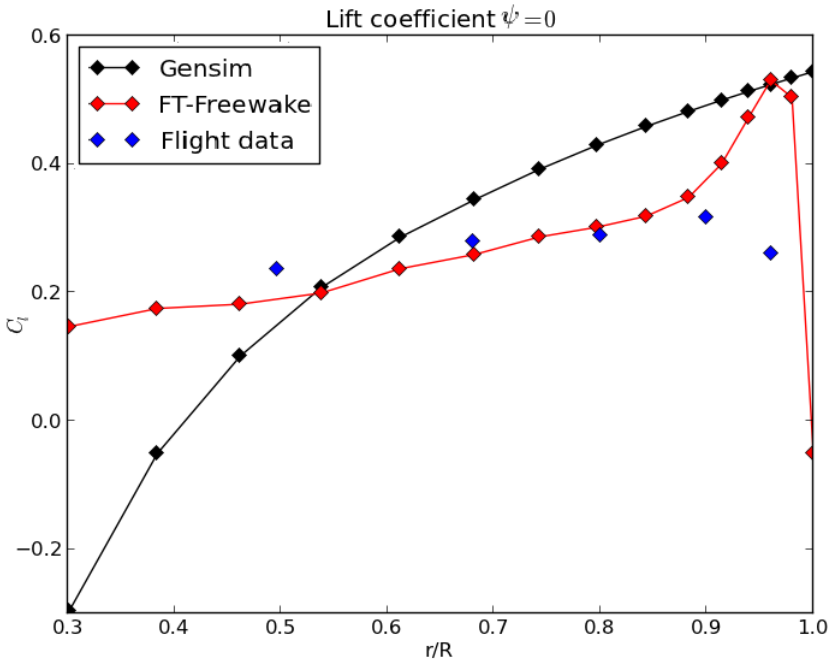

Figure 67: Caradonna small VCR: lift coefficient

Unfortunately the iteration did not converge and this is well explained by the shape of the wake and the position of the tip vortex which has the higher vorticity. The tip vortex is stable for the first 3 revolutions and afterwards it totally diverges without moving far from the rotor disk; due to the peaks that the induced velocity can reach the vortices are stretched and shortened.
Increasing the discretization points allows to obtain a more stable solution but that

does not really permit an improvement in the computational time comparing with CFD that still produces more accurate results.
Counting the stable revolutions it is clear that for a hover case the vortex core radius must be increased.
Except for the first revolution, in which the vorticity trend is reasonable, the shape of the wake does not permit to explain the strength of the vortices that seem to be constant in half revolution and decrease in the other which is clearly not reasonable. This aspect can also be just a plotting inaccuracy.

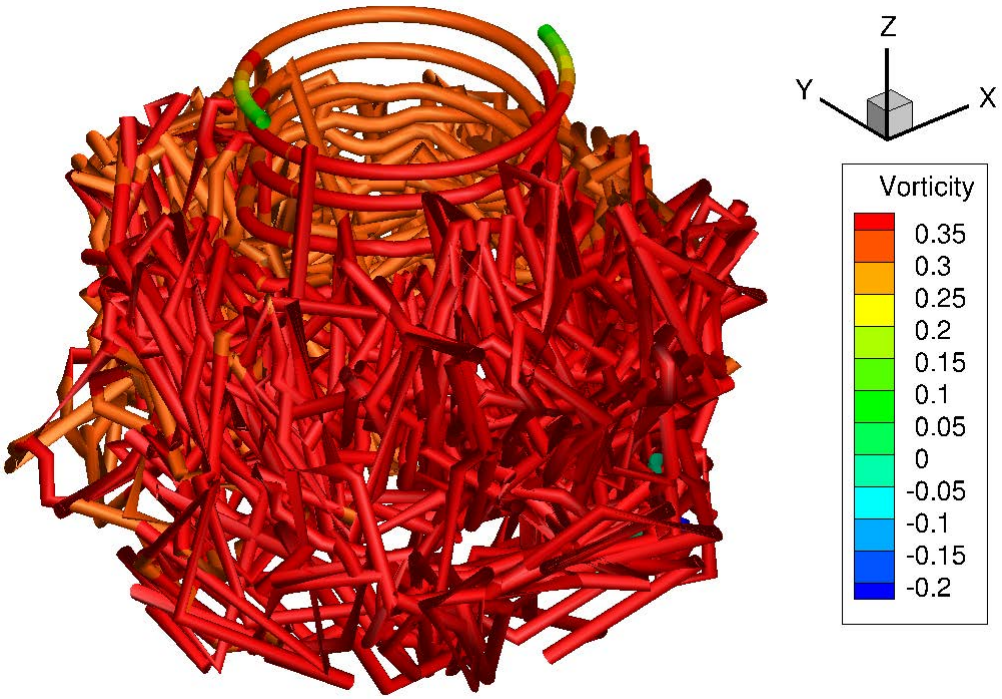

Figure 68: Caradonna small VCR: Tip vortex position and strength

As done for the Carpenter rotor, table 7 summarizes the results for all the test described. For the small VCR case the results regard the first iteration.

Table 7: Caradonna-Tung test magnitudes

Magnitude	Test 1	Small VCR	0.5 deg twist	1 deg twist
Thrust [N]	588.8	541.5	582.2	518.3
C_T	0.00529	0.00486	0.00523	0.00465
$\frac{C_T}{\sigma}$	0.04982	0.04583	0.04927	0.04386
Induced power [kW]	4.5	4.0	4.4	3.7
Average v_i [m/s]	7.672	7.358	7.629	7.198
FM	0.6338	0.6555	0.6505	0.6145
Computational time [s]	50580	86940	54000	50400

The computational time reflects the divergence problems and for the small VCR case

is increased by 40%. The other parameters do not present strange effects.
The results of the Caradonna case confirmed the difficultness of this rotor for both codes and showed some of their weaknesses, but it also showed a huge improvement of around 30% comparing with the BEMT.

6.3 Results for the H135 rotor

A large number of flight test were carried out for the AIRBUS H135 varying the input parameters for different flight conditions in order to find the more stable and accurate configuration. The main difference with the validation tests is that in this case Gensim trims on the thrust without prescribing the pitch angles.
The Caradonna case showed that the result depends on the dimension of the vortex core radius, so 16 different cases were tested with 3 different VCRs. The cases are divided in four groups, every group has a similar weight and 4 different flight speeds. This permits to find a general trend of the behaviour varying the velocity for different normalized weights (normalizing the weight permits to remove the dependence of the temperature, the altitude and the rotational velocity). The 3 VCRs have been expressed in terms of percentage of the maximum chord of the blade and are 30%, 50%, 80% of the chord. The other input parameters of the freewake have been chosen in order to permit the convergence and to reduce the inaccuracies. Since the lower forward flight speed is around 35 knots the wake length number used is 5 revolution which permits to consider effects near the rotor disk and reduces the computational time compared with a hover case. Table 8 summarizes all the input parameters employed in the freewake code and in the coupling script: The input parameters required by Gensim to compute the trim

Table 8: H135 input parameters

Magnitudes	Amplitude
Number of iterations	7
Relaxation factor	0.2
Moving point	0.3
Wake revolutions	5
Max turns	7
Radial discretization	40
Azimuthal discretization	72
VCR	30%,50%,80% of c

are the gross mass, V_x, V_z, temperature and the altitude. Table 9 highlights all these data for every test simulated arranging them by normalized weight and forward flight speed. The outputs will be compared with the flight data and a validated version of the H135 Gensim model, the inflow factors akh and akf have been adjusted to match

the flight test results. A negative V_z is a positive rate of climb due to the Gensim

Table 9: Flight test data for H135 in forward flight

T.no	W [kg]	V_x [kts]	V_z [ft/min]	T [C]	Zp [ft]	M.no [kg]
105-197	2650	46.2	-7.1	11	5030	3020
105-205	2630	73.7	1.7	11	4995	2988
105-184	2679	105.2	0.8	11	4987	3037
105-176	2696	133.3	-3.8	11	4988	3040
118-39	2934	46.2	23.0	38	1495	3350
118-43	2920	74.5	-13.6	38	1496	3335
118-36	2945	98.5	3.16	39	1490	3371
118-30	2963	133.3	-18.87	40	1490	3398
246-579	2994	34.3	46.2	23	5392	3481
246-583	2983	82.1	22.2	22	5303	3504
246-585	2977	104.2	-4.2	22	5346	3503
246-589	2964	138.4	-10.6	23	5260	3479
220-516	3004	38.7	18.6	13	10002	3937
220-518	2997	63.3	-18.5	13	10057	3938
220-521	2987	100.4	3.8	13	9993	4062
220-526	2968	117.6	0.3	13	9991	4040

axis orientation. Obviously the normalized weight is not the same for every test case depending on the flight conditions and the reduction of the fuel mass during the flights. The results for the power are presented without the numerical description along the y axis to protect AIRBUS Helicopters internal data. The relative error with the flight test data is also presented for every case.

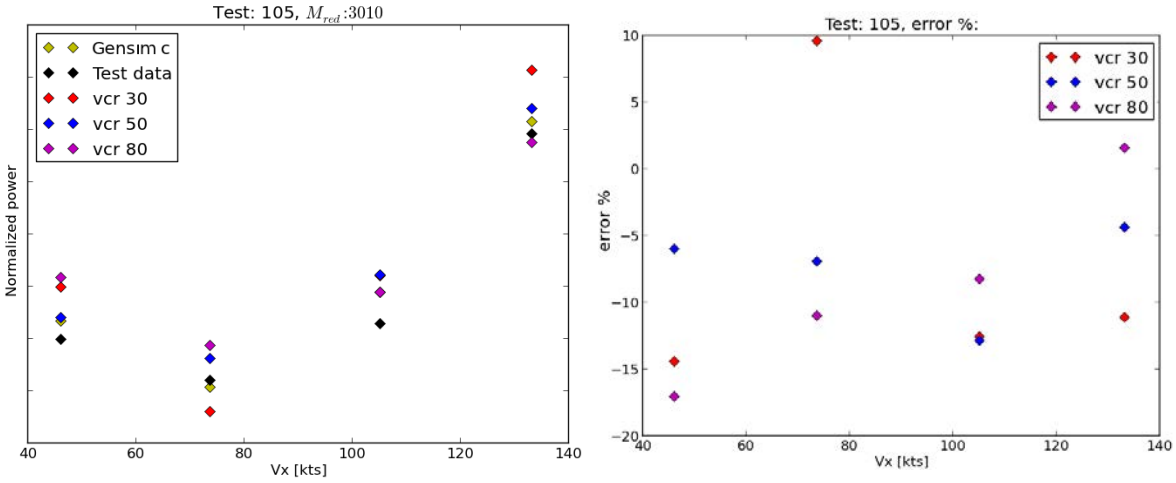

(a) Flight Test 105: P_{red} vs Vx

(b) Flight Test 105: % error

Figure 69: Flight Test 105

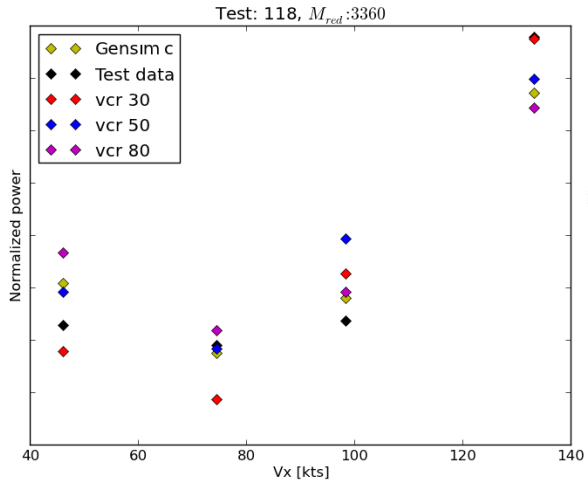

(a) Flight Test 118: P_{red} vs Vx

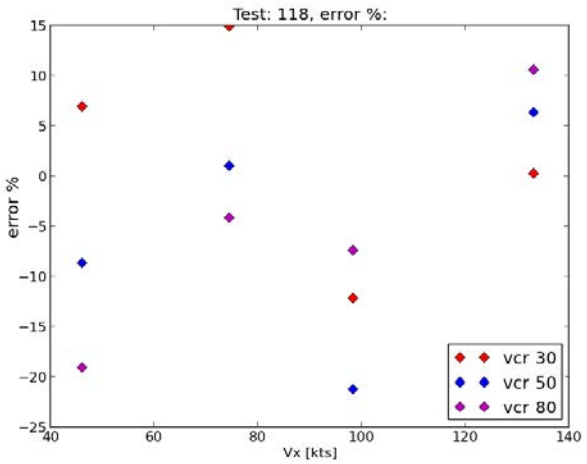

(b) Flight Test 118: % error

Figure 70: Flight Test 118

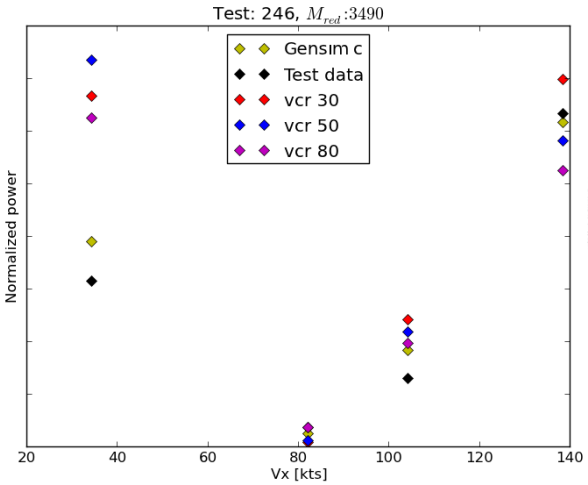

(a) Flight Test 246: P_{red} vs Vx

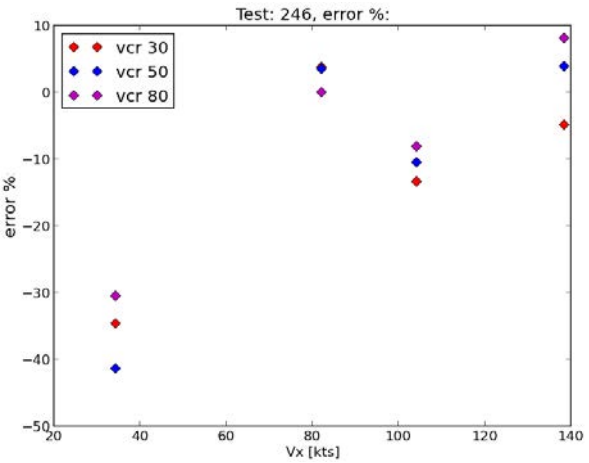

(b) Flight Test 246: % error

Figure 71: Flight Test 246

The graph show that not every VCR result is accurate but that it is possible to find a VCR configuration for every result, except for the highest weight, that outputs a required power with a maximum of 10 % of relative error respect to the flight test data.

Analyzing with more accuracy the results it is clear that the high normalized weight is difficult to evaluate with this code and the reason must be searched in its basic theory. A high weight helicopter requires high thrust to fly, not modifying the rotational speed a much higher angle of attack is required. If the polars for the angle of attack is not in the linear part or in the worst case is in a stall condition that means that a high angle of attack produces a low lift coefficient.

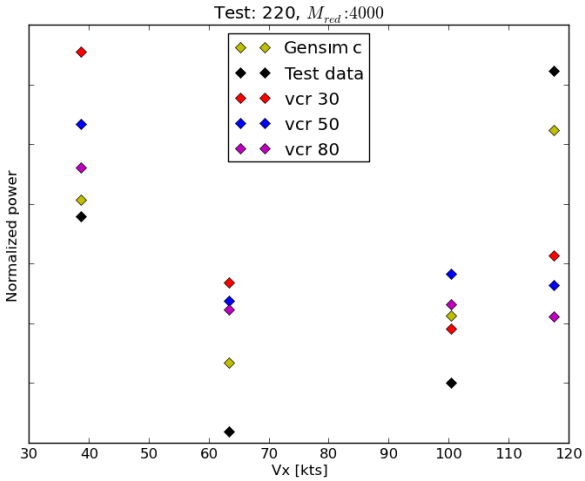

(a) Flight Test 246: P_{red} vs Vx

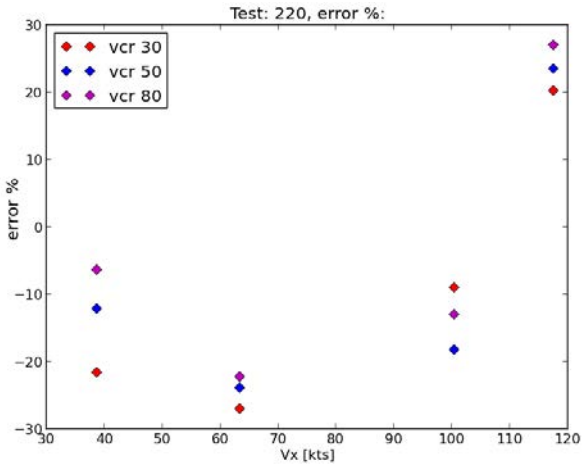

(b) Flight Test 246: % error

Figure 72: Flight Test 246

The other case for which it is difficult to find a vortex core radius that produces reasonable results is the test number 246 with lower speed: analyzing the table that summarizes the flight conditions, it is possible to notice that another parameter might affect the accuracy of the result. This case has the highest descending velocity of all the cases with more than 46 ft/min, this aspect, summed with a low velocity, can be considered as a difficult situation for the freewake code since the wake does not move far from the rotor plane quickly and the descending speed that must be subtract to the induced velocity to find the position of the wake at any instant could produce a significant number of BVI. To increase the accuracy of this case one option might be to increase the wake length and the number of revolutions analyzed.
For the other cases FT-Freewake produces one or more results inside 10% of accuracy. To understand how difficult is to predict the performance of a helicopter the previous graph showed the results compute by Gensim (yellow) that has an inflow model modified in order to match the flight test data and in many cases outputs a power that does not fit perfectly.
Interpolating the results presented with the Python function scipy.interpolate.interp1d that permits to choose the grade of the polynomium, it is possible to find the best vortex core radius along the helicopter speed for the normalized weight used. If the user has a normalized weight different from the analyzed ones it will be enough to linearly interpolate between the charts in Fig.73 for the required speed. The trend for the Test number 220 has been compute according to the best results but obviously is not reliable. The other three plots show that the magnitude varies with the weight but the trend is coarsely confirmed: at low speed a higher VCR is required, it then decreases until 50-70 knots to raise up again until 100 knots. After 100 knots it decreases

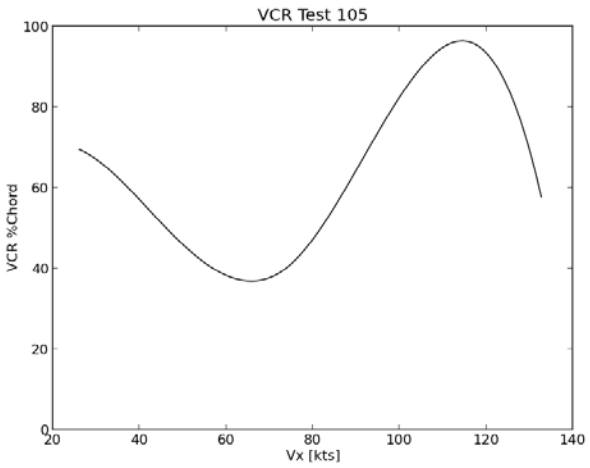

(a) Flight Test 105: VCR vs speed

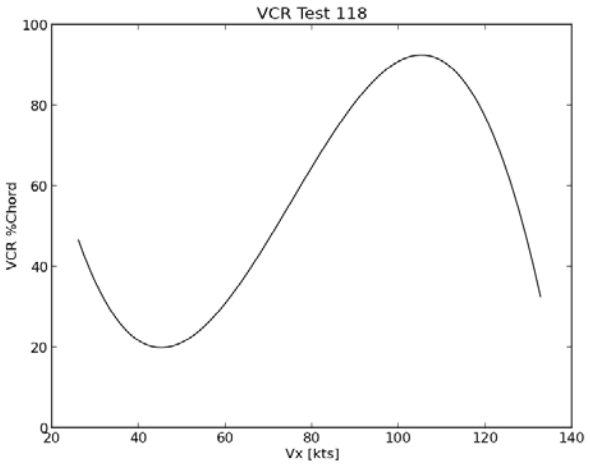

(b) Flight Test 118: VCR vs speed

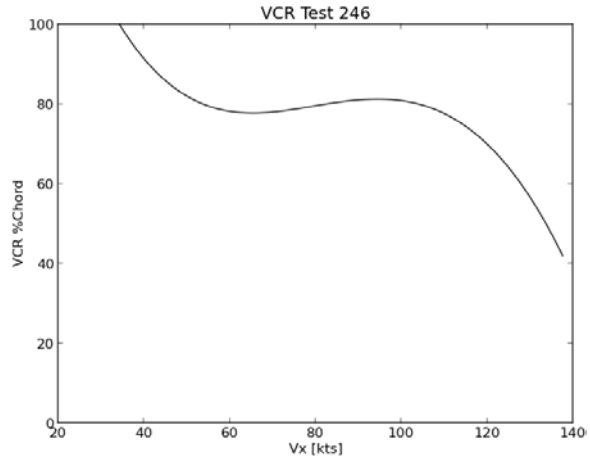

(c) Flight Test 246: VCR vs speed

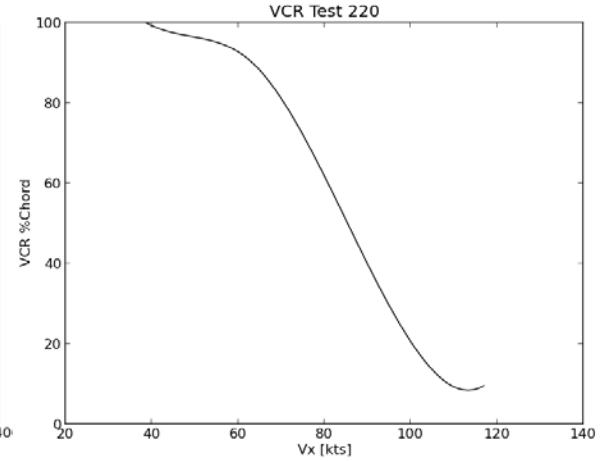

(d) Flight Test 220: VCR vs speed

Figure 73: VCR vs speed

strongly and reaches its minimum at the maximum speed of the helicopter.

The range goes from 0 to 100% of the chord, it is possible to use even higher vortex core radius but it will produce a smooth wake shape that does not represent the reality. Increasing the number of discretization points allows to reduce the vortex core radius down to 5 or 10% of the chord but with more than 60 points on the radius the computational time will explode.

In order to not overload this paper just two of the 48 cases globally presented will be analyzed more in detail: the test number 118-43 with a VCR of 50% of the chord and the test case 220-526 with a VCR of 30% of c. The first simulation achieved very accurate global results, while the second one on the contrary highlights the weaknesses of the vortex theory.

As done for the validation tests, the convergence of the iterations will be firstly presented. From Fig.74 it is possible to understand that the convergence is achieved after

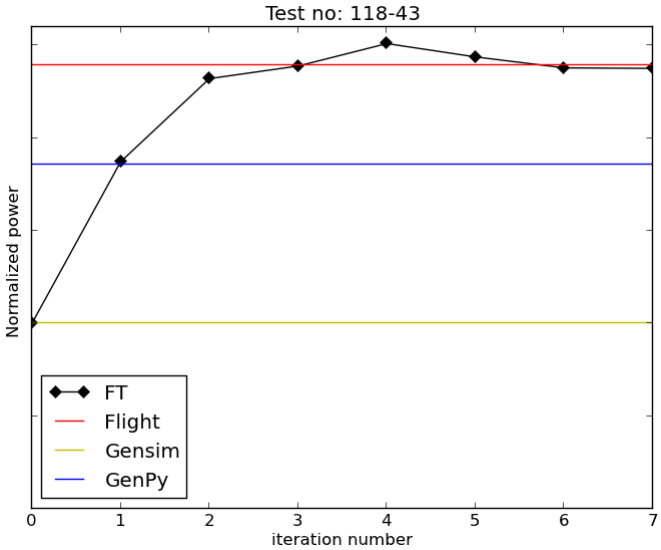

Figure 74: Test 118-43: Convergence

2 iteration (excluding the number 0) and that the difference with the flight data is totally neglectable. The improvement respect to the BEMT is around 21% and about 8% towards corrected Gensim.

Fig.75 aims to compare the lift coefficient at the rotor disk between stand alone Gensim and the last iteration: From the graph on the right side the presence of vortices in the

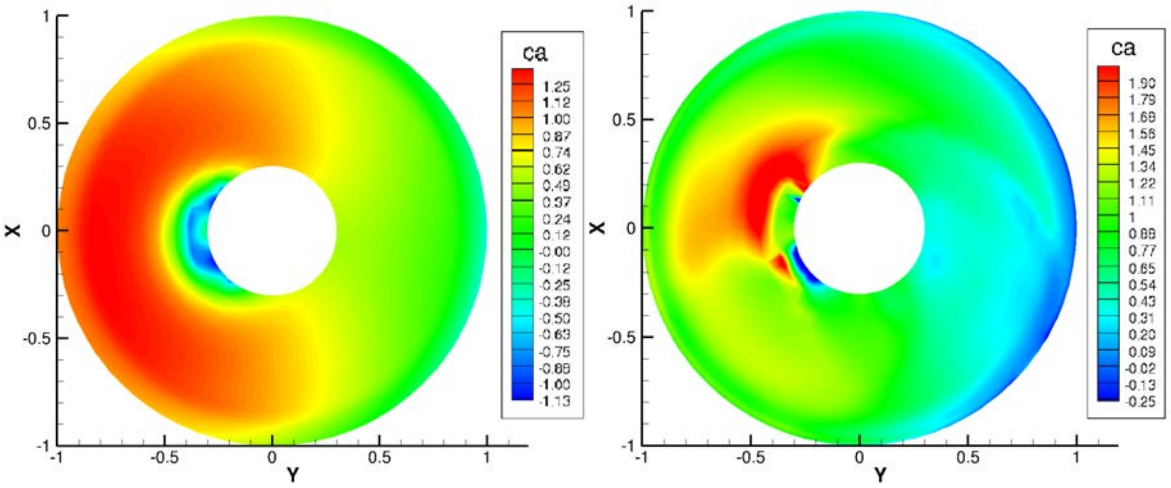

(a) Test 118-43: c_l iteration 0

(b) Test 118-43: c_l iteration 7

Figure 75: Test 118-43: lift coefficient comparison

rotor plane is clear; in the advancing side it is possible to see the strong interaction with the tip vortex of the previous blade and the weaker one due of two preceeding blades. Also on the retreating side the lift coefficient has not a uniform distribution as in the BEMT but after an azimuth of 270 degrees it strongly reduces its magnitude. The effect of the reverse flow is not very strong due to the low velocity of the helicopter

but is well visible on both cases in the retreating side near the root. Even if the trend is different, it is important to remember that since Gensim trims, the total thrust is the same. Especially from the chart in the left it is clear that the rotor has been designed in order to achieve a uniform lift distribution on the disk. Clearly due to the interaction with the wake and its vortices this is only theoretically possible.
Fig.76 shows the instant induced velocity at the rotor disk and the BVI, this helps the reader to understand also the lift coefficient distribution.

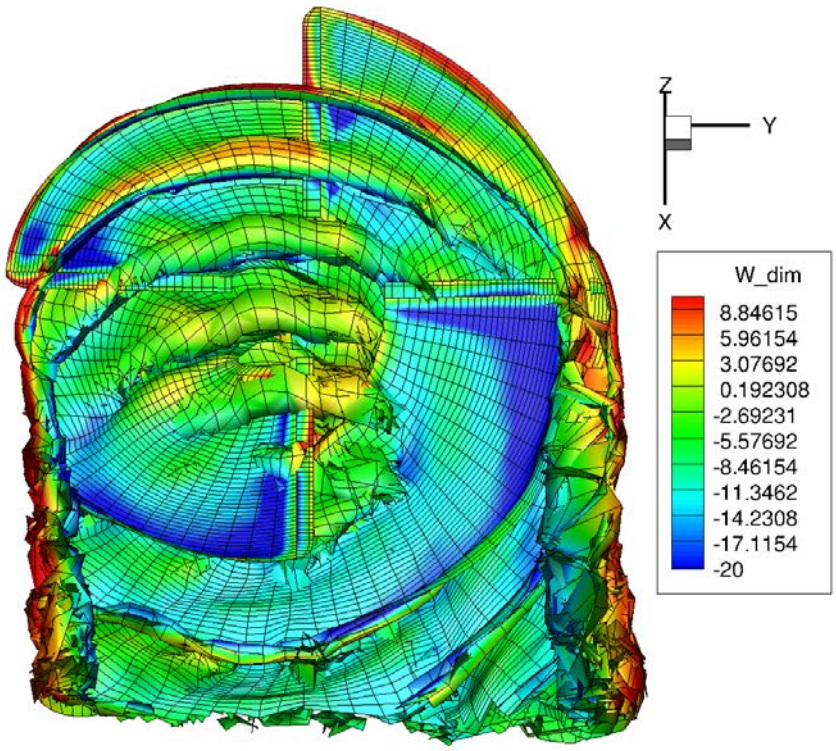

Figure 76: Test 118-43: BVI

The reduction on the induced velocity due to the blade vortex interaction is perfectly visible: the blade at an azimuth of 180 degrees is crossed by 3 tip vortices coming from the previous blades and all of them are normal to it. Different is the situation of the blade in the retreating side in which the angle is very low and the vortex is almost tangential.
Another phenomenon clearly visible occurs at an azimuth of 90 degrees in which a strong vortex leaves the blade from the tip in the flight direction. The same phenomenon happens also in the retreating side but it is weaker due to the lower velocity. The low VCR in this simulation permits to visualize the tip vortex that it is caused by the finite length of the blade.
This plot also permits to understand the difficulties of simulating a rotating wing instead of a fixed one: if the blade is not affected by other vortices it is clear that in

the downstream direction a strong downwash velocity will occur and this effect always happens for a fixed blade, but due to the rotation and the presence of other blades for a rotating wing the inflow field is far from being uniform.
Before presenting the entire wake of a helicopter in forward flight, it must be checked whether the implementation of the missing vortex lines produces different effects depending on the azimuth. Fig.77 shows the magnitude of the total induced velocity every 90 degrees of azimuth. The implementation works properly since the magnitude

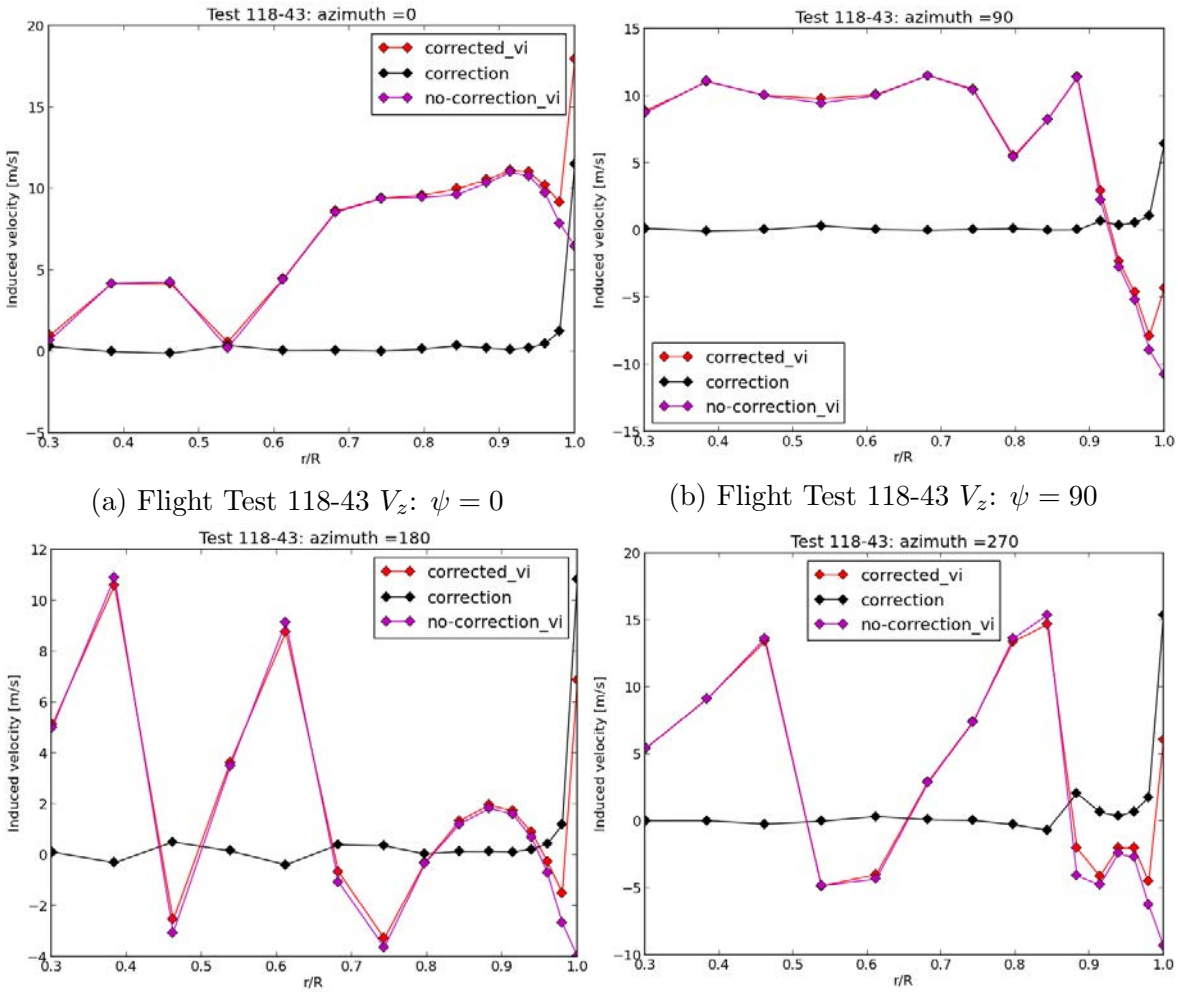

(a) Flight Test 118-43 V_z: $\psi = 0$

(b) Flight Test 118-43 V_z: $\psi = 90$

(c) Flight Test 118-43 V_z: $\psi = 180$

(d) Flight Test 118-43 V_z: $\psi = 270$

Figure 77: Flight Test 118-43: induced velocity

of the induced velocity varies with the azimuth with a peak on the retreating side of more than 15 m/s.
These plots are very helpful to find the precise position of the BVI; this effect is clearly visible for an azimuth of 180 degrees and it shows that, starting from the rotation axis the first interaction with a vortex according with Fig.76 occurs before the root, the second one at around 45% of the radius and the last one at 75%.

To conclude the discussion for this flight test the entire wake is shown if Fig.78.

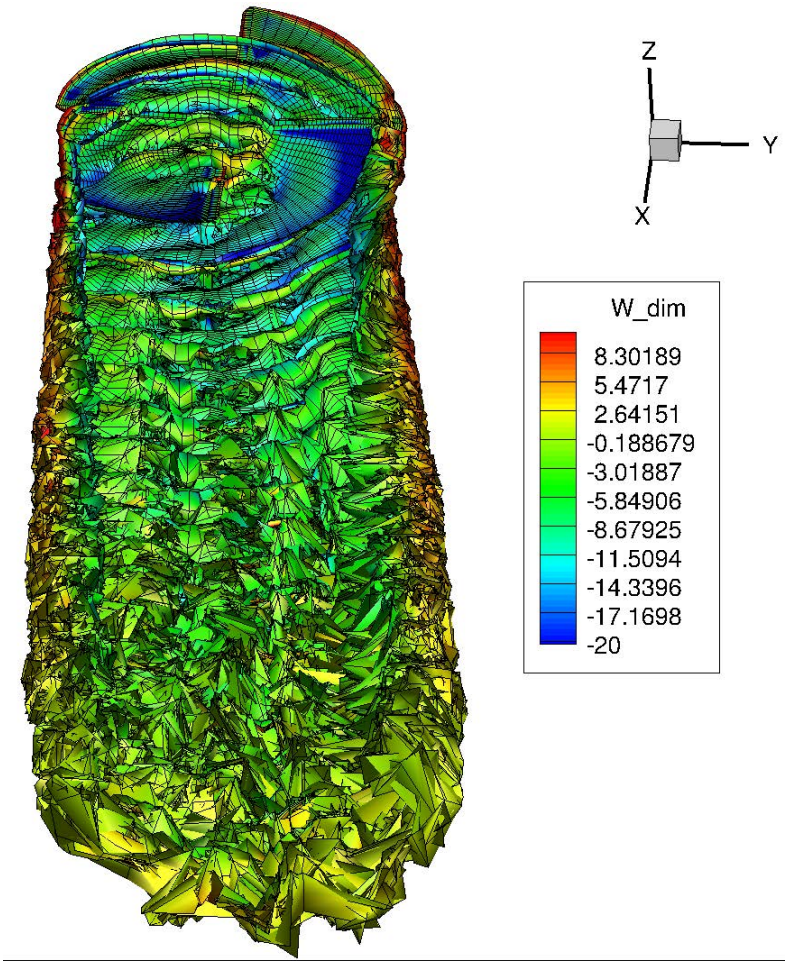

Figure 78: Test 118-43: entire wake

Far from the rotor it is not possible to distinguish anymore one vortex from the other due to the destabilization of the wake (in the visualization from the bottom this effect is still visible); even if the free stream velocity is small, the wake goes far quickly enough to not contaminate the rotor plane with its instabilities. Due to the helicopter velocity the wake spreads mainly along the x direction and just for the induced velocity component along the z axis.

The last forward flight case analyzed is, as previously announced, the test case number 220-526 due to its significant stall effects. The case analyzed varying the vortex core radius did not converge for any VCR as expected. To achieve reasonable results for this case the only possible choice is to decrease as much as possible the vortex core radius in order to increase the induced velocity enough to reduce the local stall areas. Increasing the number of radial points up to 51, reducing the wake length to obtain a sustainable computational time (this does not affect the final result since the velocity is really high) and increasing the relaxation factor to 0.3 permitted a stable convergence.

The VCR used for this simulation is 5% of the chord. Fig.79 shows the convergence and it compares the result with corrected Gensim and the flight test data.

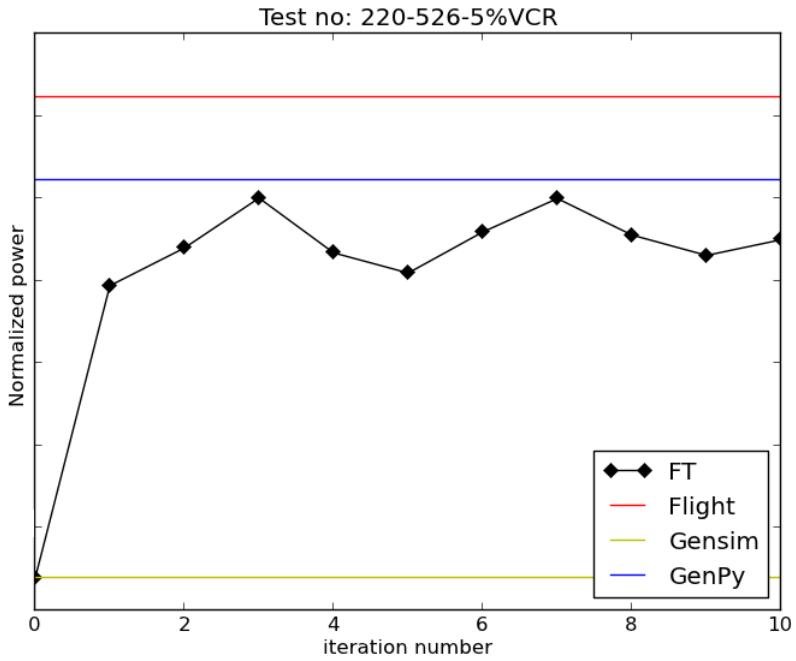

Figure 79: Test 220-526: Convergence

The result is characterized by a percentual error of 11% with respect to the flight test data. The main highlight is the improvement with respect to the BEMT, around 30%, also the difference with corrected Gensim is acceptable. This proves that setting a more computationally expensive configuration permits to increase the accuracy of the results for the difficult cases. Fig.80 show the AoA and the lift coefficient distribution in the rotor, highlighting the distortion due to vortices and the fact that on the retreating side there is a large area that stalls.
Comparing with the previous tests, it is clear that since the forward flight speed is higher there are less interactions with the vortices coming from the previous blades.
Even if the free stream velocity is really high, it is not possible to find a reverse flow area and this can cause the inaccuracy in the global result.
To conclude, the entire wake is presented in order to let the reader understand how the vortex core radius affects the tip vortex and its shape.
The tip vortex increases its behaviour with the decrease of the vortex core radius. The levels of the induced velocity in the axis have been manually limited since in some point of the far wake the induced velocity raised up to 100 m/s and do not permit a clear visualization. This simulation also confirmed that the trend of the vortex core radius is correct, since it strongly decreases at high speed. Using a small vortex core radius with less discretization points will produce the complete divergence of the simulation.

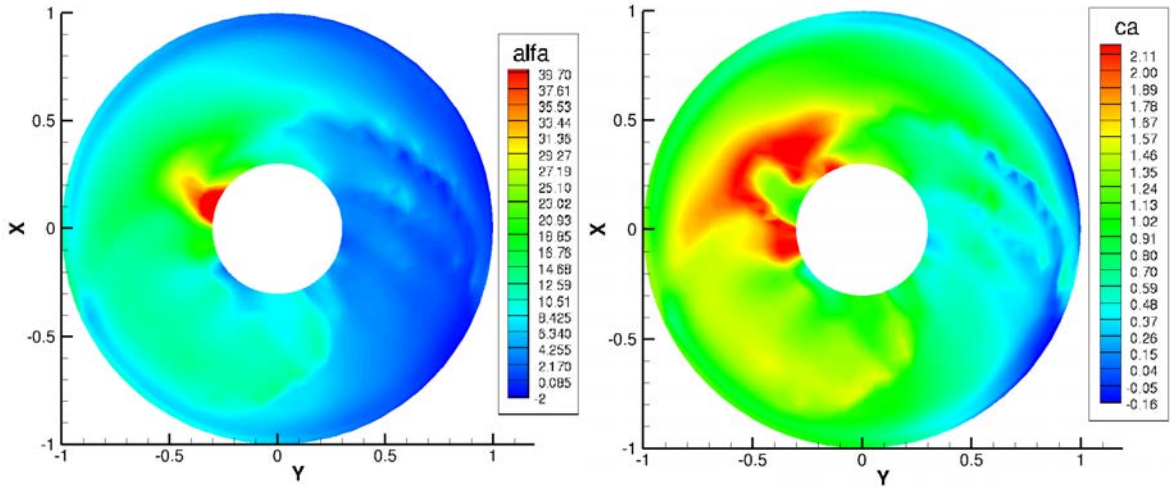

(a) Test 220-526: α iteration 10

(b) Test 220-526: c_l iteration 10

Figure 80: Test 220-526: lift coefficient and angle of attack

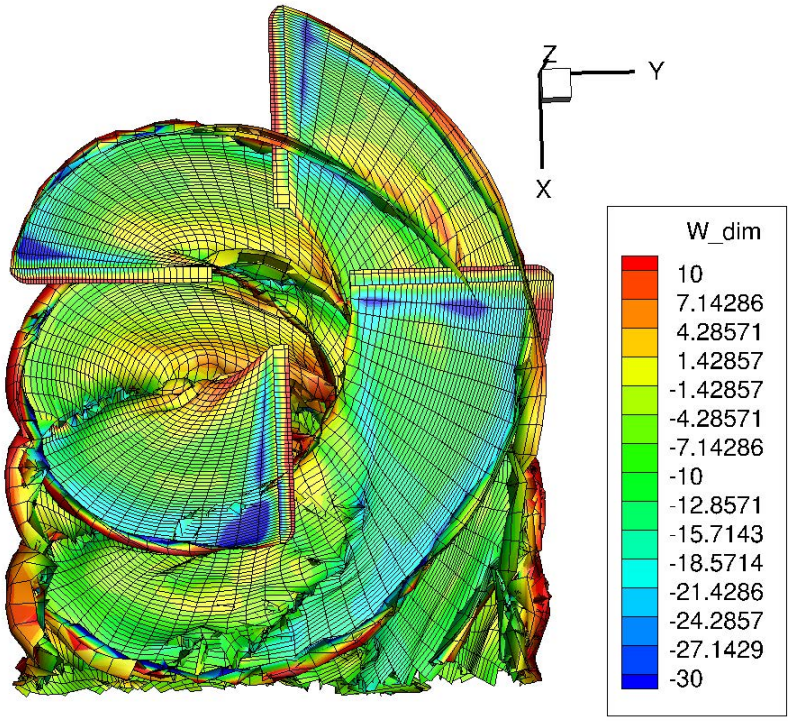

Figure 81: Test 220-526: Entire wake

All the forward flight cases run allowed to understand the behaviour of the code and find the easier configuration that permits to achieve reasonable results; except for some "extreme" flight tests that need a more complex setting.

The last case that will be presented is the H135 in hover and table 10 summarizes all the input parameteres including the flight test data.

The relaxation factor has been increased compared with the other cases to improve the

Table 10: H135 hover

Magnitude	Hover
Weight [kg]	2921.1
V_x [kts]	0
RoC [ft/min]	-2.0
Temperature [C]	2
Altitude [ft]	974
Wake length rev	16
Max turns	18
VCR	80% chord
iterations	7
radial discretization	40
RF	0.3
Moving point	0.3

convergence, since this case, a hover case with four blades is very difficult to analyze with a free wake method. The rotor has been designed in order to obtain a uniform lift along the radius, this permits to stabilize the simulation by increasing the vortex core radius to 80% of the chord since the difference with the BEMT should not be high. The convergence along the iterations, the comparison with the flight data and with corrected Gensim will be presented in Fig.82.

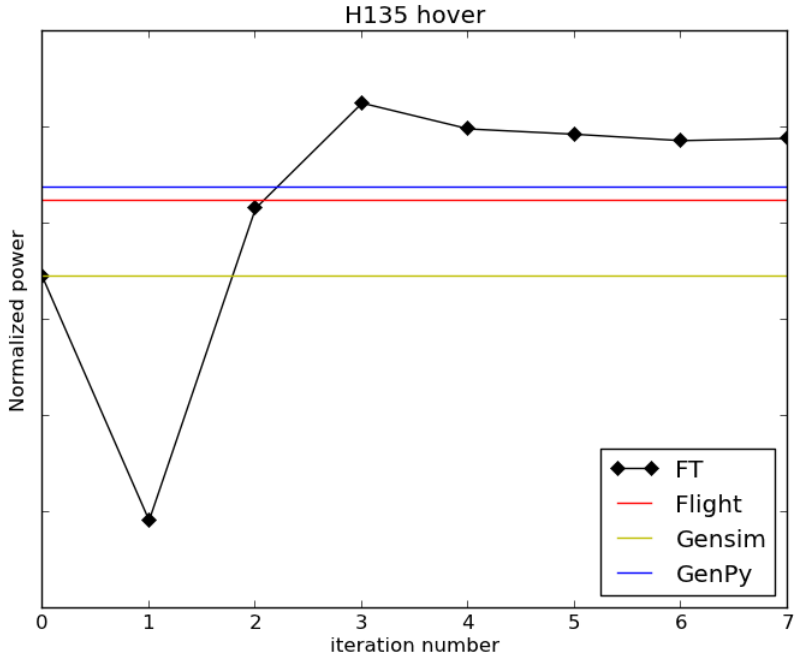

Figure 82: H135 hover: convergence

The convergence is reached after three iterations, the global result is higher than the flight test data of around 5%. The explanation has to be searched in a higher induced

velocity in the inner part of the blade caused by a too low induced velocity in the outer part due to the interaction with the second rotation of the wake. Also the classic momentum theory produces a result with an error of around 8%; this is explainable analyzing the rotor lift distribution and Fig.33 that shows the factor that must be multiplied to the average induce velocity to obtain the corrected Gensim result.
The global plot of the induced velocity at the rotor disk is shown in Fig.84:

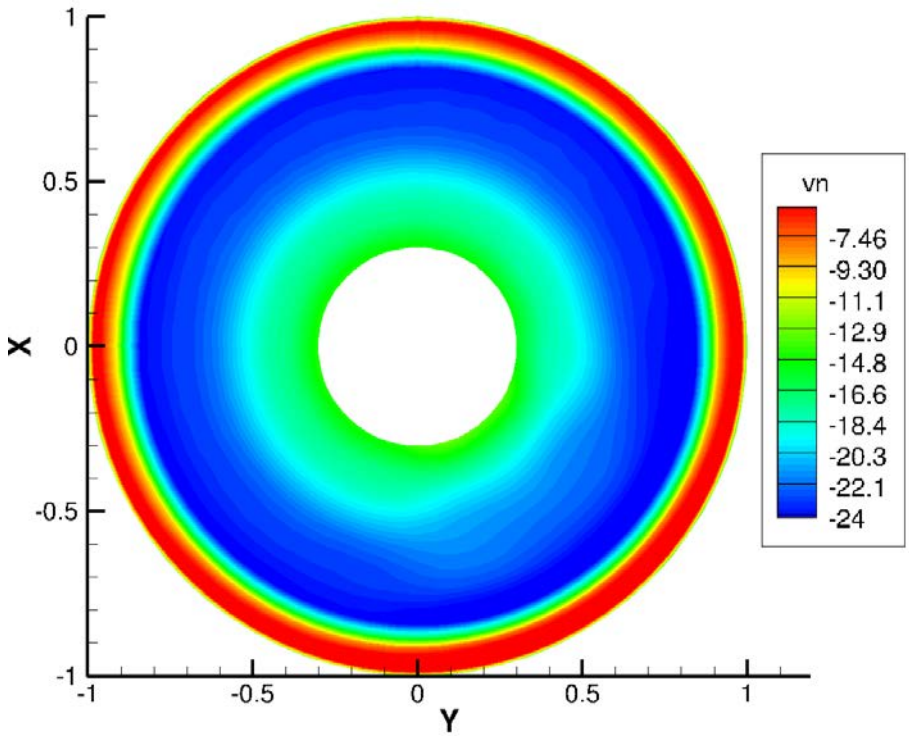

Figure 83: H135 hover: induced velocity at the rotor disk

The plot highlights the effect explained previously and it also shows the non perfect uniformity along the azimuth. In this case two main reasons must be analyzed: the first one is caused by the instability of the code in the far wake, that diverging can modify the inflow; the second one and more important is the fact that the plots do not show the induced velocity field of an isolated main rotor, the other components of the helicopter affect the center of mass, the momentums and so the lift distribution.
To conclude the chapter the entire shape of the wake will be presented.
The entire wake is very stable for around 4 revolutions and then it quickly diverges. Analyzing the trend of the diverged part it is clear that in the left side of the graph the wake remains higher and closer to the rotor disk respect to the wake on the right side. The missing vortex lines are visible in this plots because of the upwash at the tip and the BVI that occurs between the blades and the tip vortex from the previous wing.
The computational time for this simulation is around 30000 seconds per iteration,

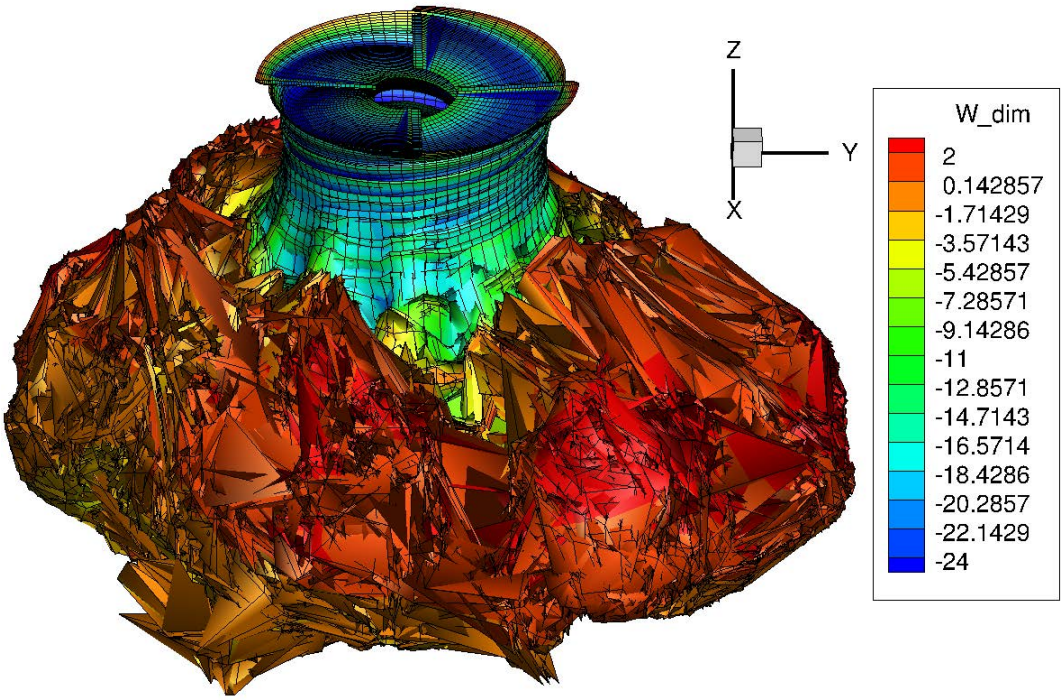

Figure 84: H135 hover: wake

which means more than 210000 seconds using 10 CPU's. A CFD simulation of the entire helicopter wake with around 300 CPU's requires from two to three weeks to converge.

7 Conclusions

The aim of this master thesis was to compute the induced velocity field of the main rotor in many different situations thanks to a free-wake method and evaluate the performance of the entire helicopter by means of Gensim, an AIRBUS Helicopters internal code that adopts the blade element theory.
Two main rotors from literature (Carpenter and Caradonna-Tung) were simulated to validate the code analyzing the induced velocity field, the angle of attack, the lift coefficient distribution and the entire shape of the wake. The first results showed the absence of a non negligible portion of the trailing vortices causing a strong reduction of the induced velocity in the outer region of the blade. To solve the problem these missing vortex lines have been implemented manually in the coupling between the two codes. This correction helped to compute the tip losses that were totally neglected by the previous implementation but does not permit to modify the entire shape of the wake and its behaviour on the induced velocity at the rotor disk. This correction must be considered as a preliminary correction and the problem must be solved inside the free-wake code.
The results for the Carpenter rotor permitted to understand the general behaviour of the code in hover situations and probably due to its simplicity the accuracy compared with a bench test data was satisfactory.
The second validation case was selected since straight untwisted blades are difficult to simulate with classical BEMT under the uniform inflow assumption. The results for this case showed a significant improvement compared with Gensim stand alone but the final result confirmed an offset of around 13%.
Finally the entire H135 was simulated in 16 different forward flight conditions comparing the result for different vortex core radii with flight test data in order to find common settings for both the codes. The trend of the vortex core radius against the speed of the helicopter was plotted for different normalized weights in order to permit an easier simulation setup in the future. The results that have been presented show that for almost every flight test it is possible to achieve results within 10% of accuracy. As previously explained the code struggles in two main situations: hover cases or similar situations (low speed and descend) in which the wake does not move away from the rotor disk quickly and high weight and high speed in which stall effects might occur.
The present work presents just the starting point of the coupling between Gensim and FT-Freewake and showed the advantage in the computational time compared with CFD analysis. To improve the accuracy of the results and stabilize the simulations some implementations are required:

- Implement the missing vortex lines in FT-Freewake;
- Implement a vortex core growth model that increases the vortex core radius with the ageing of the wake in order to stabilize the wake shape in the far field;
- Increase the radial discretization points in Gensim in order to decrease the inaccuracy due to interpolation;
- Import the fuselage geometry in the freewake in order to improve the download prediction and improve the wake shape;
- Implement the possibility to evaluate the ground effect directly in FT-Freewake.

The state of art in the CPU's technology does not permit to use at the moment CFD analysis to simulate the entire helicopter in all the possible configurations because of the too large computational time required. Since a freewake code permits to achieve medium-high accuracy results around 20 times faster than CFD, the usage of these types of codes should increase drastically in this sector and should lead to more accurate steady state analysis and eventually to unsteady simulations.

References

[1] Wayne Johnson. *Helicopter theory.* 1980

[2] J. Gordon Leishman. *Principles of Helicopters Aerodynamics* University of Maryland 2000

[3] Raymond W. Prouty. *Helicopter Performance, Stability, and Control.* 1986

[4] A. R. S. Bramwell, George Done, David Balmford. *Bramwell's Helicopter Dynamics.* 2001

[5] Robert T. N. Chen *A survey of Nonuniform Inflow Models for Rotorcraft Flight Dynamics and Control Application.* NASA November 1969.

[6] Filipe Szolnoki Cuhna. *Vortex theory.* Istituto Superior Tecnico 2010.

[7] Patricia X. Coronado Domenge, Marcel Ilie. *Numerical study of helicopter blade-vortex mechanism of interaction using the potential flow theory.* Applied Mathematical Modelling 2012.

[8] Paul J. Carpenter. *Lift and Profile-Drag Characteristics of a NACA 0012 Airfoil Section as Derived from Measured Helicopter-Rotor Hovering Performance.* NACA 1958.

[9] F. X. Caradonna, C. Tung. *Experimental and Analytical Studies of a Model Helicopter Rotor in Hover.* NASA September 1981.

[10] AIRBUS Helicopters. *H135 Flight Manual.*

[11] Berend G. van der Wall, Michael Roth. *Free-Wake Analysis on Massively Parallel Computers and Validation with HART Test Data.* DLR Institute for Flight mechanics.

[12] Larry A. Young. *Vortex Core Size in the Rotor Near Wake.* NASA June 2003.

[13] K. R. Reddy. *The Vortex Flow field Generated by a Hovering Helicopter.* August 1980.

[14] Markus Dietz, Christoph Maucher, Dieter Schimke. *Addressing today's aeromechanic questions by industrial answers.* Eurocopter Deutschland GmbH 2010.

[15] Roth German. *Dynamischen Durchflussmodell nach Pitt/Peters fur die Bewegungssimulation von Hubschraubern im Zeitbereich.* Eurocopter Dezember 1993.

[16] Wayne Johnson. *A History of Rotorcraft Comprehesive Analyses.* NASA

[17] Andrea Garavello, Sebastian Fuhr, Raymond Laporte. *On the Establishment of Class 2 Helipad Takeoff and Landing Performance for the BK117 C-2: a Comprehensive Approach Based on Limited Testing and Simulation.* AIRBUS Helicopters.

[18] German Roth, Florian Vogel. *Flightmechanics and Performance Calculation Method: Upgrade Report for BK117-D2.* AIRBUS Helicopters.

[19] Wayne Johnson, *CAMRAD II, Comprehensive Analytical Model of Rotorcraft Aerodynamics and Dynamics.* Johnson Aeronautics, 1992.